Tensor Network Simulation and Optimal Control of Strongly Interacting Nitrogen-Vacancy Spins

Dissertation
der Mathematisch-Naturwissenschaftlichen Fakultät
der Eberhard Karls Universität Tübingen
zur Erlangung des Grades eines
Doktors der Naturwissenschaften
(Dr. rer. nat.)

vorgelegt von
Jirawat Saiphet
aus Nakhon Ratchasima/Thailand

Tübingen
2025

Gedruckt mit Genehmigung der Mathematisch-Naturwissenschaftlichen Fakultät der Eberhard Karls Universität Tübingen.

Tag der mündlichen Qualifikation:	20.08.2025
Dekan:	Prof. Dr. Thilo Stehle
1. Berichterstatter:	Prof. Dr. Daniel Braun
2. Berichterstatter:	Prof. Dr. Igor Lesanovsky

Abstract

English Nitrogen-Vacancy (NV) centers in diamond represent a promising platform for developing highly sensitive quantum sensors for magnetic fields and other physical quantities. The pursuit of sensors combining high sensitivity with high spatial resolution motivates the use of dense NV center ensembles, which inherently exhibit strong, long-range dipole-dipole interactions. Consequently, accurate simulation of these strongly interacting NVs becomes crucial. However, the exponential scaling of the Hilbert space dimension with the number of spins renders the exact simulation of their dynamics intractable for large system. Modeling the system's interaction with its environment as an open quantum system further increases the computational complexity.

This thesis addresses these challenges using tensor network methods. Specifically, the Matrix Product Density Operator (MPDO) formalism is employed to represent the many-body mixed state and simulate the dissipative dynamics of NV ensembles under strong dipole-dipole interactions. We benchmark the efficiency, numerical accuracy, and stability of different tensor network time-evolution algorithms that are capable of long-range interactions against exact numerical diagonalization, identifying a numerical instability in one algorithm when applied to MPDOs. Subsequently, we simulate the dynamics within the strong interaction regime and investigate the impact of decoherence on the accuracy of the MPDO simulations for given maximum bond dimensions.

Furthermore, we calculate the dynamics of the Quantum Fisher Information (QFI) to quantify entanglement generated by the strong interactions. This entanglement, quantified by the QFI, underlies the potential for quantum-enhanced sensitivity. Results indicate that magnetic field sensitivity can be enhanced by these strong interactions when the ensemble is driven by constant amplitude pulses. We also investigate the detrimental effects of excessively strong interactions on sensitivity.

Finally, we address the optimal control task of preparing states to maximize sensor sensitivity. The dCRAB optimization technique is implemented to find control pulses capable of achieving higher sensitivity than that attainable with constant driving fields. Successful optimized pulses for driving an ensemble of three NV centers into the target GHZ state are obtained via numerical simulation. The challenge of performing such optimizations using experimentally relevant parameters is also discussed.

German Stickstoff-Fehlstellen-Zentren (NV-Zentren) in Diamant stellen eine vielversprechende Plattform für die Entwicklung hochempfindlicher Quantensensoren für Magnetfelder und andere physikalische Größen dar. Das Streben nach Sensoren, die hohe Empfindlichkeit mit hoher räumlicher Auflösung kombinieren, motiviert die Verwendung von dichten NV-Zentren-Ensembles, die von Natur aus starke, weitreichende Dipol-Dipol-Wechselwirkungen aufweisen.

Folglich ist eine genaue Simulation dieser stark wechselwirkenden NV-Zentren von entscheidender Bedeutung. Die exponentielle Skalierung der Dimension des Hilbert-Raums mit der Anzahl der Spins macht jedoch die exakte Simulation ihrer Dynamik für große Systeme unpraktikabel. Die Modellierung der Wechselwirkung des Systems mit seiner Umgebung als offenes Quantensystem erhöht die Komplexität der Berechnungen noch weiter.

In dieser Arbeit werden diese Herausforderungen mit Hilfe von Tensornetzwerkmethoden angegangen. Insbesondere wird der Matrix Product Density Operator (MPDO) Formalismus verwendet, um den Vielkörper-Mischzustand darzustellen und die dissipative Dynamik von NV-Ensembles unter starken Dipol-Dipol-Wechselwirkungen zu simulieren. Wir vergleichen die Effizienz, die numerische Genauigkeit und die Stabilität verschiedener Algorithmen zur Zeitentwicklung von Tensornetzwerken, die in der Lage sind, weitreichende Wechselwirkungen mit exakter numerischer Diagonalisierung zu simulieren, wobei wir eine numerische Instabilität in einem Algorithmus identifizieren, wenn dieser auf MPDOs angewendet wird. Anschließend simulieren wir die Dynamik innerhalb des Regimes der starken Wechselwirkung und untersuchen den Einfluss der Dekohärenz auf die Genauigkeit der MPDO-Simulationen für gegebene maximale Bindungsdimensionen.

Darüber hinaus berechnen wir die Dynamik der Quanten-Fischer-Information (QFI), um die durch die starken Wechselwirkungen erzeugte Verschränkung zu quantifizieren. Diese Verschränkung, die durch die QFI quantifiziert wird, liegt dem Potenzial für eine quantenverstärkte Empfindlichkeit zugrunde. Die Ergebnisse zeigen, dass die Magnetfeldempfindlichkeit durch diese starken Wechselwirkungen erhöht werden kann, wenn das Ensemble durch Pulse mit konstanter Amplitude angetrieben wird. Wir untersuchen auch die nachteiligen Auswirkungen von zu starken Wechselwirkungen auf die Empfindlichkeit.

Schließlich befassen wir uns mit der Aufgabe der optimalen Steuerung, die

Zustände so vorzubereiten, dass die Sensorempfindlichkeit maximiert wird. Die dCRAB-Optimierungstechnik wird eingesetzt, um Steuerpulse zu finden, die eine höhere Empfindlichkeit als die mit konstanten Antriebsfeldern erreichbare Empfindlichkeit ermöglichen. Mittels numerischer Simulation werden erfolgreich optimierte Pulse für die Steuerung eines Ensembles von drei NV-Zentren in den Zielzustand GHZ ermittelt. Die Herausforderung, solche Optimierungen mit experimentell relevanten Parametern durchzuführen, wird ebenfalls diskutiert.

List of publications and personal contribution

List of publications

1. J. Saiphet, and D. Braun, *Simulation of the Dissipative Dynamics of Strongly Interacting NV Centers with Tensor Networks* , Phys. Rev. A **111**, 022604.

Personal contributions

Author	Author position	Scientific ideas (%)	Data generation (%)	Analysis & interpretation (%)	Paper writing (%)
Jirawat Saiphet	1	50	100	70	80
Daniel Braun	2	50	0	30	20
Title of paper: Simulation of the Dissipative Dynamics of Strongly Interacting NV Centers with Tensor Networks					
Status in publication process: Published					

Acknowledgements

It is hard to imagine reaching this point without the shoulders of giants upon which I stand. Thus, I would like to express my deepest gratitude to everyone who supported me and made the completion of this thesis possible.

First and foremost, I extend my heartfelt thanks to my supervisor, Prof. Daniel Braun, for giving me the opportunity to join his wonderful group in Tübingen. His insightful advice, valuable feedback, and unwavering support throughout my PhD journey have been invaluable. I have learned so much under his guidance.

I would also like to express my appreciation to my collaborators on this project, especially Dr. Ressa Sind, for our fruitful discussions, one of which became part of this thesis.

To my incredible friends and colleagues within the group, I owe a special thanks. In no particular order, I would like to mention Emre Köse, Matthias Hüls, Ricardo Bellese, Giovanni Gramegna, Jakub Czartowski, Alessio Belenchia, Felix Spengler, Francis Headley, Mahdi Rouhbakhshnabati, Erik Weiß, Lennart Becker, and Stanislaw Soltan, whose bug card game made our coffee breaks truly enjoyable. I also cherish the group activities we shared, including hiking, cycling, and parties, which brought so much joy to my time here.

Moving from Thailand to Germany and living far from home was a challenging journey. I am immensely thankful to my wonderful Mitbewohner, Yuee, Jonas, and Friedrich, who helped me adapt to this new environment with warmth and kindness, making the transition smooth and welcoming.

Last but not least, I would like to express my deepest gratitude to my family for their unconditional love, belief, and support throughout this journey. I am also thankful to my friends in Thailand for their emotional support, which kept me grounded. Finally, I thank myself for persevering and not giving up along the way.

Contents

Chapter 1

Framework

1.1 Introduction

This thesis focuses on ensembles of nitrogen-vacancy (NV) defects in diamond and investigates their application as high-sensitivity probe candidates in quantum metrology. The research presented herein encompasses several key areas: addressing a theoretical model for individual NV centers and their interactions; discussing efficient numerical methods for simulating NV ensembles with dissipation; investigating the time evolution and entanglement generation within systems of strongly interacting spins; and presenting results on the optimization of control pulses to achieve maximum sensitivity.

In metrology, achieving high sensitivity is crucial for enabling high-resolution sensing, such as probing magnetic fields at the nanoscale. By leveraging quantum phenomena, probes can theoretically surpass the sensitivity limitations of classical devices. One prominent candidate for realizing such quantum probes is the nitrogen-vacancy (NV) center in diamond. This crystallographic defect consists of a substitutional nitrogen atom adjacent to a lattice vacancy. The NV center can exist in two charge states: neutral (NV^0) and negative (NV^-) [47, 10]. Since there are two free valent electrons from the nitrogen atom and three electrons from the vacancy, four of them create two quasi pairs and one electron is left unpaired. The NV^0 state is paramagnetic with a net spin of 1/2. Upon capture of an additional electron, the NV center transitions to the NV^- state, which possesses a spin-triplet (S=1) ground state. This negatively charged state exhibits favorable optical properties, enabling efficient spin initialization and readout via optical means, which is highly advantageous for experiments. The utility of individual NV centers as atomic-scale magnetic field sensors has been well-established [46, 51, 11]. Consequently, this thesis primarily focuses on the NV^- state, and henceforth, "NV center" will refer to

NV^- unless explicitly stated otherwise.

To further enhance sensitivity, probes can be constructed using multiple NV centers. The successful fabrication of double and triple NV centers in close proximity has recently been reported [21]. Such arrangements of multiple NV centers constitute an NV ensemble. Utilizing NV ensembles holds the potential to boost sensitivity by increasing the number of sensing spins [1, 55, 50]. A quantum probe consisting of N independent spins exhibits sensitivity scaling according to the standard quantum limit (SQL), proportional to $1/\sqrt{N}$. However, reaching the ultimate sensitivity bound permitted by quantum mechanics, the Heisenberg limit (HL), which scales as $1/N$, requires exploiting entanglement among the constituent spins [20, 19, 18].

Achieving high spatial resolution necessitates the use of high-density NV ensembles. In such dense ensembles, the close proximity between NV centers facilitates significant dipole-dipole interactions. Bacause the strength of this interaction is inversely proportional to the cube of the distance between centers ($1/r^3$), it becomes substantial at the short separations characteristic of dense ensembles. However, these strong dipole-dipole interactions can lead to detrimental effects for sensing applications. Specifically, they drive rapid population transfer into Hilbert space subspaces with reduced total spin. For instance, in a system of two spin-1/2 particles, not only the triplet states would get populated, but also the anti-symmetric singlet state, resulting in a reduced collective response to the applied field. This interaction-induced population leakage acts as a form of intrinsic decoherence [56], compounding the effects of external decoherence mechanisms [2]. The combined result is a reduction in coherence times and, consequently, diminished sensing sensitivity.

Strategies such as applying specific control pulses to dynamically decouple interactions, or engineering specific NV alignments to minimize interaction strength, have been employed to mitigate these detrimental effects, thereby increasing coherence times and sensitivity [56, 13, 32]. Conversely, an alternative and potentially more desirable approach seeks to harness these interactions constructively. Ideally, interactions could be exploited to generate entangled states among the NV spins, which, as previously mentioned, are required to potentially enhance the probe's sensitivity towards the Heisenberg limit.

To model and optimize entanglement generation in a dissipative system with strong and long-range interactions, simulations of its dynamics in the presence of microwave control pulses is necessary. However, given the many-body nature of an ensemble, simulating its exact dynamics is intractable. Exact simulations of closed spin-1/2 systems with long-range interaction have been implemented up to 32 spins [41, 42, 56, 7], and up to 12 spins with dissipation [12, 26]. In order to address this challenge, we use a tensor network approach to capture the dynamics of the ensemble. Matrix Product States (MPS)[48, 35, 44, 31] were proposed for the efficient simulation of quantum metrology[24] and open quantum systems[14]. Simulation of non-Markovian systems has been performed using Matrix Product Operators (MPO) with a nearest-neighbors model [43, 17].

Generating and optimizing entanglement within NV ensembles, characterized by strong and long-range interactions and subject to microwave control pulses, requires simulating their quantum dynamics. However, the inherent many-body nature of these ensembles renders exact simulation computationally intractable, especially with dissipation, for systems beyond a modest size. While exact simulations have been achieved for closed spin-1/2 systems with long-range interactions comprising up to 32 spins [41, 42, 56, 7], this limit reduces significantly, to around 12 spins, when dissipation is included [12, 26]. To overcome this scalability challenge, this work employs a tensor network approach to efficiently approximate the ensemble dynamics. Tensor network methods, such as Matrix Product States (MPS) [48, 35, 44, 31], have proven effective for simulating quantum metrology protocols [24] and open quantum systems [14]. Furthermore, Matrix Product Operators (MPO) have been utilized for simulating non-Markovian dynamics, albeit restricted to models with nearest-neighbor interactions [43, 17].

This work focuses on an NV ensemble composed of spin-1 particles, where all constituents interact via long-range dipole-dipole interaction. We simulate the dissipative dynamics of this system using the Matrix Product Density Operator (MPDO) method. The efficiency and stability of the MPDO method is investigated, particularly for simulating dynamics under conditions of strong interactions and dissipation. We analyze the interplay between strong interactions and dissipation, assessing its impact on the resources required by the MPDO representation and its ability to accurately approximate the true quantum state. Subsequently, we quantify the potential sensitivity enhancements achievable through NV-NV interactions during the system's evolution. Finally, optimal control techniques are employed to devise strategies for accelerating the generation of entanglement within finite evolution times.

1.2 Nitrogen-vacancy center in diamond.

A nitrogen-vacancy (NV) center is a type of point defect in the diamond crystal structure. This defect is formed when two adjacent carbon atoms in the diamond lattice are replaced by a nitrogen atom and a vacant site. When an NV center gains an additional electron, it becomes negatively charged, resulting in optically active $S = 1$ spin states. The NV center exhibits long spin coherence times at room temperature and high sensitivity to magnetic fields, making it a promising platform for quantum sensing.

A single NV center can be fabricated using ion implantation techniques [23, 21]. Alternatively, ensembles of dipole-coupled NV centers can be created by employing nitrogen-rich molecules, which can be detected through higher photon intensities. Since the dipole coupling strength increases with decreasing distance, NV centers within an ensemble can interact via dipole-dipole interactions. These interactions are useful for entanglement generation and sensitivity enhancement in quantum metrology. Recent experiments have observed ensembles containing up to four NV centers [25]. However, achieving full control over these NV centers remains challenging due to local disorder.

The diamond's crystallographic structure allows for four possible NV principal axis orientations along the $\langle 111 \rangle$ axis. These orientations are typically formed randomly during NV center fabrication [45, 29], contributing to local disorder. Nevertheless, it is possible to grow NV centers with perfect alignment by employing chemical vapor deposition (CVD) techniques on (111) diamond substrates [16]. In the presence of interactions, the coherence times of NV centers are shortened. Therefore, precise control and dynamic simulations of strongly interacting systems are essential.

1.2.1 NV Hamiltonian

The local Hamiltonian for NV center is given by

$$\begin{aligned} \hat{H}_{NV} &= \hbar(D\hat{S}_z^2 + \gamma B_z \hat{S}_z) \qquad (1.1) \\ &= \begin{pmatrix} D+\gamma B_z & 0 & 0 \\ 0 & 0 & 0 \\ 0 & 0 & D-\gamma B_z \end{pmatrix} \qquad (1.2) \end{aligned}$$

The spin operators for $S = 1$ are defined as

$$\hat{S}_x = \frac{1}{\sqrt{2}} \begin{pmatrix} 0 & 1 & 0 \\ 1 & 0 & 1 \\ 0 & 1 & 0 \end{pmatrix}, \hat{S}_y = \frac{i}{\sqrt{2}} \begin{pmatrix} 0 & -1 & 0 \\ 1 & 0 & -1 \\ 0 & 1 & 0 \end{pmatrix}, \hat{S}_z = \begin{pmatrix} 1 & 0 & 0 \\ 0 & 0 & 0 \\ 0 & 0 & -1 \end{pmatrix}. \qquad (1.3)$$

The energy level structure of an individual NV center without an external magnetic field is determined by the eigenvalues and eigenvectors of the Hamiltonian in eq. (1.2). Since $\hat{H}_{NV}$ is diagonal, the eigenvalues $(D+\gamma B_z, 0, D-\gamma B_z)$ correspond to the energies of the eigenstates labeled by the electron spin m_s:

$$|m_s = 1\rangle = (1,0,0)^T \tag{1.4}$$

$$|m_s = 0\rangle = (0,1,0)^T \tag{1.5}$$

$$|m_s = -1\rangle = (0,0,1)^T. \tag{1.6}$$

The diamond structure separates the energy levels of the $|m_s = \pm 1\rangle$ states from the $|m_s = 0\rangle$ state by $D = (2\pi) \cdot 2.88$ GHz, known as the zero-field splitting frequency. Interaction with an external magnetic field applied along the NV axis introduces an additional Zeeman splitting between the $|m_s = +1\rangle$ and $|m_s = -1\rangle$ states, with a splitting amplitude of $2\gamma B_z$.

When an external microwave pulse is applied to the NV center at the resonant frequency, it can induce Rabi oscillations between the NV's ground state $|m_s = 0\rangle$ and the excited states $|m_s = \pm 1\rangle$, enabling information processing with the NV center's optical states.

1.2.2 Rotating Wave Approximation (RWA)

Consider a simplified model where an individual NV center is driven along the x-axis by a cosinusoidal pulse with frequency ω and amplitude Ω. The local Hamiltonian for the NV center, including the control field, is:

$$\hat{H}_{NV}^{(i)} = \hbar(D\hat{S}_z^2 + \gamma_e B_z \hat{S}_z + \Omega_x^{(i)} cos(\omega t)\hat{S}_x) \tag{1.7}$$

To eliminate the explicit time dependence, eq. (1.7) is transformed into a rotating frame using the unitary transformation.

$$\hat{U} = e^{-i\hat{A}t/\hbar}, \quad \text{where} \quad \hat{A} = \hbar\omega\hat{S}_z^2. \tag{1.8}$$

In the rotating frame, the Hamiltonian becomes:

$$\hat{H}_{rot} = \hat{U}^\dagger \left[\hat{H}_0 - \hat{A}\right] \hat{U}. \tag{1.9}$$

The index (i) is omitted since now there are only Hamiltonian of one NV. Let $\hat{H}_0 = \hbar(D\hat{S}^2 + \gamma B_z \hat{S}_z + \Omega\cos(\omega t)\hat{S}_x)$.

$$\begin{aligned}
\hat{H}_{rot} &= \hat{U}^\dagger \left[\hat{H}_0 - \hat{A}\right]\hat{U} \qquad (1.10)\\
&= \hbar \begin{bmatrix} e^{i\omega t} & 0 & 0 \\ 0 & 1 & 0 \\ 0 & 0 & e^{i\omega t} \end{bmatrix} \begin{bmatrix} D + \gamma B_z + \omega & \Omega\cos(\omega t)/\sqrt{2} & 0 \\ \Omega\cos(\omega t)/\sqrt{2} & 0 & \Omega\cos(\omega t)/\sqrt{2} \\ 0 & \Omega\cos(\omega t)/\sqrt{2} & D - \gamma B_z - \omega \end{bmatrix}\\
&\times \begin{bmatrix} e^{-i\omega t} & 0 & 0 \\ 0 & 1 & 0 \\ 0 & 0 & e^{-i\omega t} \end{bmatrix} \qquad (1.11)\\
&= \hbar \begin{bmatrix} D + \gamma B_z - \omega & \Omega\cos(\omega t)e^{i\omega t}/\sqrt{2} & 0 \\ \Omega\cos(\omega t)e^{-i\omega t}/\sqrt{2} & 0 & \Omega\cos(\omega t)e^{-i\omega t}/\sqrt{2} \\ 0 & \Omega\cos(\omega t)e^{i\omega t}/\sqrt{2} & D - \gamma B_z - \omega \end{bmatrix} \qquad (1.12)\\
&= \frac{\hbar}{2} \begin{bmatrix} 2[D + \gamma B_z - \omega] & \Omega(1 + e^{i2\omega t})/\sqrt{2} & 0 \\ \Omega(1 + e^{-i2\omega t})/\sqrt{2} & 0 & \Omega(1 + e^{i2\omega t})/\sqrt{2} \\ 0 & \Omega(1 + e^{-i2\omega t})/\sqrt{2} & 2[D - \gamma B_z - \omega] \end{bmatrix}. \qquad (1.13)
\end{aligned}$$

After applying the rotating wave approximation (RWA), which neglects rapidly oscillating terms, $e^{\pm i2\omega t} \approx 0$, the Hamiltonian simplifies to:

$$\begin{aligned}
\hat{H}_{rot} &= \frac{\hbar}{2} \begin{bmatrix} 2[D + \gamma B_z - \omega] & \frac{\Omega}{\sqrt{2}} & 0 \\ \frac{\Omega}{\sqrt{2}} & 0 & \frac{\Omega}{\sqrt{2}} \\ 0 & \frac{\Omega}{\sqrt{2}} & 2[D - \gamma B_z - \omega] \end{bmatrix}, \qquad (1.14)\\
&= \frac{\hbar}{2} \begin{bmatrix} 2(\Delta_+ - \omega) & \frac{\Omega_x}{\sqrt{2}} & 0 \\ \frac{\Omega_x}{\sqrt{2}} & 0 & \frac{\Omega_x}{\sqrt{2}} \\ 0 & \frac{\Omega_x}{\sqrt{2}} & 2(\Delta_- - \omega) \end{bmatrix}. \qquad (1.15)
\end{aligned}$$

By choosing a pulse at the resonant frequencies $\omega = \Delta_\pm = D \pm \gamma B_z$, Rabi oscillations can be generated between $|m_s = 0\rangle$ and $|m_s = \pm 1\rangle$.

$$\begin{aligned}
\hat{H}_{rot}(\omega = \Delta_+) &= \frac{\hbar}{2} \begin{bmatrix} 0 & \frac{\Omega_x}{\sqrt{2}} & 0 \\ \frac{\Omega_x}{\sqrt{2}} & 0 & \frac{\Omega_x}{\sqrt{2}} \\ 0 & \frac{\Omega_x}{\sqrt{2}} & -4\gamma B_z \end{bmatrix}, \qquad (1.16)\\
\hat{H}_{rot}(\omega = \Delta_-) &= \frac{\hbar}{2} \begin{bmatrix} 4\gamma B_z & \frac{\Omega_x}{\sqrt{2}} & 0 \\ \frac{\Omega_x}{\sqrt{2}} & 0 & \frac{\Omega_x}{\sqrt{2}} \\ 0 & \frac{\Omega_x}{\sqrt{2}} & 0 \end{bmatrix}. \qquad (1.17)
\end{aligned}$$

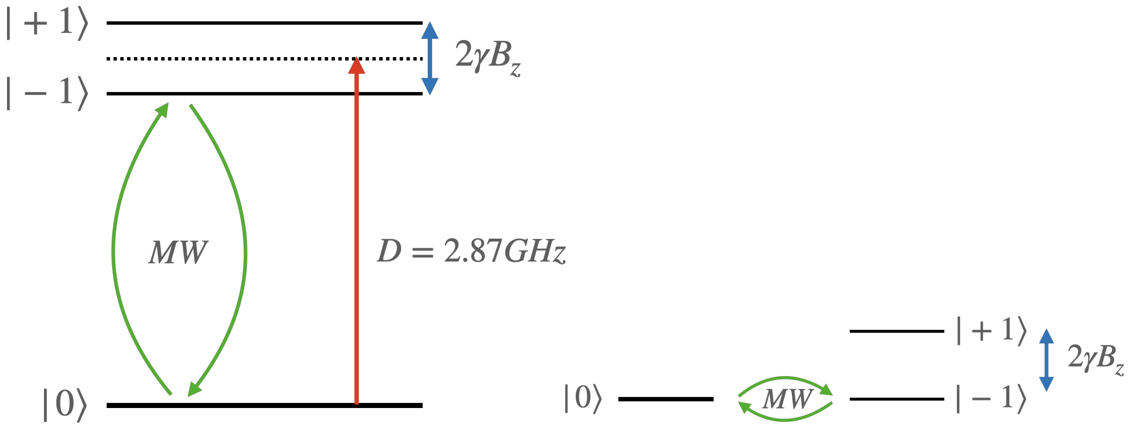

(a) Lab frame **(b)** Rotating frame

Figure 1.1: Energy levels of an NV center in the lab frame and the rotating frame. The zero-field splitting separates $|m_s = 0\rangle$ and $|m_s = \pm 1\rangle$ by 2.87 GHz. In the absence of an external magnetic field, the $|m_s = \pm 1\rangle$ states are degenerate. Otherwise, the Zeeman effect splits them by $2\gamma B_z$. A microwave drive with frequency $\omega = D - \gamma B_z$ induces Rabi oscillations between $|m_s = 0\rangle$ and $|m_s = -1\rangle$.

If the magnetic field is strong enough ($B_z \gg \Omega$), the off-resonant states are far detuned, and the system can be approximated as an effective qubit system. Conversely, in the absence of a magnetic field ($B_z = 0$), the two degenerate excited states $|m_s = \pm 1\rangle$ are equally driven:

$$\hat{H}_{rot}(B_z = 0) = \frac{\hbar}{2} \begin{bmatrix} 0 & \frac{\Omega}{\sqrt{2}} & 0 \\ \frac{\Omega}{\sqrt{2}} & 0 & \frac{\Omega}{\sqrt{2}} \\ 0 & \frac{\Omega}{\sqrt{2}} & 0 \end{bmatrix}. \tag{1.18}$$

This result can be extended to multiple spins by summing the individual transformations:

$$\hat{A} = \sum_{i=1}^{N} \hat{A}_i \tag{1.19}$$

1.3 Interaction Hamiltonian

1.3.1 Dipole-dipole interaction

NV centers, randomly distributed within the diamond lattice, are typically located far apart and rarely interact without an additional interaction channel. This is because their interaction is relatively weak for pairs of NV centers with large spatial separations. This scenario is common for NV centers in different ensembles, where the separation scale is on the order of a few microns. However, the interaction becomes significantly stronger when the separation is reduced to the nanometer scale, which is 100 times smaller. This is due to the interaction strength scaling as $1/r^3$. For instance, when two NV centers are located within the same ensemble, their close proximity enables strong dipole-dipole interactions. An ensemble within the diamond lattice containing multiple NV centers can exhibit such interactions.

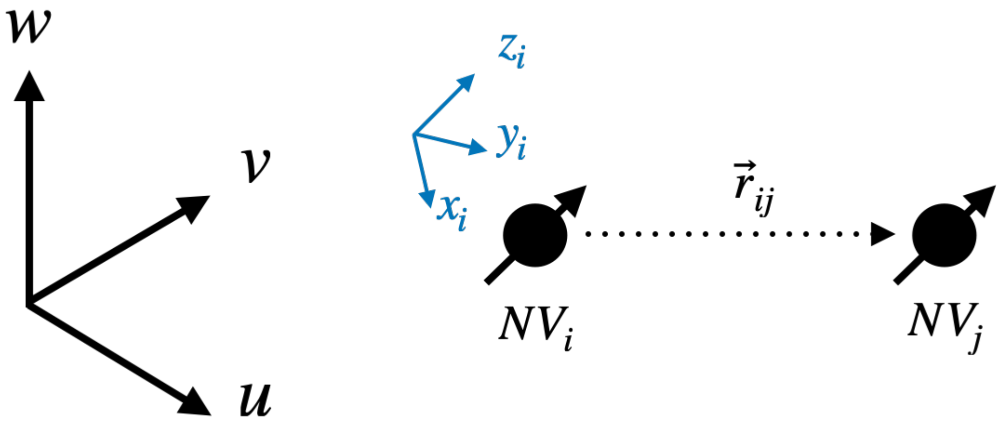

Figure 1.2: (Black) Coordinate system in the laboratory frame. (Blue) Coordinate system aligned along the symmetric axis of each spin.

The dipole-dipole interaction between two NV centers, NV_i and NV_j, is generally defined as:

$$H_{dip,ij} = -\frac{\mu_0 \gamma^2 \hbar^2}{4\pi r_{ij}^3}(3(\vec{S}_i \cdot \hat{r})(\vec{S}_j \cdot \hat{r}) - \vec{S}_i \vec{S}_j) \tag{1.20}$$

where $\vec{S}_{i(j)} = (\hat{S}_x, \hat{S}_y, \hat{S}_z)_{i(j)}$ are the spin operators of NV$_i$ and NV$_j$, and $\hat{r}$ is the unit vector connecting the two NV centers. In eq. (1.20), the spin vectors $\vec{S}_i$ and $\vec{S}_j$ are defined in a coordinate system where $\hat{z}_{i(j)}$ is parallel to their respective principal axes. For example, if the principal axis of NV$_i$ is aligned along the [111] crystallographic direction, then:

$$\vec{S}_i = \hat{S}_x \hat{x}_i + \hat{S}_y \hat{y}_i + \hat{S}_z \hat{z}_i, \tag{1.21}$$

where $\hat{z}_i \parallel \left(\frac{1}{\sqrt{3}}, \frac{1}{\sqrt{3}}, \frac{1}{\sqrt{3}}\right)$. The axes $\hat{x}_i$ and $\hat{y}_i$ are defined through a coordinate transformation. Let us define a common coordinate system, denoted as $(\hat{u}, \hat{v}, \hat{w})$, in which the operators are expressed:

$$\hat{u} = (1, 0, 0), \tag{1.22}$$
$$\hat{v} = (0, 1, 0), \tag{1.23}$$
$$\hat{w} = (0, 0, 1). \tag{1.24}$$

The transformation between the common coordinate system $(\hat{u}, \hat{v}, \hat{w})$ and the local coordinate system $(\hat{x}_i, \hat{y}_i, \hat{z}_i)$ is achieved by applying a rotational matrix $\hat{R}(\theta_i)$, such that:

$$\hat{R}(\theta_i)\hat{u} = \hat{x}_i \tag{1.25}$$
$$\hat{R}(\theta_i)\hat{v} = \hat{y}_i \tag{1.26}$$
$$\hat{R}(\theta_i)\hat{w} = \hat{z}_i. \tag{1.27}$$

The rotational matrix $\hat{R}(\theta)$ can be efficiently computed when $\hat{w}$ and $\hat{z}_i$ are known. Using Rodrigues' rotation formula [8], the matrix is given by:

$$\hat{R}(\theta) = \hat{I} + \sin(\theta)\hat{K} + (1 - \cos(\theta))\hat{K}^2, \tag{1.28}$$

where $\hat{K}$ is an anti-symmetric matrix defined as:

$$\hat{K} = \begin{bmatrix} 0 & -k_z & k_y \\ k_z & 0 & -k_x \\ -k_y & k_x & 0 \end{bmatrix}. \tag{1.29}$$

The elements of $\hat{K}$ are determined from $\hat{w}$ and $\hat{z}_i$ as follows:

$$\begin{pmatrix} k_x \\ k_y \\ k_z \end{pmatrix} = \frac{\hat{w} \times \hat{z}_i}{|\hat{w} \times \hat{z}_i|}. \tag{1.30}$$

Finally, the interaction Hamiltonian in eq. (1.20) can account for different principal axis orientations by mapping $\vec{S}_i \to \hat{R}_i \cdot \vec{S}_i$ and $\vec{S}_j \to \hat{R}_j \cdot \vec{S}_j$.

$$\begin{aligned}\hat{H}_{dip,ij} = \frac{C_{\text{dip}}}{r_{ij}^3}[\, &(\hat{x}_i \cdot \hat{x}_j - 3(\hat{x}_i \cdot \hat{r})(\hat{x}_j \cdot \hat{r}))\,\hat{S}_x\hat{S}_x \\ &(\hat{y}_i \cdot \hat{y}_j - 3(\hat{y}_i \cdot \hat{r})(\hat{y}_j \cdot \hat{r}))\,\hat{S}_y\hat{S}_y \\ &(\hat{x}_i \cdot \hat{y}_j - 3(\hat{x}_i \cdot \hat{r})(\hat{y}_j \cdot \hat{r}))\,\hat{S}_x\hat{S}_y \\ &(\hat{y}_i \cdot \hat{x}_j - 3(\hat{y}_i \cdot \hat{r})(\hat{x}_j \cdot \hat{r}))\,\hat{S}_y\hat{S}_x \\ &(\hat{z}_i \cdot \hat{z}_j - 3(\hat{z}_i \cdot \hat{r})(\hat{z}_j \cdot \hat{r}))\,\hat{S}_z\hat{S}_z \\ &(\hat{z}_i \cdot \hat{x}_j - 3(\hat{z}_i \cdot \hat{r})(\hat{x}_j \cdot \hat{r}))\,\hat{S}_z\hat{S}_x \\ &(\hat{x}_i \cdot \hat{z}_j - 3(\hat{x}_i \cdot \hat{r})(\hat{z}_j \cdot \hat{r}))\,\hat{S}_x\hat{S}_z \\ &(\hat{z}_i \cdot \hat{y}_j - 3(\hat{z}_i \cdot \hat{r})(\hat{y}_j \cdot \hat{r}))\,\hat{S}_z\hat{S}_y \\ &(\hat{y}_i \cdot \hat{z}_j - 3(\hat{y}_i \cdot \hat{r})(\hat{z}_j \cdot \hat{r}))\,\hat{S}_y\hat{S}_z \\ ]\end{aligned} \tag{1.31}$$

1.3.2 Effective Interaction of a Driven NVs system

Transitioning into the rotating frame, the dipolar Hamiltonian transforms as:

$$\hat{H}_{\text{dip}} \to \hat{U}^\dagger(t)\hat{H}_{\text{dip}}\hat{U}(t) \tag{1.32}$$

under the unitary transformation $\hat{U} = \exp\left(-it\sum_i \omega_i(\hat{S}_z^{(i)})^2\right)$. The Hamiltonian in eq. (1.31) can then be simplified using the rotating wave approximation (RWA).

It is important to note that, while considering the interaction of NV centers separated at the nanoscale, the driving frequency $\omega \approx (2\pi)2.6$–3 GHz remains significantly stronger than the interaction strength. For example, $|\frac{C_{\text{dip}}}{r^3}| \approx (2\pi)6.5$ MHz at $r = 2$ nm. Furthermore, since $[\hat{S}_z, \hat{U}] = 0$, the operator $\hat{S}_z$ remains invariant in this frame. Consequently, the components $\hat{S}_x$ and $\hat{S}_y$ oscillate rapidly compared to $\hat{S}_z$, justifying the use of the RWA. As a result, the terms $\hat{S}_z\hat{S}_x$, $\hat{S}_x\hat{S}_z$, $\hat{S}_z\hat{S}_y$, and $\hat{S}_y\hat{S}_z$ in eq. (1.31) can be neglected. The approximated interaction Hamiltonian then becomes:

$$\begin{aligned}\hat{H}_{\text{dip}} \approx &\frac{C_{\text{dip}}}{r^3}[g^+(S_xS_x + S_yS_y) + h^-(S_xS_y - S_yS_x) + qS_zS_z \\ &+ g^-(S_xS_x - S_yS_y) + h^+(S_xS_y + S_yS_x)]\end{aligned} \tag{1.33}$$

where the coefficients are defined as:

$$g^+ = \frac{1}{2}\left[\hat{x}_i \cdot \hat{x}_j - 3(\hat{r} \cdot \hat{x}_i)(\hat{r} \cdot \hat{x}_j) + \hat{y}_i \cdot \hat{y}_j - 3(\hat{r} \cdot \hat{y}_i)(\hat{r} \cdot \hat{y}_j)\right] \tag{1.34}$$

$$g^- = \frac{1}{2}\left[\hat{x}_i \cdot \hat{x}_j - 3(\hat{r} \cdot \hat{x}_i)(\hat{r} \cdot \hat{x}_j) - \hat{y}_i \cdot \hat{y}_j + 3(\hat{r} \cdot \hat{y}_i)(\hat{r} \cdot \hat{y}_j)\right] \tag{1.35}$$

$$h^+ = \frac{1}{2}\left[\hat{x}_i \cdot \hat{y}_j - 3(\hat{r} \cdot \hat{x}_i)(\hat{r} \cdot \hat{y}_j) + \hat{y}_i \cdot \hat{x}_j - 3(\hat{r} \cdot \hat{y}_i)(\hat{r} \cdot \hat{x}_j)\right] \tag{1.36}$$

$$h^- = \frac{1}{2}\left[\hat{x}_i \cdot \hat{y}_j - 3(\hat{r} \cdot \hat{x}_i)(\hat{r} \cdot \hat{y}_j) - \hat{y}_i \cdot \hat{x}_j + 3(\hat{r} \cdot \hat{y}_i)(\hat{r} \cdot \hat{x}_j)\right] \tag{1.37}$$

$$q = \hat{z}_i \cdot \hat{z}_j - 3(\hat{r} \cdot \hat{z}_i)(\hat{r} \cdot \hat{z}_j) \tag{1.38}$$

To simplify further, we first ignore the interaction terms in eq. (1.36) and eq. (1.35), which correspond to double flip-flop transitions. The dipolar Hamiltonian is then approximated as:

$$\hat{H}_{\text{dip}} \approx \frac{C_{\text{dip}}}{r^3}[g^+(S_xS_x + S_yS_y) + h^-(S_xS_y - S_yS_x) + qS_zS_z]. \tag{1.39}$$

Next, we consider two distinct cases. The first case involves two NV centers with the same orientation, where $\hat{k}_i = \hat{k}_j$ for $\hat{k} \in (\hat{x}, \hat{y}, \hat{z})$, and:

$$\hat{k}_i \cdot \hat{k}_j = \begin{cases} 1, & i = j, \\ 0, & i \neq j. \end{cases}$$

Under these conditions, eq. (1.34), eq. (1.37), and eq. (1.38) simplify as follows:

$$g^+ = \frac{1}{2}\left[1 - 3(\hat{r} \cdot \hat{x})^2 + 1 - 3(\hat{r} \cdot \hat{y})^2\right] \tag{1.40}$$

$$= \frac{1}{2}\left[2 - 3(1 - (\hat{r} \cdot \hat{z})^2)\right] \tag{1.41}$$

$$= \frac{1}{2}(3(\hat{r} \cdot \hat{z})^2 - 1) \tag{1.42}$$

$$h^- = \frac{1}{2}\left[0 - 3(\hat{r} \cdot \hat{x})(\hat{r} \cdot \hat{y}) - 0 + 3(\hat{r} \cdot \hat{y})(\hat{r} \cdot \hat{x})\right] \tag{1.43}$$

$$= 0 \tag{1.44}$$

$$q = 1 - 3(\hat{r} \cdot \hat{z})^2 \tag{1.45}$$

Here, we rewrite $\cos\theta \equiv \hat{r} \cdot \hat{z}$, where θ is the angle between the principal axis of the

NV centers and the connecting vector. Substituting these results, we obtain:

$$(\hat{x}_i, \hat{y}_i, \hat{z}_i) = (\hat{x}_j, \hat{y}_j, \hat{z}_j) \tag{1.46}$$

$$g^+ = \frac{1}{2}(3\cos^2\theta - 1) \tag{1.47}$$

$$h^- = 0 \tag{1.48}$$

$$q = -(3\cos^2\theta - 1) \tag{1.49}$$

$$\hat{H}_{\text{dip}} = \frac{C_{\text{dip}} q}{r^3}[S_z S_z - \frac{1}{2}(S_x S_x + S_y S_y)] \tag{1.50}$$

The second case involves NV centers with different orientations. In this scenario, the large inhomogeneous energy levels compared to the coupling constant, $|E_{|00\rangle \to |-10\rangle} - E_{|00\rangle \to |0-1\rangle}| \gg \frac{C_{\text{dip}}}{r^3}$, justify the secular approximation. This allows us to eliminate the flip-flop interaction terms in eq. (1.34) and eq. (1.37), leaving only the $\hat{S}_z \hat{S}_z$ term. This condition is valid in the presence of a strong magnetic field $|\vec{B}|$, where the Zeeman effect dominates the interaction:

$$\hat{H}_{\text{dip}} = \frac{C_{\text{dip}} q}{r^3} S_z S_z. \tag{1.51}$$

In summary, the effective Hamiltonian for dipole-dipole interaction between two NV centers, depending on whether they share the same or different principal axes, is given by:

$$\hat{H}_{dip,eff} = \begin{cases} \frac{C_{\text{dip}} q}{r^3}[S_z S_z - \frac{1}{2}(S_x S_x + S_y S_y)] & \text{Same} \\ \frac{C_{\text{dip}} q}{r^3} S_z S_z & \text{Different} \end{cases}. \tag{1.52}$$

1.4 Exact Diagonalization

In this section, we discuss an exact numerical method for simulating many-body problems and its limitations. For small system sizes, exact calculation is a precise method that provides highly accurate results. Since it does not introduce any approximation errors, this technique is often used as a benchmark for evaluating the accuracy of other methods.

The exact dynamics of a system can be obtained from its Hamiltonian by diagonalizing the Hamiltonian. This approach is referred to as the *Exact Diagonalization* method. From Schrödinger's equation, the quantum state evolves in time according to a unitary operator (in natural units, $\hbar = 1$):

$$|\psi(t+dt)\rangle = U(dt)|\psi(t)\rangle \tag{1.53}$$

$$= e^{-i\hat{H}dt}|\psi(t)\rangle \tag{1.54}$$

Thus, obtaining $U(t) = e^{-i\hat{H}t}$ becomes a central problem in solving the system's dynamics. The most straightforward approach is diagonalization, assuming that $\hat{H}$ is diagonalizable:

$$\hat{H} = PDP^{\dagger} \tag{1.55}$$

where $\hat{H}$ has dimensions $n \times n$, $D = \mathrm{diag}(\lambda_1, \cdots, \lambda_n)$ is a diagonal matrix of eigenvalues, and P is a unitary matrix whose columns are the eigenvectors corresponding to the eigenvalues in D. Using this decomposition, the unitary operator $U(t)$ can be computed as:

$$e^{-i\hat{H}dt} = e^{-i(UDU^{\dagger})dt} \tag{1.56}$$

$$= Pe^{-iDdt}P \tag{1.57}$$

Since D is a diagonal matrix, the exponentiation $e^{D} = \mathrm{diag}(e^{\lambda_1}, \cdots, e^{\lambda_n})$ is simply a diagonal matrix with the exponentiated diagonal elements.

Although this method is powerful, finding the matrix diagonalization for many-body Hamiltonians scales exponentially, which limits its applicability to small system sizes. For a system consisting of N spins, where each spin has d local degrees of freedom, the total number of spin configurations is d^N, and the Hamiltonian has dimensions $d^N \times d^N$. For example, a spin-1 NV center has $d = 3$. The memory required to store the entire Hamiltonian for 10 spins is approximately 55.8 GB. This estimate assumes that each element is a complex number with double precision and that no symmetries are exploited.

Bytes per one complex with double precisions.	**N**	d^N	**RAM needed**	$d^N \times d^N$	**RAM needed**
16	2	9	0.144KB	81	1.296KB
16	3	27	0.432KB	729	11.664KB
16	4	81	1.296KB	6561	104.976KB
16	5	243	3.888KB	59049	944.784KB

16	6	729	11.664KB	531441	8.503MB
16	7	2187	34.992KB	4782969	76.528MB
16	8	6561	104.976KB	43046721	688.748MB
16	9	19683	314.928KB	387420489	6.199GB
16	10	59049	944.784KB	3486784401	55.789GB

Table 1.1: Memory requirements illustrating the exponential scaling of exact diagonalization.

1.5 Tensor Network

The simulation intractability due to exponential scaling in the exact method suggests another approach with better scaling is required if one need to go beyond the small system limit. In the past, a powerful tensor network based technique was purposed for the system with low entanglement. In this section, we present how to simulate a quantum many-body system with tensor networks.

1.5.1 Tensor and tensor operations

While there exists a more mathematically rigorous definition, in this thesis, we adopt a computationally friendly definition. A tensor is defined as a multi-dimensional array of numbers, labeled by indices. The number of indices determines the rank of a tensor. Specifically, tensors are generalization referred to as rank-3 or higher arrays, while lower-rank tensors are typically categorized as follows:

- Rank-0: scalar.
- Rank-1: a vector.
- Rank-2: a matrix.

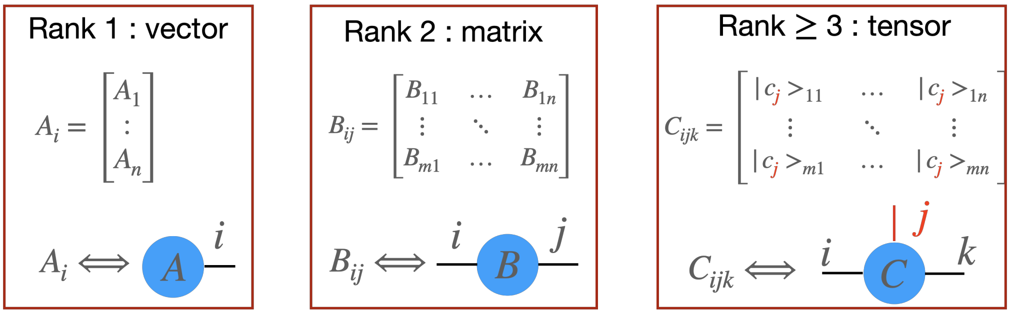

Figure 1.3: Examples of tensors with ranks 1, 2, and 3.

The visualization of a tensor is often represented as an object with lines (or legs), as shown in fig. 1.3. Each leg symbolizes an index of the tensor. Several operations can be performed on tensors, including:

1. *Contraction*: The most common operation involving tensors is tensor contraction, which is depicted by connecting legs. Contracted legs represent indices that are summed over between tensors. For example, the contraction of one index between two rank-2 tensors corresponds to matrix multiplication:

$$C_{ik} = \sum_j A_{ij} B_{jk}, \tag{1.58}$$

while the contraction of two indices within the same tensor corresponds to the trace:

$$\mathrm{Tr}[C] = \sum_i C_{ii} \tag{1.59}$$

The computational cost of performing a contraction between tensors A and B is given by:

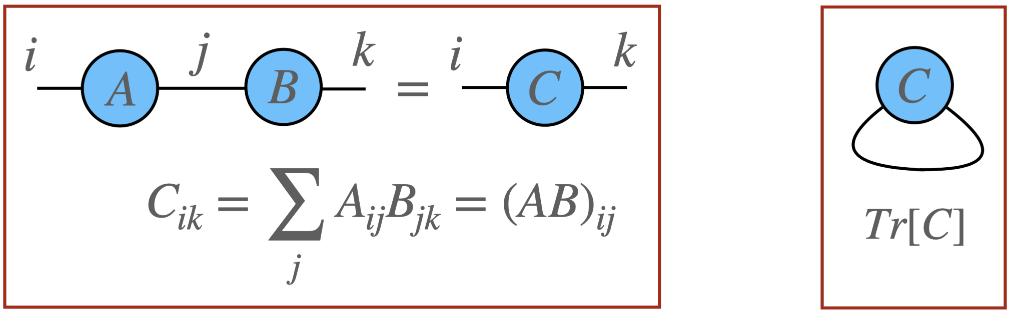

Matrix multiplication

Trace

Figure 1.4: Illustration of tensor contraction.

$$\begin{align}
\text{cost} : (A \times B) &= \frac{\dim(A)\dim(B)}{\dim(A \cap B)}, \tag{1.60}\\
\dim(A) &= \{\textstyle\prod \dim(s); s \in \text{legs of A}\}, \tag{1.61}\\
\dim(A \cap B) &= \{\textstyle\prod \dim(s); s \in \text{contracted legs between } A \text{ and } B\}. \tag{1.62}
\end{align}$$

The order of contractions can significantly affect computational costs. Finding the optimal contraction path is, in general, an NP-hard problem for complex tensor networks.

2. *Reshaping*: The indices of a tensor can be combined or split. In a tensor, only neighboring indices can be reshaped. The reshaping operation is often used

to change the shape of a tensor without altering its data. Examples of this operation include creating a matrix or vectorizing a tensor:

$$A = \sum_{i,j} A_{ij} \xrightarrow{vectorize} \vec{A} = \sum_{k=(i,j)} \rho_k \tag{1.63}$$

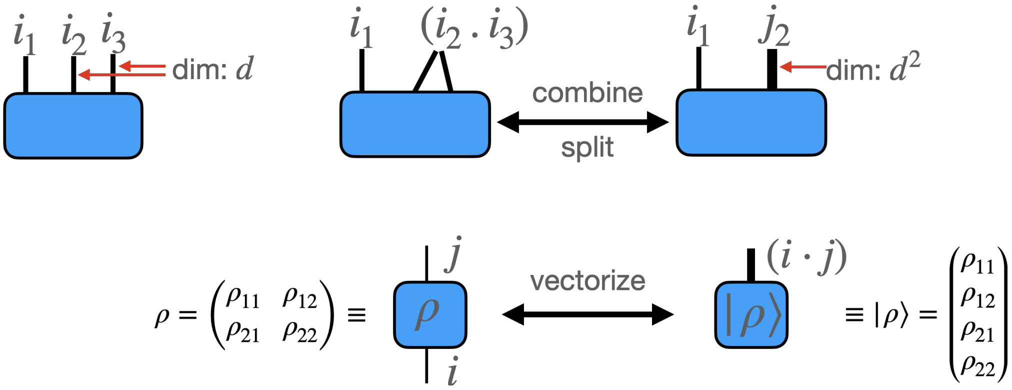

Figure 1.5: Illustration of tensor reshaping.

3. *Transpose*: This operation swaps the order of indices. The transpose operation is commonly used to rearrange the indices of a tensor. For example, the transpose of a rank-3 tensor A_{ijk} is denoted as A_{ikj}, where the second and third indices are swapped:

$$A_{ijk} \xrightarrow{transpose(j,k)} A_{ikj} \tag{1.64}$$

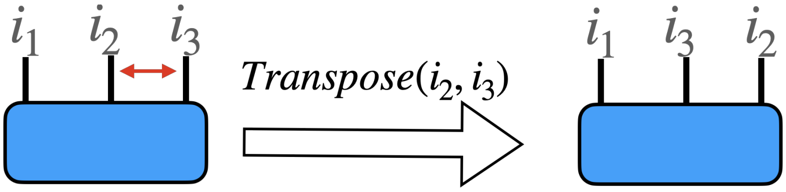

Figure 1.6: Illustration of tensor transposition.

1.6 Matrix Product States (MPS)

Let $|\psi\rangle$ be the wavefunction of a quantum system consisting of N spins $\{s_1, \cdots, s_N\}$, where the size of the local Hilbert space is $\dim(|s_l\rangle) = d$. The

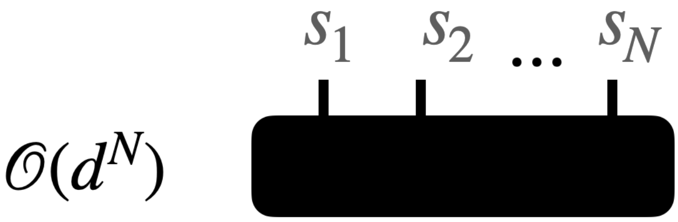

Figure 1.7: Diagram of $C_{s_1,\cdots,s_N}$ in eq. (1.65).

wavefunction $|\psi\rangle$ can be expressed as a summation of states in an orthogonal basis:

$$|\psi>= \sum_{s_1,\cdots,s_N} C_{s_1,\cdots,s_N}|s_1\cdots s_N\rangle \tag{1.65}$$

Here, $C_{s_1,\cdots,s_N}$ is a multi-dimensional array of state coefficients. The dimension of $C_{s_1,\cdots,s_N}$ is given by $\dim(C_{s_1,\cdots,s_N}) = \dim(|s_l\rangle)\otimes\cdots\otimes\dim(|s_N\rangle) = d^N$.

Example 1 *For* $d = 2$*,*

$$N=1: \quad |\psi\rangle = C_0|0\rangle + C_1|1\rangle \tag{1.66}$$

$$N=2: \quad |\psi\rangle = C_{00}|00\rangle + C_{01}|01\rangle + C_{10}|10\rangle + C_{11}|11\rangle \tag{1.67}$$

$$N=N: \quad |\psi\rangle = \sum_{s}^{2^N} C_i|s\rangle \tag{1.68}$$

where $s \in \mathcal{H}^{s_1\otimes\cdots\otimes s_N}$*. In vector form,* $C_s = \begin{bmatrix} C_1 & \dots & C_n \end{bmatrix}^T$*.*

The Matrix Product State (MPS) is a one-dimensional tensor network structure that represents $C_{s_1,\cdots,s_N}$ in eq. (1.65) as a product of matrices:

$$C_{s_1,\cdots,s_N} = \sum_{(\alpha_1,\cdots,\alpha_N)} Tr\left[A^{[1]}_{i_1,\alpha_1}A^{[2]}_{\alpha_1,i_2,\alpha_2}\dots A^{[N]}_{\alpha_{N-1},i_N,\alpha_N}\right] \tag{1.69}$$

$$= Tr[A^{s_1}_1 A^{s_2}_2 \dots A^{s_N}_N] \tag{1.70}$$

where the term *Matrix Product* refers to the matrix multiplication of A_l and A_{l+1}, which in this case are matrices of the physical state $|s\rangle$. From now on, $s_l \in (s_1,\cdots,s_N)$ is referred to as the *physical index*, as it indexes the local Hilbert space. The index $\alpha_l \in (\alpha_1,\cdots,\alpha_N)$ is called the *bond index*, with bond dimension $\dim(\alpha_l) = \chi_l$. In this MPS form, the dimension $\dim(C_{s_1,\cdots,s_N}) = Nd\chi^2$, assuming all bonds have uniform dimension $\chi_l = \chi$. This implies that χ must scale exponentially for the same N to be as fully expressive as d^N:

$$\chi_{\text{full}} = \frac{d^{(N-1)/2}}{N^{1/2}} \tag{1.71}$$

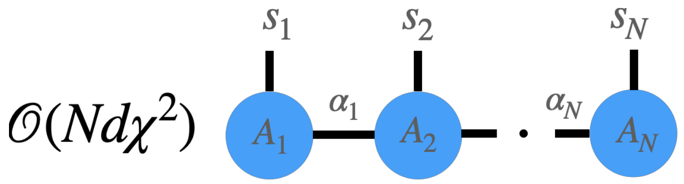

Figure 1.8: MPS representation of $C_{s_1,\cdots,s_N}$ in eq. (1.70).

1.6.1 MPS construction

It can be shown that, by repetitively applying Singular Value Decomposition (SVD) between physical legs, any pure state can be faithfully decomposed into an MPS. The procedure, as demonstrated in fig. 1.9, involves the following steps:

1. Starting from the leftmost physical leg s_1, combine all legs except s_1 into a single entity. This step is equivalent to reshaping the tensor C into a matrix.

2. Perform an SVD on the matrix C. Thus, $C_{i_1,(i_2,\cdots,i_N)} \to A_{s_1,\alpha_1}\Lambda_{\alpha_1}V^T_{\alpha_1,(i_2,\cdots,i_N)}$.

3. The singular tensor Λ_{α_1} can be absorbed into A (or V^T) to define the MPS in right (or left) canonical form. This demonstrates that MPS representations are not unique for the same pure state.

4. Repeat the above steps for the remaining physical legs.

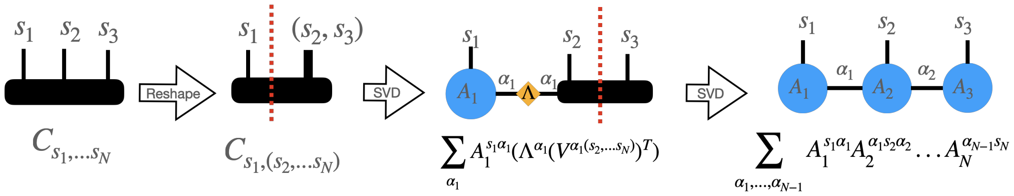

Figure 1.9: Procedure to decompose the coefficients of a full state $C_{s_1,\cdots,s_N}$ into an MPS. The figure illustrates the case for $N = 3$.

In practice, constructing an MPS from SVD is computationally inefficient, especially when N is large. The coefficients of the full state $C_{(s_1,\cdots,s_N)}$ are often unavailable due to memory constraints. Fortunately, many well-known states have analytic MPS forms that can be used directly. For example, a product state has an MPS form with bond dimension $\chi = 1$:

$$|\Psi\rangle = |\psi_1\rangle|\psi_2\rangle|\psi_3\rangle, \tag{1.72}$$

$$A_{s_1} = [|\psi_1\rangle], A_{s_2} = [|\psi_2\rangle], A_{s_3} = [|\psi_3\rangle]. \tag{1.73}$$

Another example is the maximally entangled state, also known as the GHZ state, which has an MPS form with bond dimension $\chi = 2$:

$$|\Psi\rangle = \frac{1}{\sqrt{2}}|0\rangle|0\rangle|0\rangle + \frac{1}{\sqrt{2}}|1\rangle|1\rangle|1\rangle \tag{1.74}$$

$$A_1 = \frac{1}{\sqrt{2}}\begin{pmatrix}|0\rangle & |1\rangle\end{pmatrix}, \tag{1.75}$$

$$A_2 = \begin{pmatrix}|0\rangle & 0 \\ 0 & |1\rangle\end{pmatrix}, \tag{1.76}$$

$$A_3 = \begin{pmatrix}|0\rangle \\ |1\rangle\end{pmatrix}. \tag{1.77}$$

1.6.2 Truncation

By the nature of the MPS in canonical form, the bond index contains singular values obtained via SVD. This allows for compression of the MPS by discarding the smallest singular values and their respective eigenvectors, as shown in fig. 1.10. In other words, using MPS enables an approximation of a pure state $|\psi\rangle$ with reduced dimensions. The error of this approximation, called the *truncation error*, is equal to the sum of the squares of the discarded singular values:

$$\epsilon = \sqrt{\sum_{k>\chi}(\Lambda_k)^2} \tag{1.78}$$

Physically, the truncation error is small if the state satisfies the area-law entanglement and the interaction range is finite. In such cases, the state evolves over time while the bond dimensions grow only slightly with small singular values. Bond truncation allows us to limit the size of the matrices required during each step of quantum state evolution. If the maximum allowed bond dimension $\chi_{\max}$ is constant, the dimension of the total state $\propto Nd\chi^2$ scales linearly with the system size N. This is the reason why MPS is efficient for simulating systems with low entanglement.

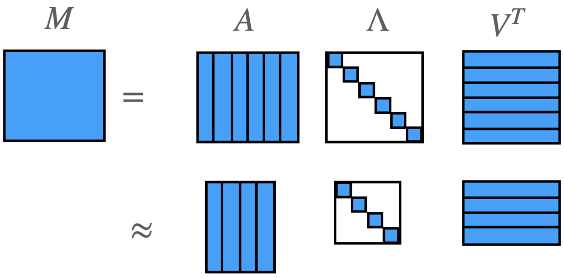

Figure 1.10: MPS can be compressed by truncating singular values within bonds and the corresponding elements with physical indices.

1.7 Matrix Product Operators (MPOs)

Similar to the MPS representation for a wavefunction, explained in section 1.6, a Hamiltonian can also be represented in a one-dimensional tensor network structure. The *Matrix Product Operator* (MPO) of an operator $\hat{O}$ is defined as

$$\hat{O}^{s'_1,\cdots,s'_N}_{s_1,\ldots,s_N} = \sum_{<\alpha_i>=1}^{\chi} W^{s'_1}_{[1]s_1\alpha_1} W^{s'_2}_{[2]\alpha_1 s_2 \alpha_2} \ldots W^{s'_N}_{[N]\alpha_{N-1} s_N \alpha_N} \tag{1.79}$$

where χ is the bond dimension. fig. 1.11 illustrates the tensor diagram for eq. (1.79) when $N = 3$.

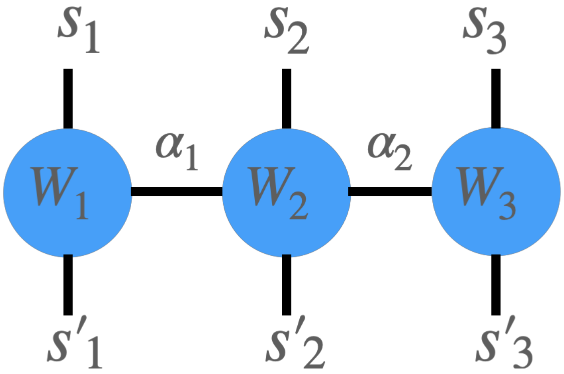

Figure 1.11: Tensor diagram for an MPO when $N = 3$.

Unlike in MPS, the bond dimension of an MPO is determined by the longest interaction range present in the Hamiltonian.

Example 2 *MPO of local Hamiltonian*

For a Hamiltonian written as a sum of local terms without interaction terms, the MPO can be constructed with a maximum bond dimension $\chi = 2$:

$$\hat{H}_{\text{loc}} = \sum_i \hat{X}_i, \tag{1.80}$$

$$W^{[1]} = \begin{pmatrix} I & \hat{X} \end{pmatrix}, W^{[i]} = \begin{pmatrix} I & \hat{X} \\ 0 & I \end{pmatrix}, W^{[N]} = \begin{pmatrix} \hat{X} \\ I \end{pmatrix}, \tag{1.81}$$

It is straightforward to verify, by multiplying all matrices, that eq. (1.81) reproduces the local Hamiltonian. For $N = 3$:

$$W^{[1]}W^{[2]}W^{[3]} = \begin{pmatrix} I_1 & \hat{X}_1 \end{pmatrix} \begin{pmatrix} I_2 & \hat{X}_2 \\ 0 & I_2 \end{pmatrix} \begin{pmatrix} \hat{X}_3 \\ I_3 \end{pmatrix} \tag{1.82}$$

$$= \begin{pmatrix} I_1 & \hat{X}_1 \end{pmatrix} \begin{pmatrix} I_2\hat{X}_3 + \hat{X}_2 I_3 \\ I_2 I_3 \end{pmatrix} \tag{1.83}$$

$$= \hat{X}_1 I_2 I_3 + I_1 \hat{X}_2 I_3 + I_1 I_2 \hat{X}_3 = \hat{H}_{\text{loc}} \tag{1.84}$$

Adding local operators does not increase the maximum bond dimension:

$$\hat{H}_{\text{loc}} = \sum_i \hat{X}_i + \sum_i \hat{Y}_i, \tag{1.85}$$

$$W^{[1]} = \begin{pmatrix} I & (\hat{X} + \hat{Y}) \end{pmatrix}, W^{[i]} = \begin{pmatrix} I & (\hat{X} + \hat{Y}) \\ 0 & I \end{pmatrix}, W^{[N]} = \begin{pmatrix} (\hat{X} + \hat{Y}) \\ I \end{pmatrix}, \tag{1.86}$$

Example 3 *Interaction Hamiltonian*

The bond dimension of an MPO increases when interactions are present. For example, the MPO for a nearest-neighbor interaction has a maximum bond dimension $\chi = 3$:

$$H_{\text{nearest-neighbour}} = \sum_{i=1}^{N-1} \hat{X}_i \otimes \hat{Y}_{i+1}, \qquad W^{[i]} = \begin{pmatrix} I & \hat{X} & 0 \\ 0 & 0 & \hat{Y} \\ 0 & 0 & 1 \end{pmatrix}, \chi = 3 \tag{1.87}$$

Adding more interaction terms increases the bond dimension of the MPO. Without any symmetry, the total bond dimension is $\chi = 2 + N_{\text{terms}}$, where N_{terms} is the number of interaction terms in the Hamiltonian:

$$H_{N_{\text{terms}}=3} = \sum_{i=1}^{N-1} (\hat{X}_i \otimes \hat{X}_{i+1} + \hat{Y}_i \otimes \hat{Y}_{i+1} + \hat{Z}_i \otimes \hat{Z}_{i+1}), \tag{1.88}$$

$$W^{[i]} = \begin{pmatrix} I & \hat{X} & \hat{Y} & \hat{Z} & 0 \\ 0 & 0 & 0 & 0 & \hat{X} \\ 0 & 0 & 0 & 0 & \hat{Y} \\ 0 & 0 & 0 & 0 & \hat{Z} \\ 0 & 0 & 0 & 0 & I \end{pmatrix}, \chi = 5 \tag{1.89}$$

Example 4 *General long-range Hamiltonian*

MPO construction is always possible for a general Hamiltonian with long-range interactions by employing the concept of a finite state machine [15]. Consider a

rule	**input**	**output**
1	$(1,1)$	$\to I$
2	$(1,2)$	$\to \hat{X}$
3	$(1,D)$	$\to \hat{Z}$
4	$(m,m+1)$	$\to I$
5	$(D-1,D)$	$\to \hat{Y}$
6	(D,D)	$\to I$

Table 1.2: $D = \min(i+2, N-i-3)$ is the bond dimension of $W^{[i]}$, and $m = 2,\dots,D-2$ carries interactions longer than nearest-neighbor.

Hamiltonian with long-range interactions and local terms, $H = \sum_{i=1}^{N} \hat{Z}_i + \sum_{i<j} c_{ij} \hat{X} \otimes \hat{Y}$. Since the bond dimension increases with the interaction range and the number of terms, for general two-body interaction Hamiltonians, the MPO bond dimension grows linearly with the system size, $\mathcal{O}(N)$.

The rules for $W^{[i]}$ that generate this Hamiltonian are summarized in table 1.2. The rule table can be converted into a matrix representation by assigning the **input** element to the **output**. For instance, rule 1 assigns an identity to the element $(1,1)$ of the matrix $W^{[i]}$, and so on.

As an example, when the interaction extends up to the next-nearest neighbor, the MPO has a bond dimension $\chi = 4$:

$$H = \sum_{i=1}^{N} \hat{Z}_i + \sum_{i=1}^{N-1} \hat{X}_i \otimes \hat{Y}_{i+1} + \sum_{i=1}^{N-2} \hat{X}_i \otimes \hat{Y}_{i+2}, W^{[i]} = \begin{pmatrix} I & \hat{X} & 0 & \hat{Z} \\ 0 & 0 & I & \hat{Y} \\ 0 & 0 & 0 & \hat{Y} \\ 0 & 0 & 0 & I \end{pmatrix}, \quad \chi = 4 \tag{1.90}$$

Finally, the general form for the MPO of a Hamiltonian with many long-range interaction terms is given by

$$W^{[i]}_{\text{gen}} = \begin{pmatrix} I & \hat{C} & \hat{D} \\ 0 & \hat{A} & \hat{B} \\ 0 & 0 & I \end{pmatrix}_{(i)} . \tag{1.91}$$

Here, $\hat{A}_i$, $\hat{B}_i$, $\hat{C}_i$, and $\hat{D}_i$ are operator-valued matrices defined by the structure of the Hamiltonian $\hat{H}$. Specifically, $\hat{D}_i$ contains operators from local terms acting only on site j, while $\hat{A}_i$, $\hat{B}_i$, and $\hat{C}_i$ contain operators from interaction terms corresponding to site i and others. Identity operators corresponding to long-range interactions are also included in $\hat{A}_i$.

1.7.1 Applying MPO to MPS

The direct application of an MPO to an MPS is achieved by contracting the MPS physical index s_k with the conjugated index s'_k of the MPO. The resulting bonds are combined, yielding an MPS with enlarged bond dimensions. If the MPO represents a unitary time propagator, this process implements time evolution, as discussed in the following section. The increase in bond dimension when applying an MPO provides an intuitive explanation for how the system generates entanglement entropy during time evolution and why long-range interactions are more challenging to simulate.

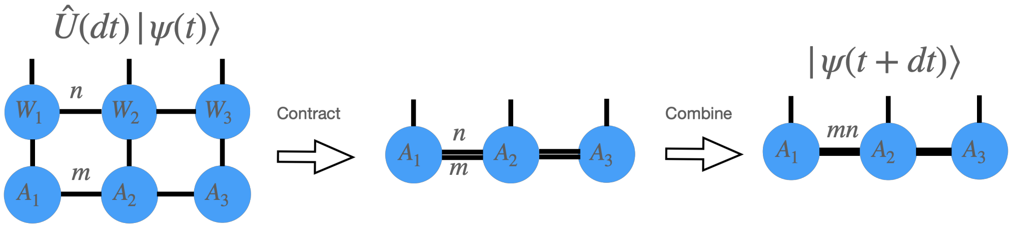

Figure 1.12: Direct application of MPO to MPS.

1.7.2 Expectation value

Given an MPS for a quantum state and an MPO for an operator, one can extract useful information from the MPS, such as the expectation value of a physical observable. This is achieved by applying the MPO of the observable to the MPS and contracting all indices of the MPS with its complex conjugate. The procedure for finding the expectation value of a local observable is depicted in fig. 1.13.

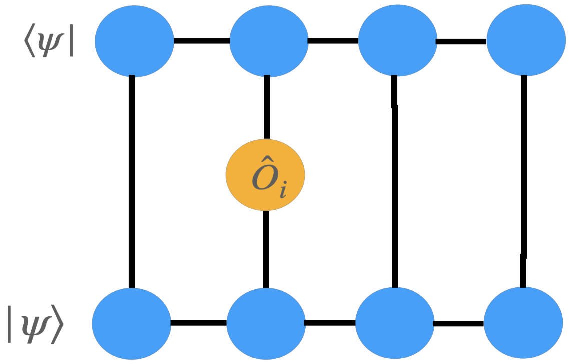

Figure 1.13: Finding the expectation value of a local observable $\hat{O}$ at site i.

1.8 Time-Evolution Algorithms

The time-evolution algorithms that support long-range interactions is required to simulate the dynamics of an NV center ensemble. In this section, we discuss two algorithms for MPS and MPDO that fulfill this requirement. The first algorithm is the MPO W^{II} method, which relies on a generalization of the operator exponential $e^{-i\hat{H}\delta t}$ approximation. The second algorithm is the Time-Dependent Variational Principle (TDVP), which evolves the MPS on a projected manifold of specific bond dimensions.

1.8.1 MPO W^{II} Method

The key concept of the W^{II} method (and its predecessor, the W^{I} method) is the use of the Euler approximation for the time propagator $\hat{U}$. For a Hamiltonian of L spin sites that can be expressed as a sum of local terms $\hat{H}_j$ acting only on individual sites, $\hat{H} = \sum_{j=1}^{L} \hat{H}_j$, the first-order Euler approximation reads:

$$e^{i\delta\hat{H}} = 1 - i\delta \sum_{j=1}^{L} \hat{H}_j + \mathcal{O}(\delta^2). \tag{1.92}$$

where $\delta \ll 1$. This first-order approximation introduces an error of approximately $L\delta^2$ per site due to $\mathcal{O}(L^2)$ contributions from higher-order terms. To mitigate inaccuracy caused by these errors as the system size increases, some second-order terms can be included in the approximation:

$$\begin{aligned} e^{i\delta\hat{H}} &= 1 - i\delta \sum_{j=1}^{L} \hat{H}_j - \delta^2 \sum_{j<k} \hat{H}_j \hat{H}_k + \mathcal{O}(L\delta^2) + \mathcal{O}(\delta^3) && (1.93) \\ &\approx \prod_j (1 - i\delta \hat{H}_j) && (1.94) \\ &\equiv U^I(\delta). && (1.95) \end{aligned}$$

The summation of second-order terms in eq. (1.93) includes only non-overlapping terms, where $\hat{H}_j$ and $\hat{H}_k$ do not act on common sites. By incorporating these additional terms, the total error is significantly reduced to $\mathcal{O}(L\delta^2)$, as only $\mathcal{O}(L)$ terms are neglected. Consequently, the error per site becomes independent of L, remaining constant with respect to system size.

Finding the MPO representation of $\hat{U}^I$ is straightforward. By rewriting the Hamiltonian focusing on a site j and separating the left, right, and j-related parts, for N_j interaction terms passing through bond j, we have:

$$\hat{H} = \hat{H}^L_{j-1} \otimes \hat{I}^R_j + \hat{I}^L_j \otimes \hat{H}^R_{j+1} + \sum_{a_j=1}^{N_j} \hat{h}^L_{j;a_j} \otimes \hat{h}^R_{j;a_j}. \tag{1.96}$$

Thus,

$$\begin{pmatrix} \hat{H}^R_{j-1} \\ \hat{h}^R_{j-1} \\ \hat{1}^R_{j-1} \end{pmatrix}, = \hat{W}_j \begin{pmatrix} \hat{H}^R_j \\ \hat{h}^R_j \\ \hat{1}^R_j \end{pmatrix} \tag{1.97}$$

$$\hat{W}_j = \begin{pmatrix} \hat{1}_j & \hat{C}_j & \hat{D}_j \\ \hat{0} & \hat{A}_j & \hat{B}_j \\ \hat{0} & \hat{0} & \hat{1}_j \end{pmatrix}. \tag{1.98}$$

By definition, the MPO for $\hat{H}$, represented by the set $(\hat{W}_1, \cdots, \hat{W}_L)$ in eq. (1.98), also provides the MPO representation for $\hat{U}^I(\delta)$. At site j, the MPO for the time propagator in eq. (1.93), denoted as $\hat{W}^I_j$, is given by:

$$\hat{W}^I_j = \begin{pmatrix} (\hat{1} + \delta \hat{D}_j) & \sqrt{\delta}\hat{C}_j \\ \sqrt{\delta}\hat{B}_j & \hat{A}_j \end{pmatrix}. \tag{1.99}$$

If $\hat{H}$ has a bond dimension χ, then $\hat{W}^I_j$ has a bond dimension of $\chi - 1$. Although constructing $\hat{W}^I$ is straightforward, further improvements can still be achieved in the approximation. For instance, for a purely on-site Hamiltonian $\hat{H} = \sum_j \hat{S}^z_j$, $U^I(\delta) = \prod_j (1 - i\delta \hat{S}^z_j)$ retains only first-order terms.

The W^{II} method was proposed to achieve higher accuracy by including terms with overlaps up to one site. The propagator is then expressed as:

$$U^{II}(\delta) = 1 - i\delta \sum_{j=1}^{L} \hat{H}_j - \delta^2 \sum_{j,k}^{\text{1-site overlap}} \hat{H}_j \hat{H}_k + \mathcal{O}(L\delta^2) + \mathcal{O}(\delta^3). \tag{1.100}$$

While eq. (1.100) has errors of the same order as eq. (1.93), all on-site terms are exact. The number of retained interaction terms is significantly larger than in eq. (1.93). Although no exact representation exists, the U^{II} MPO can be numerically constructed with $\mathcal{O}(\delta^3)$ errors, dominated by second-order approximation errors in U^{II}.

The MPO representation of U^{II} is given by:

$$\hat{W}^{II}_j = \begin{pmatrix} \widehat{W^{II}_{D_j}} & \widehat{W^{II}_{C_j}} \\ \widehat{W^{II}_{B_j}} & \widehat{W^{II}_{A_j}} \end{pmatrix}. \tag{1.101}$$

The matrices $\hat{W}^{II}_{A,B,C,D}$ can be obtained from the Taylor expansion of the generator function:

$$e^{\phi\cdot\hat{A}\cdot\bar{\phi}+\phi\cdot\hat{B}\sqrt{t}+\sqrt{t}\hat{C}\cdot\bar{\phi}+t\hat{D}} = \hat{W}^{II}_{D} + \hat{W}^{II}_{C}\cdot\bar{\phi} + \phi\cdot\hat{W}^{II}_{B} + \phi\cdot\hat{W}^{II}_{A}\cdot\bar{\phi} + ... \tag{1.102}$$

where $\phi, \bar{\phi}$ are auxiliary fields introduced for complex integration.

An additional technique to reduce numerical errors in the W^{II} method is the use of complex time steps when applying the time propagator. For example, when evolving:

$$\begin{aligned} |\psi(t+\delta t)\rangle &= \hat{U}(\delta)|\psi(t)\rangle & (1.103)\\ &= \hat{U}(\delta_1)\hat{U}(\delta_2)|\psi(t)\rangle, & (1.104) \end{aligned}$$

where $\delta_1 = \frac{1-i}{2}\delta$ and $\delta_2 = \frac{1+i}{2}\delta$. Applying the same propagator twice with complex time steps transforms the errors in the propagator from second-order to third-order. Since the computational cost of implementing complex time steps is small compared to the reduction in errors, this technique is preferable for improving accuracy. However, the general construction of this technique does not guarantee the unitarity of the time propagator and should be carefully applied in extreme parameter regimes.

1.8.2 Time-Dependent Variational Principle

Another tensor network algorithm for time evolution that supports Hamiltonians with long-range interactions is the Time-Dependent Variational Principle (TDVP). Unlike the W^{II} method, which directly approximates the propagator in MPO form, TDVP evolves the system by locally solving the time-dependent Schrödinger equation (TDSE) for pairs of tensor sites. The key idea is to restrict the time evolution to a subspace defined by the initially specified bond dimension of the MPS. The Hamiltonian is projected onto a space tangent to the MPS manifold, and the TDSE is then solved within this space.

For implementation details, let $T_{|\psi\rangle}$ denote the tangent space of the MPS representing the quantum state $|\psi\rangle$. Consider the TDSE for $|\psi\rangle$ and the Hamiltonian $\hat{H}$, projected onto $T_{|\psi\rangle}$ by the projector $\hat{P}_{T_{|\psi\rangle}}$:

$$\frac{\partial}{\partial t}|\psi\rangle = -i(\hat{P}_{T_{|\psi\rangle}}\hat{H})|\psi\rangle, \tag{1.105}$$

where

$$\hat{P}_{T_{|\psi\rangle}} = \sum_{j=1}^{L} \hat{P}^{L,|\psi\rangle}_{j-1} \otimes \hat{1}_j \otimes \hat{P}^{R,|\psi\rangle}_{j+1} - \sum_{j=1}^{L-1} \hat{P}^{L,|\psi\rangle}_{j} \otimes \hat{P}^{R,|\psi\rangle}_{j+1}. \tag{1.106}$$

Here, $\hat{P}^{L(R),|\psi\rangle}_j$ are projectors that act on site j and all other sites to the left (right). These projectors are defined as:

$$\hat{P}^{L,|\psi\rangle}_{j;\bar{\sigma}_1,\cdots,\bar{\sigma}_j,\sigma_1,\cdots,\sigma_j} = \sum_{m_j} \bar{\psi}^{L;\bar{\sigma}_1,\cdots,\bar{\sigma}_j}_{j;m_j} \otimes \psi^{L;\sigma_1,\cdots,\sigma_j}_{j;m_j} \tag{1.107}$$

$$\hat{P}^{R,|\psi\rangle}_{j;\bar{\sigma}_j,\cdots,\bar{\sigma}_L,\sigma_j,\cdots,\sigma_L} = \sum_{m_{j-1}} \bar{\psi}^{R;\bar{\sigma}_j,\cdots,\bar{\sigma}_L}_{j;m_{j-1}} \otimes \psi^{R;\sigma_j,\cdots,\sigma_L}_{j;m_{j-1}}, \tag{1.108}$$

where $\psi^{L(R)}_j$ represents the tensor at site j, in left- (right-) normalization, along with its left (right) neighboring tensors in the MPS.

Solving eq. (1.105) exactly is generally infeasible; however, an approximate solution can be obtained by locally solving each term. First, the L forward-evolving equations are solved, each of the form:

$$\frac{\partial}{\partial t}|\psi\rangle = -i(\hat{P}^{L,|\psi\rangle}_{j-1} \otimes \hat{1}_j \otimes \hat{P}^{R,|\psi\rangle}_{j+1})\hat{H}|\psi\rangle, \tag{1.109}$$

followed by solving the $L-1$ backward-evolving equations:

$$\frac{\partial}{\partial t}|\psi\rangle = i(\hat{P}^{L,|\psi\rangle}_{j} \otimes \hat{P}^{R,|\psi\rangle}_{j+1})\hat{H}|\psi\rangle. \tag{1.110}$$

Each forward (backward) equation is then multiplied by the single-site map $\bar{\psi}^L_{j-1} \otimes \bar{\psi}^R_{j+1}$ (the center-bond map $\bar{\psi}^L_j \otimes \bar{\psi}^R_{j+1}$). Thus, the Schrödinger equation is solved locally for each tensor in the MPS, starting from right to left in a single sweep.

The one-site TDVP maintains a fixed bond dimension for the MPS throughout the evolution, preventing it from increasing. However, this approach introduces significant errors due to the projection of the quantum state, particularly in the presence of interactions between sites. These projection errors can be mitigated using the two-site version of TDVP, which combines neighboring sites j and $j+1$ into a single site $(j, j+1)$ and solves the TDSE in a manner similar to the one-site version. The two-site TDVP allows the bond dimension to increase, thereby reducing projection errors compared to the one-site variant. However, it requires the SVD, which introduces another source of error. This error arises from the truncation of singular values when splitting the combined sites using SVD.

In simulations, the errors introduced by TDVP are influenced by the choice of timestep size. For a fixed final time, using a smaller timestep δ reduces finite timestep errors but increases errors from projection and truncation due to the larger number of evolution steps. Therefore, it is crucial to carefully select a timestep size that balances these competing sources of error, avoiding values that are either too large or too small.

1.9 Open System

While the MPS is a highly efficient tool for simulating the many-body dynamics of quantum systems, it is limited to the simulation of pure states. Capturing the temporal dynamics of a mixed state requires the use of a density operator. If the Hilbert space of an N-body pure state $|\psi\rangle$ is $\mathcal{H}_{|\psi\rangle} \in \mathcal{C}^N$, the density operator ρ resides in a larger Hilbert space $\mathcal{H}_\rho \in \mathcal{C}^{N\times N}$. Consequently, MPS alone is insufficient in this case. Furthermore, incorporating dissipation arising from interactions between the system and its environment (bath) is not feasible with MPS.

To overcome these limitations, a tensor network structure similar to MPS, called the Matrix Product Density Operator (MPDO), is employed. The key idea is to represent the vectorized density operator in an MPS-like form, but with squared bond dimensions. Since the one-dimensional structure is preserved, most MPS algorithms discussed in the previous section can be adapted for MPDO with minor modifications. This allows for the simulation of dissipative dynamics by solving the vectorized master equation using methods such as the W^{II} method (section 1.8.1) or the TDVP algorithm (section 1.8.2). In this section, we will discuss the vectorization of operators, the concept of super-operators, the construction of MPDOs from MPS, and the vectorized form of Lindblad's master equation.

1.9.1 Vectorization

Vectorization is a tensor reshaping operation that transforms a tensor into a vector. For instance, a rank-3 tensor T_{ijk} can be vectorized into $\vec{T}_a$, where $a \equiv (i, j, k)$ represents a combination of the indices i, j, and k. The result is a flat, rank-1 tensor (a vector), which is why this operation is sometimes referred to as "flattening." There are two common ways to vectorize a tensor, depending on the order in which the elements are arranged: (i) Row-major order and (ii) Column-major order.

To illustrate this, consider a density operator of a two-level system (a qubit), represented by the 2 × 2 matrix:

$$\hat{\rho} = \begin{bmatrix} \rho_{00} & \rho_{01} \\ \rho_{10} & \rho_{11} \end{bmatrix} \tag{1.111}$$

Row-major order: This format is the default in programming languages such as C, C++, and the Python library *NumPy*. In this approach, the tensor is flattened by appending rows sequentially. Applying row-major vectorization to the matrix in eq. (1.111) yields:

$$\hat{\rho} = \begin{bmatrix} \rho_{00} & \rho_{01} \\ \rho_{10} & \rho_{11} \end{bmatrix}_{(m \times n)} \xrightarrow{Row-major} vec(\rho) = \begin{bmatrix} \rho_{00} \\ \rho_{01} \\ \rho_{10} \\ \rho_{11} \end{bmatrix}_{1 \times (mn)} \tag{1.112}$$

Column-major order: This format is the default in Fortran and MATLAB. Here, the tensor is flattened by concatenating its columns. Applying column-major vectorization to the matrix in eq. (1.111) results in:

$$\hat{\rho} = \begin{bmatrix} \rho_{00} & \rho_{01} \\ \rho_{10} & \rho_{11} \end{bmatrix}_{(m \times n)} \xrightarrow{Column-major} vec(\rho) = \begin{bmatrix} \rho_{00} \\ \rho_{10} \\ \rho_{01} \\ \rho_{11} \end{bmatrix}_{(mn) \times 1} \tag{1.113}$$

1.9.2 Master equation

The choice of tensor flattening order not only determines the vectorized form of the density operator but also defines the vectorized master equation. To clarify this, the identity for vectorization of matrix multiplication is provided for both row-major and column-major orders:

$$vec(\hat{A}\hat{B}\hat{C}) = \begin{cases} (\hat{A} \otimes \hat{C}^T) vec(B), & \text{for row-major} \\ (\hat{C}^T \otimes \hat{A}) vec(B), & \text{for column-major} \end{cases} \tag{1.114}$$

The master equation for the time evolution of the density operator is defined as:

$$\frac{\partial}{\partial t}\hat{\rho}(t) = \mathcal{L}(t)\hat{\rho}(t) \tag{1.115}$$

$$= -\frac{i}{\hbar}[\hat{H}, \hat{\rho}(t)] + \gamma \mathcal{D}[\hat{c}]\hat{\rho}(t) \tag{1.116}$$

where the unitary and dissipative parts are given by:

$$[\hat{H}, \hat{\rho}(t)] = \hat{H}\hat{\rho}(t) - \hat{\rho}(t)\hat{H} \tag{1.117}$$

$$\mathcal{D}[\hat{c}]\hat{\rho}(t) = \hat{c}\hat{\rho}(t)\hat{c}^\dagger - \frac{1}{2}(\hat{c}^\dagger\hat{c}\hat{\rho}(t) + \hat{\rho}(t)\hat{c}^\dagger\hat{c}) \tag{1.118}$$

Using the row-major vectorization identity from eq. (1.114), the commutator term $[\hat{H}, \hat{\rho}(t)]$ is transformed as:

$$\hat{H}\hat{\rho}(t) - \hat{\rho}(t)\hat{H} \xrightarrow{vectorize} (\hat{H} \otimes \hat{\mathbb{1}} + \hat{\mathbb{1}} \otimes \hat{H}^T)vec(\rho). \tag{1.119}$$

Similarly, the dissipative term $\mathcal{D}[\hat{c}]\hat{\rho}(t)$ is vectorized as:

$$\hat{c}\hat{\rho}(t)\hat{c}^\dagger - \frac{1}{2}\left(\hat{c}^\dagger\hat{c}\hat{\rho}(t) + \hat{\rho}(t)\hat{c}^\dagger\hat{c}\right) \xrightarrow{vectorize} \left(\hat{c} \otimes \hat{c}^* - \frac{1}{2}\left(\hat{c}^\dagger\hat{c} \otimes \hat{\mathbb{1}} + \hat{\mathbb{1}} \otimes \hat{c}^T\hat{c}^*\right)\right) vec(\rho). \tag{1.120}$$

Combining these results, the vectorized master equation is expressed as:

$$\frac{\partial}{\partial t}|\rho(t)\rangle\rangle = \mathcal{L}(t)|\rho(t)\rangle\rangle \tag{1.121}$$

$$= \left(-\frac{i}{\hbar}(\hat{H} \otimes \hat{\mathbb{1}} - \hat{\mathbb{1}} \otimes \hat{H}^T) + \gamma(\hat{c} \otimes \hat{c}^* - \frac{1}{2}(\hat{c}^\dagger\hat{c} \otimes \hat{\mathbb{1}} + \hat{\mathbb{1}} \otimes \hat{c}^T\hat{c}^*))\right)|\rho(t)\rangle\rangle. \tag{1.122}$$

Here, $|\rho(t)\rangle\rangle = vec(\hat{\rho}(t))$ represents the vectorized form (or super-ket) of the density operator. The solution for the time evolution from t to $t + dt$ is given by:

$$|\rho(t + dt)\rangle\rangle = e^{\mathcal{L}dt}|\rho(t)\rangle\rangle. \tag{1.123}$$

1.9.3 MPDO

The Matrix Product Density Operator (MPDO) provides a compact representation of a density operator in a tensor network form, similar to the Matrix Product State (MPS). To construct an MPDO, the most straightforward approach is to perform an outer product between an MPS and its complex conjugate. This can be achieved by introducing auxiliary indices to the MPS tensors and contracting them appropriately.

Let $A^{[k]}_{\alpha_k,i,\alpha_k}$ represent the tensor at site k of the MPS corresponding to $|\psi\rangle$, and let $A^{*[k]}_{\alpha'_k,i',\alpha'_k}$ represent the tensor at site k of the conjugate MPS $\langle\psi|$. The indices (α_k, i, α_k) have dimensions (χ, d, χ), corresponding to the left bond, physical index, and right bond, respectively. To construct the MPDO, auxiliary indices β and β'

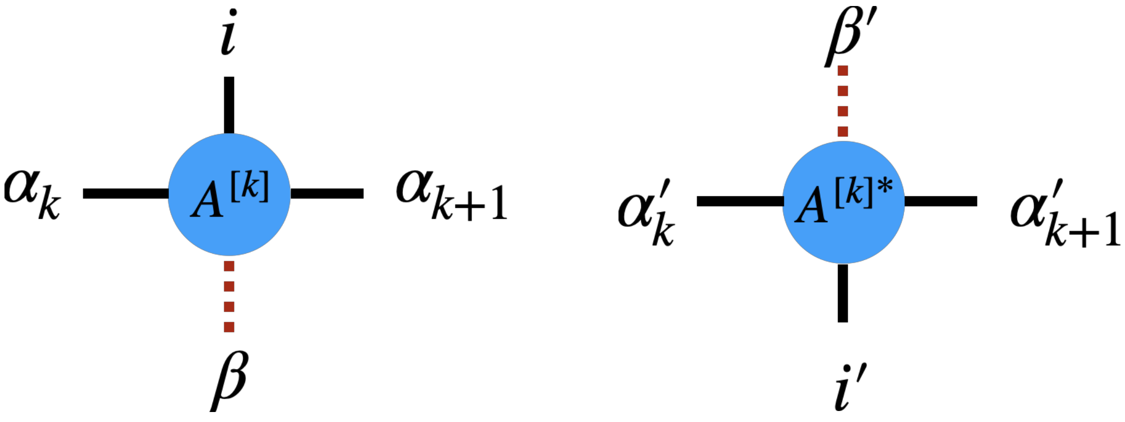

(a) A^k **(b)** $A^{*[k]}$

Figure 1.14: Tensor diagrams for the MPS of $|\psi\rangle$ and $\langle\psi|$. The dashed leg represents the auxiliary index with dimension 1.

with dimension 1 are added to $A^{[k]}$ and $A^{*[k]}$, respectively. These auxiliary indices do not alter the size of the tensors and can be added trivially:

$$A^{[k]}_{\alpha_k,i,\alpha_k} \to A^{[k]}_{\alpha_k,i,\beta,\alpha_k} \tag{1.124}$$

$$A^{*[k]}_{\alpha'_k,i',\alpha'_k} \to A^{*[k]}_{\alpha'_k,i',\beta',\alpha'_k} \tag{1.125}$$

The MPDO $|\rho\rangle\rangle = \mathrm{vec}(|\psi\rangle\langle\psi|)$ is then constructed by contracting the auxiliary indices β and β'. After the contraction, the remaining indices are fused together to create an MPS-like structure:

$$\sum_{\beta=\beta'} A^{[k]}_{\alpha_k,i,\beta,\alpha_k} A^{*[k]}_{\alpha'_k,i',\beta',\alpha'_k} = B^{[k]}_{\alpha_k,i,\beta,\alpha_k,\alpha'_k,i',\beta',\alpha'_k} \tag{1.126}$$

$$= B^{[k]}_{(\alpha_k,\alpha'_k),(i,i'),(\beta,\alpha'_k)} \tag{1.127}$$

$$= B^{[k]}_{\alpha''_k,i'',\alpha''_k} \tag{1.128}$$

Here, the combined indices $(\alpha''_k, i'', \alpha''_k)$ have dimensions (χ^2, d^2, χ^2), which are the squared dimensions of the original MPS. This results in an MPDO with squared bond and physical dimensions compared to the original MPS.

The process of constructing an MPDO is illustrated in fig. 1.14 and fig. 1.15. In fig. 1.14, the auxiliary indices are added to the MPS tensors, while in fig. 1.15, the contraction of the auxiliary indices and the resulting MPDO structure are shown.

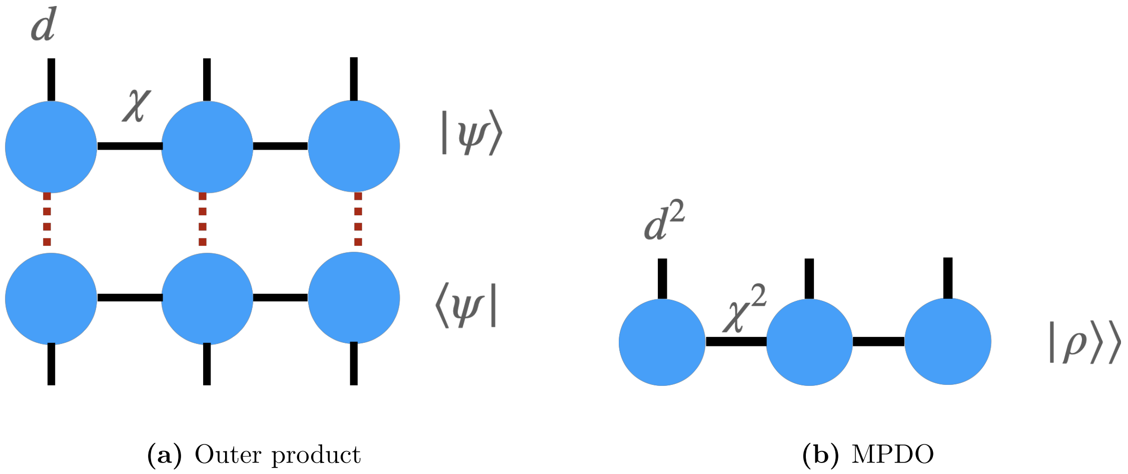

(a) Outer product **(b)** MPDO

Figure 1.15: The contraction of the auxiliary indices results in an MPDO with squared bond and physical dimensions.

1.9.4 MPO of super-operator

In Liouville space (the space of the vectorized density operator), the number of operators in the Hamiltonian acting on $|\rho\rangle\rangle$ effectively doubles. This arises because the super-operators $\hat{H} \otimes \hat{\mathbb{1}}$ and $\hat{\mathbb{1}} \otimes \hat{H}$ in eq. (1.119) are treated as distinct terms when constructing a Matrix Product Operator (MPO). However, this increase in the number of local terms does not affect the bond dimension. As a result, the MPO of the super-operator is enlarged only by twice the number of interaction terms.

As discussed in example 3, the bond dimension of an MPO is given by $\chi_{\text{op}} = 2 + N_{\text{terms}}$, where N_{terms} is the number of interaction terms in the Hamiltonian. For the super-operator, the bond dimension becomes $\chi_{\text{sup-op}} = 2 + 2N_{\text{terms}}$.

For example, consider the Hamiltonian of the transverse field Ising model:

$$\hat{H}_{\text{ising}} = -J \sum_{i=1}^{N-1} \hat{S}_z^i \hat{S}_z^{i+1} - g \sum_{i=1}^{N} \hat{S}_x^i. \tag{1.129}$$

The MPO for this Hamiltonian is represented as:

$$W_{H,\text{ising}}^{[i]} = \begin{pmatrix} \hat{I} & \hat{S}_z & -g\hat{S}_x \\ 0 & 0 & -J\hat{S}_z \\ 0 & 0 & \hat{I} \end{pmatrix}. \tag{1.130}$$

From the master equation in eq. (1.122), the Liouvillian super-operator $\mathcal{L}(t)$ is expressed as:

$$\mathcal{L}(t) = \left(\underbrace{-\frac{i}{\hbar}(\hat{H} \otimes \hat{\mathbb{1}} - \hat{\mathbb{1}} \otimes \hat{H}^T)}_{\mathcal{M}_H} + \underbrace{(\hat{c} \otimes \hat{c}^* - \frac{1}{2}(\hat{c}^\dagger \hat{c} \otimes \hat{\mathbb{1}} + \hat{\mathbb{1}} \otimes \hat{c}^T \hat{c}^*))}_{\mathcal{M}_L} \right). \tag{1.131}$$

The MPO for the Liouvillian $\mathcal{L}(t)$ is then constructed as:

$$W^{[i]}_{\mathcal{M}_H} = \begin{pmatrix} \hat{I} & \hat{S}_z \otimes \hat{I} & \hat{I} \otimes \hat{S}_z^T & -g\hat{S}_x \otimes \hat{I} + \hat{I} \otimes g\hat{S}_x^T \\ 0 & 0 & 0 & -J(\hat{S}_z \otimes \hat{I}) \\ 0 & 0 & 0 & J(\hat{I} \otimes \hat{S}_z^T) \\ 0 & 0 & 0 & \hat{I} \end{pmatrix}, \tag{1.132}$$

and the MPO for the Lindblad term $\mathcal{M}_L$ is:

$$W^{[i]}_{\mathcal{M}_L} = i\gamma \begin{pmatrix} 0 & 0 & 0 & \hat{c} \otimes \hat{c}^* - \frac{1}{2}\left(\hat{c}^\dagger \hat{c} \otimes \hat{I} + \hat{I} \otimes \hat{c}^* \hat{c}^T\right) \\ 0 & 0 & 0 & 0 \\ 0 & 0 & 0 & 0 \\ 0 & 0 & 0 & 0 \end{pmatrix}. \tag{1.133}$$

Although the MPDO retains the MPS-like structure and evolves using MPS algorithms, the method for calculating expectation values in MPS is not directly applicable to MPDO. To extract an expectation value from an MPDO, two mathematically equivalent approaches can be used.

The first approach is based on the definition of the expectation value for a density operator:

$$\langle \hat{O} \rangle = \mathrm{Tr}[\hat{O}\hat{\rho}]. \tag{1.134}$$

In this method, the trace is implemented by splitting the combined physical index of the MPDO and contracting them together. The contraction scheme for this approach is illustrated in fig. 1.16.

The second approach leverages the vectorization of operators. In this scheme, the expectation value is calculated as the inner product of the vectorized observable and the MPDO:

$$\langle \hat{O} \rangle_{\mathrm{vec}} = \langle \hat{O} | \hat{\rho} \rangle. \tag{1.135}$$

Here, the observable is represented as a vectorized tensor, which is then contracted with the MPDO. The contraction scheme for this approach is depicted in fig. 1.17.

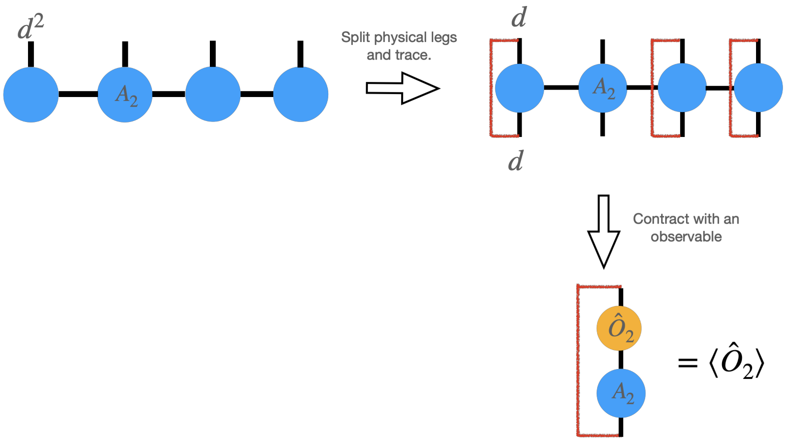

Figure 1.16: Contraction scheme for calculating the expectation value of a local observable using the definition in eq. (1.134).

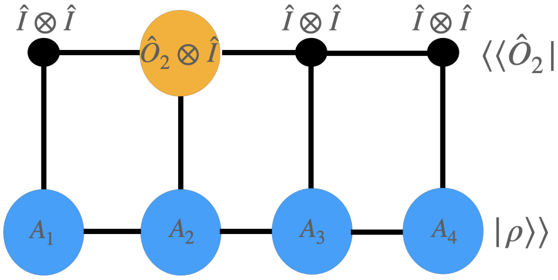

Figure 1.17: Calculation of the expectation value using the vectorized definition in eq. (1.135).

1.10 Entanglement Entropy

1.10.1 MPS

In MPS, the bond dimension, which corresponds to the dimension of the bond index connecting the left and right subsystems, is directly related to the entanglement entropy of the bipartite system. To illustrate the physical significance of the bond dimension, consider the *Schmidt decomposition* of a pure state $|\psi\rangle$ across a specific bond:

$$|\psi\rangle_{AB} = \sum_{ij} \sqrt{p_{ij}} |i\rangle_A \otimes |j\rangle_B. \tag{1.136}$$

Here, $|i\rangle_A$ and $|j\rangle_B$ are orthonormal basis states of the left and right subsystems, respectively. The matrix of Schmidt coefficients $\sqrt{p_{ij}}$ can be expressed using singular value decomposition:

$$p_{ij} = UDV^\dagger \tag{1.137}$$

$$\sqrt{p}_{ij} = UD^{1/2}V^\dagger \tag{1.138}$$

$$= \sum_{\alpha=1}^{\chi} \sqrt{\lambda_\alpha} U_{i\alpha} V^\dagger_{j\alpha}. \tag{1.139}$$

Here, $\sqrt{\lambda_\alpha} > 0$ are the Schmidt coefficients, and $\sum_{\alpha=1}^{\chi} \lambda_\alpha = 1$. In the MPS canonical form, the unitary matrices U and $V^\dagger$ are absorbed into the basis states $|i\rangle_A$ and $|j\rangle_B$, forming a new basis:

$$|\alpha\rangle_A = \sum_i U_{i\alpha} |i\rangle_A \tag{1.140}$$

$$|\alpha\rangle_B = \sum_j V^\dagger_{j\alpha} |j\rangle_B, \tag{1.141}$$

The pure state can then be written as:

$$|\psi\rangle = \sum_{\alpha=1}^{\chi} \sqrt{\lambda_\alpha} |\alpha\rangle_A \otimes |\alpha\rangle_B. \tag{1.142}$$

Thus, the bond index contains the singular values from the SVD, and the bond dimension χ equals the number of singular values.

The entanglement entropy, defined as the von Neumann entropy of the reduced density matrix, , $S = -\operatorname{Tr}[\rho_A log(\rho_A)] = -\operatorname{Tr}[\rho_B log(\rho_B)]$, can be computed directly from the singular values λ_α:

$$S = -\sum_{\alpha=1}^{\chi} \lambda_\alpha \log(\lambda_\alpha). \tag{1.143}$$

This shows that an MPS with a larger bond dimension χ can represent states with higher entanglement, thereby accessing a larger Hilbert space. The entanglement entropy also serves as a measure of the efficiency of MPS. Since the truncation error defined by eq. (1.78) is a summation of truncated singular values, for systems with low entanglement, MPS can be compressed to a smaller bond dimension with bounded truncation errors, reducing computational resources.

1.10.2 MPDO

For mixed states, entanglement measures are not well-defined. Therefore, the quantity in eq. (1.143), computed from the singular values of a Matrix Product Density Operator (MPDO), does not directly represent entanglement entropy.

However, the concept of using singular values in the bond dimension to quantify approximation errors remains valid for MPDOs. To avoid ambiguity, we define the *operator entanglement entropy* (opEE) to distinguish it from the entanglement entropy (EE) of pure states computed from MPS.

It can be shown that the opEE of an MPDO for a pure state is twice the EE of the corresponding MPS [37]. From eq. (1.142), the density operator of the total system is:

$$\rho_{AB} = |\psi_{AB}\rangle\langle\psi_{AB}| \tag{1.144}$$

$$= \sum_{i=1,j=1}^{\chi,\chi} \sqrt{\lambda_i}\sqrt{\lambda_j}(|i\rangle_A \otimes |i\rangle_B)(\langle j|_A \otimes \langle j|_B). \tag{1.145}$$

The reduced density matrices for the bipartite system are obtained by tracing out the other subsystem:

$$\rho_A = \mathrm{Tr}_B[\rho_{AB}] = \sum_{i=1}^{\chi} \lambda_i |i\rangle_A\langle i|_A, \tag{1.146}$$

$$\rho_B = \mathrm{Tr}_A[\rho_{AB}] = \sum_{j=1}^{\chi} \lambda_j |j\rangle_B\langle j|_B. \tag{1.147}$$

The standard entanglement entropy, as in eq. (1.143), is:

$$S(\rho_A) = -\,\mathrm{Tr}[\rho_A log(\rho_A)] = -\,\mathrm{Tr}[\rho_B log(\rho_B)] = S(\rho_B) \tag{1.148}$$

$$= -\sum_{i=1}^{\chi} \lambda_i log \lambda_i. \tag{1.149}$$

To compute the opEE, we vectorize eq. (1.145):

$$|\rho_{AB}\rangle = |\psi_{AB}\rangle|\psi_{AB}\rangle \tag{1.150}$$

$$= \sum_{\mu=vec(i,j)}^{r^2} \Lambda_\mu |i_A i_B; j_A j_B\rangle. \tag{1.151}$$

where $\Lambda_\mu = \sqrt{\lambda_i}\sqrt{\lambda_j}$. The super density operator $\rho^\sharp$ is defined as:

$$\rho^\sharp_{AB} = |\rho_{AB}\rangle\langle\rho_{AB}| \tag{1.152}$$

$$= \sum_{\substack{\mu=vec(i,j),\\ \nu=vec(k,l)}}^{r^2,r^2} \Lambda_\mu\Lambda_\nu |i_A i_B; j_A j_B\rangle\langle k_A k_B; l_A l_B|. \tag{1.153}$$

The reduced super density operator is:

$$\rho_A^\sharp = \sum_{\mu}^{r^2} \Lambda_\mu^2 |i_A; j_A\rangle\langle i_A; j_A|, \tag{1.154}$$

$$\rho_B^\sharp = \sum_{\nu}^{r^2} \Lambda_\nu^2 |k_A; l_A\rangle\langle k_A; l_A|. \tag{1.155}$$

The opEE can then be computed as:

$$\begin{aligned}
S_{OP}(\rho_A^\sharp) &= -\left[\sum_\mu \Lambda_\mu^2 log(\Lambda_\mu^2)\right] && (1.156)\\
&= -\left[\sum_{i,j} (\lambda_i\lambda_j) log(\lambda_i\lambda_j)\right] && (1.157)\\
&= -\left[\sum_{i,j} (\lambda_i\lambda_j)\left(log(\lambda_i) + log(\lambda_j)\right)\right] && (1.158)\\
&= -\left[\sum_i (\lambda_i) log(\lambda_i) \sum_j (\lambda_j) + \sum_i (\lambda_i) \sum_j (\lambda_j) log(\lambda_j)\right] && (1.159)\\
&= -\left[2\sum_i \lambda_i \log(\lambda_i)\right] && (1.160)\\
&= 2S(\rho_A) && (1.161)
\end{aligned}$$

since $\sum_i \lambda_i = \sum_j \lambda_j = 1$.

This relationship can also be derived from the definitions of MPS and MPDO. For an MPS:

$$|\psi\rangle = \sum_{\{i\}} \mathrm{Tr}\left[A_{i_1}^{[1]}\lambda^{[1]} \cdots A_{i_L}^{[L]}\lambda^{[L]}\right] |i_1 \cdots i_L\rangle, \tag{1.162}$$

the singular value tensors $\lambda^{[l]} = \mathrm{diag}(\lambda_1, \cdots, \lambda_\chi)$ of the bond that connects tensors $A^{[l]}$ and $A^{[l+1]}$ explicitly define the bond dimension χ. For the MPDO:

$$|\psi\rangle\langle\psi| = \sum_{\{i,j\}} \mathrm{Tr}\left[A_{i_1}^{[1]}\lambda^{[1]} \cdots A_{i_L}^{[L]}\lambda^{[L]}\right] \times \mathrm{Tr}\left[A_{j_1}^{*[1]}\lambda^{[1]} \cdots A_{j_L}^{*[L]}\lambda^{[L]}\right] |i_1 \cdots i_L\rangle\langle j_1 \cdots j_L| \tag{1.163}$$

$$= \sum_{\{i,j\}} \mathrm{Tr}\left[\left(A_{i_1}^{[1]} \otimes A_{j_1}^{*[1]}\right)\left(\lambda^{[1]} \otimes \lambda^{[1]}\right) \cdots \left(A_{i_L}^{[L]} \otimes A_{j_L}^{*[L]}\right)\left(\lambda^{[1]} \otimes \lambda^{[1]}\right)\right] \tag{1.164}$$

$$|i_1 \cdots i_L\rangle\langle j_1 \cdots j_L|.$$

$$|\rho\rangle_\sharp = \sum_{\{i,j\}} \mathrm{Tr}\left[A_{i_1}^{[1]\sharp}\lambda^{[1]\sharp} \cdots A_{i_L}^{[L]\sharp}\lambda^{[L]\sharp}\right] |i_1 \cdots i_L; j_1 \cdots j_L\rangle, \tag{1.165}$$

we find $\lambda^{[l]\sharp} = \lambda^{[l]} \otimes \lambda^{[l]}$, confirming the relationship between opEE and EE.

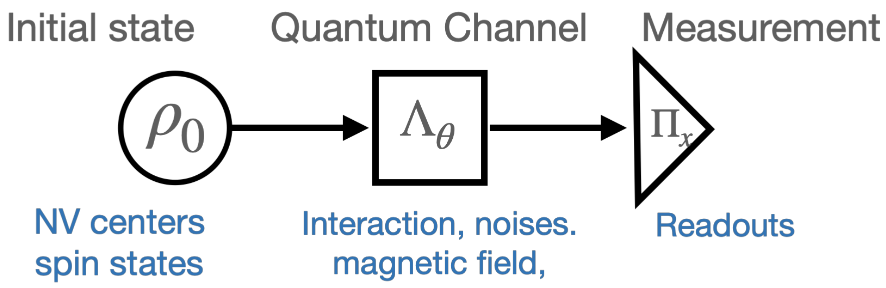

Figure 1.18: Parameter estimation with NV centers. The NV centers are prepared in the initial quantum state ρ_0. The state is then passed through a quantum channel consisting of interactions, noise, and an external magnetic field. The quantum channel encodes a parameter θ, which is estimated from the readouts, into the phase of the quantum state.

1.11 Quantum Fisher Information

In this section, we discuss the theoretical framework of quantum metrology and how to quantify the sensitivity of a probe. The Quantum Fisher Information (QFI) is introduced as a measure of the probe's sensitivity, and the method for calculating the QFI using tensor networks is presented in this section.

1.11.1 Cramér-Rao bound

We begin by discussing how using an ensemble of NV centers can enhance the sensitivity of a probe. Consider a magnetic field estimation problem with spin probes. The probe can be a single NV center or an ensemble of many NV centers (see fig. 1.18). Initially, the probes are prepared in the quantum state ρ_0. The probes are then evolved by passing through a quantum channel that includes interactions, noise, and the magnetic field. This channel encodes an unknown parameter θ into the phase of the probes. Finally, a measurement is performed on the probes. Given a conditional probability distribution $p(x|\theta)$, the unknown parameter θ is estimated from the readouts.

According to the Cramér-Rao bound, the sensitivity in estimating a parameter θ using quantum probes is bounded by the inverse of the QFI:

$$(\delta\theta)^2 \geq \frac{1}{MF_\theta} \tag{1.166}$$

where M is the number of independent experiments [34]. As per eq. (1.166), sensitivity improves by either increasing the number of experimental repetitions or enhancing the QFI. A higher QFI allows the parameter to be estimated with reduced variance. However, increasing M can be resource-intensive, as the probe's state must be reset for each repetition. If M is fixed, achieving a higher QFI becomes essential. This can be accomplished by preparing the probe in a state that maximizes the QFI. To surpass the maximum QFI achievable with a single NV center, additional NV centers must be added to the probe. Since each NV center acts as an independent probe, the QFI scales with the square root of the number of probes. For N independent probes, this results in the Standard Quantum Limit (SQL):

$$\delta\theta \geq \mathcal{O}(1/\sqrt{N}). \tag{1.167}$$

However, this is not the ultimate limit. The QFI scaling can be further improved when the probes are highly entangled. For instance, under evolution governed by a pure Zeeman term and in the absence of decoherence and dissipation, probes prepared in a GHZ state achieve optimal sensitivity for magnetic field measurements. This sensitivity follows the "Heisenberg limit" (HL), where the QFI is proportional to N [20]. Consequently:

$$\delta\theta \geq \mathcal{O}(1/N) \tag{1.168}$$

This demonstrates why entangled probes are preferred in quantum metrology.

In the context of parameter estimation, the Quantum Fisher Information (QFI) quantifies how much information about a specific parameter can be extracted from a quantum state. The formal definition of QFI for a general mixed state ρ in estimating a parameter θ is given by:

$$F_\theta = \mathrm{Tr}[L_\theta^2 \rho_\theta]. \tag{1.169}$$

Here, ρ_θ is the quantum state parameterized by θ, expressed as $\rho_\theta = e^{-i\theta\hat{A}}\rho e^{i\theta\hat{A}}$, where $\hat{A}$ is a Hermitian operator. The operator L_θ, known as the symmetric logarithmic derivative, satisfies the equation:

$$\frac{\partial\rho_\theta}{\partial\theta} = \frac{1}{2}(L_\theta\rho_\theta + \rho_\theta L_\theta). \tag{1.170}$$

Assuming the state ρ is decomposed into its eigenbasis as:

$$\rho = \sum_k \lambda_k |k\rangle\langle k|, \tag{1.171}$$

the explicit formula for QFI can be derived by rewriting eq. (1.169) as:

$$F[\rho, \hat{A}] = 2\sum_{k,l} \frac{(\lambda_k - \lambda_l)^2}{\lambda_k + \lambda_l} |\langle k|\hat{A}|l\rangle|^2. \tag{1.172}$$

Calculating QFI using eq. (1.172) requires knowledge of the full spectrum of the quantum state's eigenvalues. This can be computationally impractical for systems with a large number of spins.

However, in the special case where the quantum state is a pure state, i.e., $\rho = |\psi\rangle\langle\psi|$, eq. (1.172) simplifies significantly. In this case, the QFI can be efficiently computed as four times the variance of the observable operator $\hat{A}$:

$$\begin{aligned} F_{\text{pure}}[\rho, \hat{A}] &= 4\sum_{l\neq 0} |\langle l|\hat{A}|0\rangle|^2 && (1.173)\\ &= 4\sum_{l\neq 0}\langle 0|\hat{A}|l\rangle\langle l|\hat{A}|0\rangle && (1.174)\\ &= 4\langle 0|\hat{A}\left(\sum_{l\neq 0}|l\rangle\langle l|\right)\hat{A}|0\rangle && (1.175)\\ &= 4\langle 0|\hat{A}\,(1-|0\rangle\langle 0|)\,\hat{A}|0\rangle && (1.176)\\ &= 4\left(\langle 0|\hat{A}^2|0\rangle - (\langle 0|\hat{A}|0\rangle)^2\right) && (1.177)\\ &= 4(\delta\hat{A})^2. && (1.178) \end{aligned}$$

For mixed states, the QFI is always bounded by the maximum QFI of the eigenstate with the highest variance. This is because QFI is a convex sum of the density operators:

$$F[p\rho_1 + (1-p)\rho_2] < pF_{\text{pure}}[\rho_1] + (1-p)F_{\text{pure}}[\rho_2]. \qquad (1.179)$$

1.11.2 Single qubit

To illustrate the insights provided by the QFI in parameter estimation, let us consider the task of estimating a magnetic field using a single qubit. The objective is to identify the qubit state that is most sensitive to an external magnetic field. Initially, the qubit is prepared in a superposition state using a parameterized X-gate:

$$\begin{aligned} |\psi_\phi(0)\rangle &= e^{-iS_x\phi}|0\rangle && (1.180)\\ &= \begin{bmatrix}\cos(\phi/2)\\ \sin(\phi/2)\end{bmatrix}. && (1.181) \end{aligned}$$

Here, the angle ϕ determines the probabilities of the qubit being in the eigenstates $|0\rangle$ and $|1\rangle$. The qubit then interacts with the magnetic field for a duration T, evolving freely under the Hamiltonian $H_{\text{sense}} = BS_z$, where B is the amplitude of the magnetic field. The final quantum state accumulates a phase $\theta = BT$, which we aim to estimate in order to determine the magnetic field B:

$$|\psi_\phi(\theta)\rangle = e^{-iS_z\theta}|\psi_\phi(0)\rangle \tag{1.182}$$
$$= \begin{bmatrix} e^{i\theta/2}\cos(\phi/2) \\ e^{-i\theta/2}\sin(\phi/2) \end{bmatrix}. \tag{1.183}$$

The state that maximizes the QFI is the one most sensitive to the magnetic field. Since the state in eq. (1.183) is pure, the QFI can be calculated using eq. (1.178):

$$F[|\psi_\phi(\theta)\rangle, \hat{S}_z] = 4\left(\langle\psi_\phi(\theta)|\hat{S}_z^2|\psi_\phi(\theta)\rangle - (\langle\psi_\phi(\theta)|\hat{S}_z|\psi_\phi(\theta)\rangle)^2\right) \tag{1.184}$$
$$= 4(\frac{1}{4} - \frac{1}{4}(\cos^2(\phi/2) - \sin^2(\phi/2)^2) \tag{1.185}$$
$$= 1 - \cos^2(\phi) = \sin^2(\phi). \tag{1.186}$$

From eq. (1.186) and fig. 1.20, we observe the following for a single qubit:

1. The QFI has a value between 0 and 1, $F_{\text{pure}} \in [0, 1]$.

2. The QFI is maximized, $F_{\text{pure}} = 1$, when $\phi = \pi/2$ or $\phi = 3\pi/2$. These angles correspond to equal superposition states, which are eigenstates of $\hat{S}_x$. The qubit is most sensitive to the magnetic field when initialized in one of these states.

The corresponding states for maximum QFI are:

$$|\psi_{\pi/2}(0)\rangle = \frac{1}{\sqrt{2}}(|0\rangle + |1\rangle)) = |+\rangle \tag{1.187}$$
$$|\psi_{3\pi/2}(0)\rangle = \frac{1}{\sqrt{2}}(|0\rangle - |1\rangle)) = |-\rangle \tag{1.188}$$

1.11.3 Single NV center

Similar to the single qubit case, we can calculate the QFI for a single NV center, which is a spin-1 system. To do so, we first introduce the general formula for unitary operators acting on the triplet state [8]:

$$e^{i\phi(\hat{\boldsymbol{n}}\cdot\vec{\boldsymbol{S}})} = \hat{I} + i(\hat{\boldsymbol{n}}\cdot\vec{\boldsymbol{S}})\sin\phi + (\hat{\boldsymbol{n}}\cdot\vec{\boldsymbol{S}})^2(\cos\phi - 1) \tag{1.189}$$
$$= I + (i2\hat{\boldsymbol{n}}\cdot\vec{\boldsymbol{S}}\sin(\phi/2)\cos(\phi/2)) + \frac{1}{2}(i2\hat{\boldsymbol{n}}\cdot\vec{\boldsymbol{S}}\sin(\phi/2))^2 \tag{1.190}$$

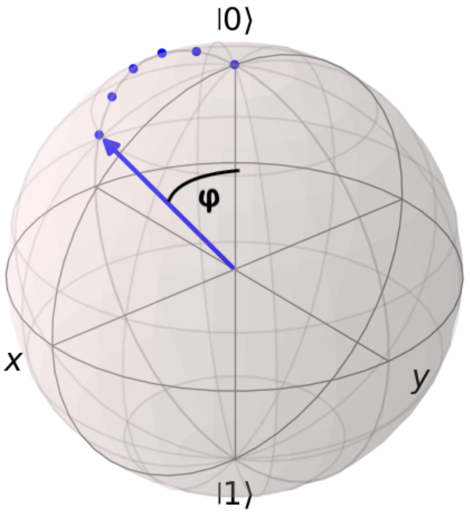

Figure 1.19: Bloch sphere representation of a parameterized qubit state in eq. (1.181). The angle ϕ determines the superposition between $|0\rangle$ and $|1\rangle$.

Let $\hat{\boldsymbol{n}} \cdot \vec{\boldsymbol{S}} = S_x$. The parameterized state is then given by:

$$
\begin{aligned}
|\psi_\phi(0)\rangle &= e^{-i\phi\hat{S}_x}|0\rangle && (1.191)\\
&= (I - i2\sin(\phi/2)\cos(\phi/2)\hat{S}_x - 2\sin^2(\phi/2)\hat{S}_x{}^2)|0\rangle && (1.192)\\
&= \begin{bmatrix} 1-\sin^2(\phi/2) & -i\sqrt{2}\sin(\phi/2)\cos(\phi/2) & -\sin^2(\phi/2) \\ -i\sqrt{2}\sin(\phi/2)\cos(\phi/2) & 1-2\sin^2(\phi/2) & -i\sqrt{2}\sin(\phi/2)\cos(\phi/2) \\ -\sin^2(\phi/2) & -i\sqrt{2}\sin(\phi/2)\cos(\phi/2) & 1-\sin^2(\phi/2) \end{bmatrix}|0\rangle && (1.193)\\
&= \begin{bmatrix} -\frac{i}{\sqrt{2}}\sin\phi \\ 1-2\sin^2(\phi/2) \\ -\frac{i}{\sqrt{2}}\sin\phi \end{bmatrix} && (1.194)\\
&= \begin{bmatrix} -\frac{i}{\sqrt{2}}\sin\phi \\ \cos\phi \\ -\frac{i}{\sqrt{2}}\sin\phi \end{bmatrix}. && (1.195)
\end{aligned}
$$

When this state interacts with a magnetic field, the evolution is governed by the unitary operator $\hat{U}(\theta) = e^{-i\theta\hat{S}_z}$, where $\hat{S}_z$ is given by:

$$\hat{S}_z = \begin{pmatrix} 1 & 0 & 0 \\ 0 & 0 & 0 \\ 0 & 0 & -1 \end{pmatrix}. \qquad (1.196)$$

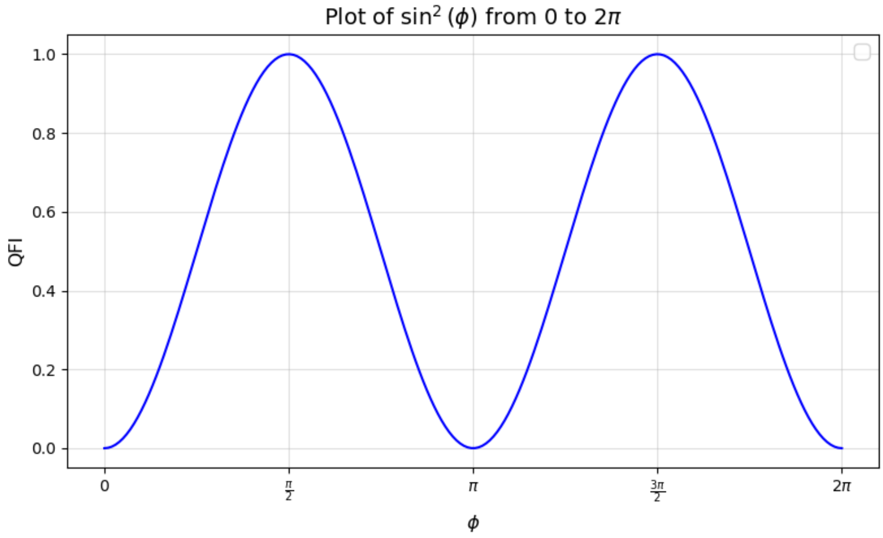

Figure 1.20: QFI of a single qubit in sensing a magnetic field. The QFI is maximized at $\phi = \pi/2$ and $\phi = 3\pi/2$.

The evolved state is:

$$|\psi_\phi(\theta)\rangle = e^{-i\theta \hat{S}_z} |\psi_\theta(0)\rangle \tag{1.197}$$

$$= \begin{bmatrix} -\frac{i}{\sqrt{2}} \sin\phi e^{-i\theta} \\ \cos\phi \\ -\frac{i}{\sqrt{2}} \sin\phi e^{i\theta} \end{bmatrix}. \tag{1.198}$$

Using eq. (1.178), the QFI for this state is calculated as:

$$F[|\psi_\phi(\theta)\rangle, \hat{S}_z] = 4\left(\langle\psi_\phi(\theta)|\hat{S}_z^2|\psi_\phi(\theta)\rangle - (\langle\psi_\phi(\theta)|\hat{S}_z|\psi_\phi(\theta)\rangle)^2\right) \tag{1.199}$$

$$= 4(\begin{pmatrix} \frac{i}{\sqrt{2}} \sin\phi e^{i\theta} & \cos\phi & \frac{i}{\sqrt{2}} \sin\phi e^{-i\theta} \end{pmatrix} \begin{pmatrix} -\frac{i}{\sqrt{2}} \sin\phi e^{-i\theta} \\ 0 \\ -\frac{i}{\sqrt{2}} \sin\phi e^{i\theta} \end{pmatrix}$$

$$+ \begin{pmatrix} \frac{i}{\sqrt{2}} \sin\phi e^{i\theta} & \cos\phi & \frac{i}{\sqrt{2}} \sin\phi e^{-i\theta} \end{pmatrix} \begin{pmatrix} -\frac{i}{\sqrt{2}} \sin\phi e^{-i\theta} \\ 0 \\ \frac{i}{\sqrt{2}} \sin\phi e^{i\theta} \end{pmatrix}) \tag{1.200}$$

$$= 4(\sin^2\phi + 0) = 4\sin^2\phi \tag{1.201}$$

Compared to the single qubit case, the QFI for a single NV center has an additional factor of 4. This means that the maximum QFI of a single NV center can be four times larger when the initial state is a superposition of the $|-1\rangle$ and

$|+1\rangle$ states:

$$|\psi_{\pi/2}(0)\rangle = -\frac{i}{\sqrt{2}}(|+1\rangle + |-1\rangle)) \tag{1.202}$$

$$|\psi_{3\pi/2}(0)\rangle = \frac{i}{\sqrt{2}}(|+1\rangle + |-1\rangle)) \tag{1.203}$$

The factor of 4 arises from the contribution of an additional excited state in the spin-1 system. To demonstrate this, consider a general pure state:

$$|\psi_{\text{gen}}\rangle = \begin{pmatrix} \sqrt{a} \\ \sqrt{1-a^2-b^2} \\ \sqrt{b} \end{pmatrix} \tag{1.204}$$

, where a, $\sqrt{1-a^2-b^2}$, and b represent the probabilities of the $|+1\rangle$, $|0\rangle$, and $|-1\rangle$ states, respectively. The QFI for this state is:

$$F(|\psi_{\text{gen}}\rangle, \hat{S}_z)/4 = \begin{pmatrix} \sqrt{a} & \sqrt{1-a^2-b^2} & \sqrt{b} \end{pmatrix}^* \begin{pmatrix} \sqrt{a} \\ \sqrt{1-a^2-b^2} \\ \sqrt{b} \end{pmatrix}$$

$$- \left[\begin{pmatrix} \sqrt{a} & \sqrt{1-a^2-b^2} & \sqrt{b} \end{pmatrix}^* \begin{pmatrix} \sqrt{a} \\ \sqrt{1-a^2-b^2} \\ -\sqrt{b} \end{pmatrix} \right]^2 \tag{1.205}$$

$$= |a| + |b| - (|a| - |b|)^2 \tag{1.206}$$

As shown in fig. 1.21a, the QFI reaches its maximum value when $|a| = |b| = 0.5$, which corresponds to the equal superposition of the $|+1\rangle$ and $|-1\rangle$ states. In cases where only one excited state is involved (e.g., under a strong magnetic field where the Zeeman splitting is large), the system effectively reduces to a two-level system. Assuming $|b| = 0$, the QFI becomes:

$$F(|\psi_{\text{gen}}\rangle, \hat{S}_z) = 4(|a| - |a|^2) \tag{1.207}$$

$$\frac{\partial F(|\psi_{\text{gen}}\rangle, \hat{S}_z)}{\partial |a|} = 4(1 - 2|a|) = 0 \tag{1.208}$$

$$|a| = 1/2 \tag{1.209}$$

$$\max(F) = F_{|a|=0.5,|b|=0} = 1. \tag{1.210}$$

This result, shown in fig. 1.21b, agrees with the maximum QFI for a single qubit case in eq. (1.186).

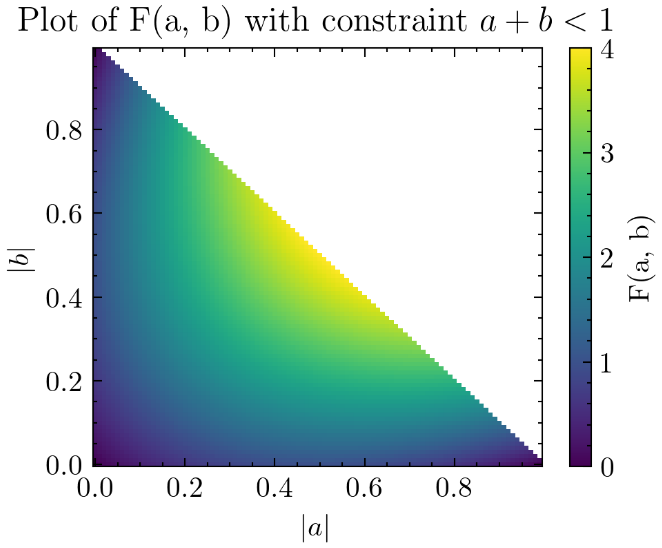

(a) QFI for a single NV center as a function of the probabilities of the $|+1\rangle$ and $|-1\rangle$ states. The QFI is maximized when the initial state is an equal superposition of the two excited states.

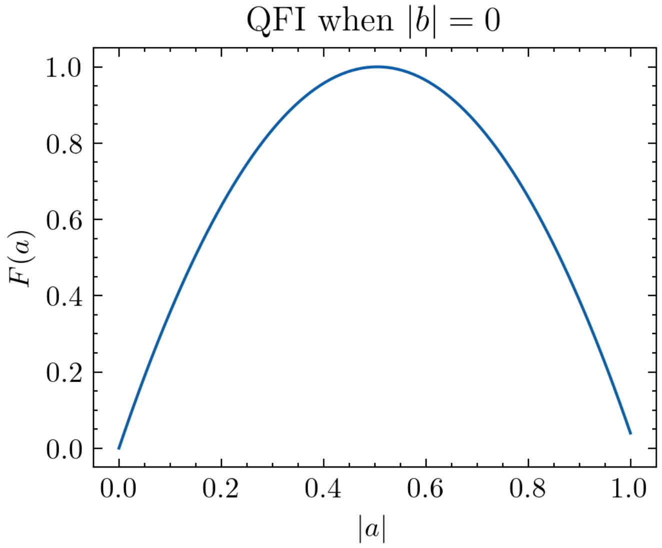

(b) QFI for an NV center reduced to a two-level system by setting $P(|-1\rangle) = 0$. The maximum QFI is 1, consistent with the single qubit case.

Figure 1.21

1.11.4 QFI calculation with tensor network

When the system has a large Hilbert space size, i.e., a large number of spins N, using eq. (1.172) becomes inefficient and undesirable. This is because it requires access to the eigenvalues of the quantum state, which involves diagonalizing ρ, a computationally expensive task.

To address this issue, extracting the QFI directly from tensor network states is necessary. We adopt a tensor network framework for calculating QFI, as proposed in [6]. This framework utilizes a tensor network ansatz to represent the symmetric logarithmic derivative (SLD). By optimizing this ansatz, which involves solving a set of linear equations, the SLD satisfying eq. (1.169) can be obtained. Thus, the problem shifts from eigenvalue computation to tensor optimization. Note that, unlike the original work, we only optimize the SLD and not the input state ρ.

As an alternative to eqs. (1.169) and (1.172), the QFI is now defined as:

$$F(\rho_\phi, L) = \sup_L [2\mathrm{Tr}(\rho'_\theta L) - \mathrm{Tr}(\rho_\theta L^2)]. \tag{1.211}$$

where $\sup_L$ denotes the maximum value over all possible candidates of L.

Since the QFI obtained from this approach relies on local optimization, it can vary depending on the initial values of L. Therefore, multiple calculations with different initial L values are required. These variations depend on the complexity of the optimization landscape, which is influenced by the model's complexity.

The optimal SLD, L^*, satisfies $\rho'_\theta = \frac{1}{2}(L_\theta \rho_\theta + \rho_\theta L_\theta)$, yielding eq. (1.169) from eq. (1.211). The parameterized quantum state evolves from the initial state via the noise channel Λ and the unitary operator:

$$\rho_\theta = \Lambda_\theta(\rho_0) = e^{-iH\theta}\Lambda(\rho_0)e^{iH\theta}. \tag{1.212}$$

To solve eq. (1.211), the symmetric logarithmic derivative L is represented as a matrix product operator (MPO) with a finite bond dimension D_L:

$$L = \sum_{jk} \mathrm{Tr}(S[1]^{j_1}_{k_1} \dots S[n]^{j_n}_{k_n}) |\mathbf{j}\rangle\langle\mathbf{k}|. \tag{1.213}$$

Here, $S[l]^{j_l}_{k_l}$ is a Hermitian matrix whose elements are initialized randomly. If the quantum channel has no noise or only uncorrelated noise, D_L is set to ≤ 2. Otherwise, the optimal value can be determined by incrementally increasing D_L and recalculating until the resulting QFI shows marginal improvement.

The matrix product density operator (MPDO) ρ'_θ is efficiently computed as:

$$|\rho'_\theta\rangle\rangle = -i(\hat{H} \otimes \hat{1} - \hat{1} \otimes \hat{H})|\rho_\theta\rangle\rangle. \tag{1.214}$$

To find the optimal L, the tensors $(S[1]^{j_1}_{k_1}, \dots, S[n]^{j_n}_{k_n})$ are updated locally, starting from $S[1]$ to $S[n]$ and then back to $S[1]$, iteratively, until F converges. For example, when updating $S[l]^{j_l}_{k_l}$, all other tensors S^j_k are contracted, and the uncontracted indices are vectorized. After contraction, eq. (1.211) reduces to a linear equation:

$$F(\rho, L) = 2\sum_\alpha b_\alpha S[l]_\alpha - 2\sum_{\alpha\beta} S[l]_\alpha A_{\alpha\beta} S[l]_\beta. \tag{1.215}$$

Here, $\vec{b}$ and $\hat{A}$ are a vector and a matrix, respectively, obtained by contracting the fixed tensors and combining the uncontracted indices. The construction of $\vec{b}$ and $\hat{A}$ during the optimization of $S[2]$ is illustrated in fig. 1.22.

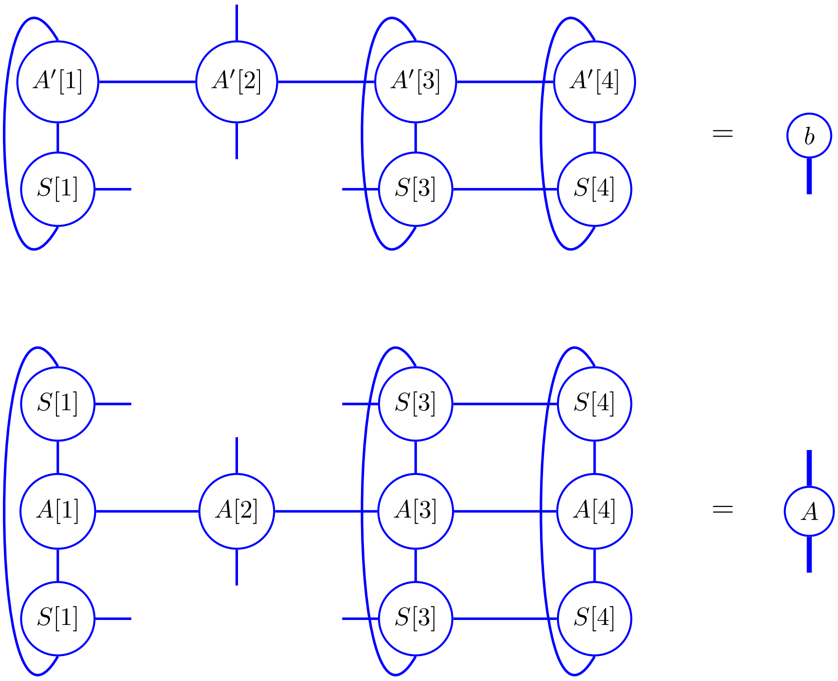

Figure 1.22: When updating $S[2]$, $\vec{b}$ and $\hat{A}$ in eq. (1.215) are constructed by contracting all tensors except those related to the tensor being updated. The uncontracted indices are combined to form a vector or matrix.

The tensor $S[l]$ that maximizes the QFI locally can be found by taking the

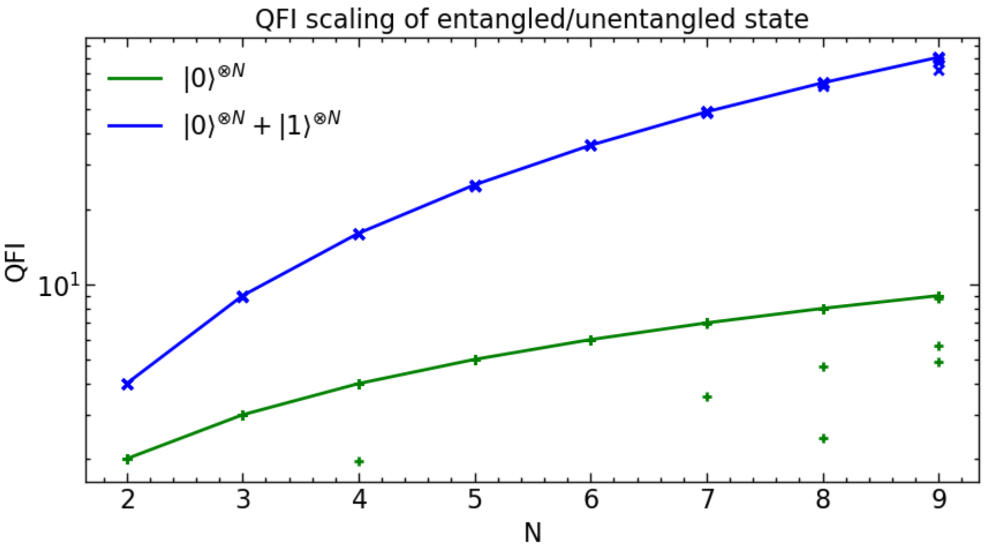

Figure 1.23: QFI computed by optimizing L in eq. (1.211). The maximum values for a product state and an entangled state scale as N and N^2, respectively.

derivative of eq. (1.215) with respect to $S[l]$:

$$\frac{\partial F(\rho, L)}{\partial S[l]} = 0. \tag{1.216}$$

This yields:

$$\frac{1}{2}(A + A^T)|S[l]\rangle = |b\rangle \tag{1.217}$$

$$|S[l]\rangle = \tilde{A}^{-1}|b\rangle. \tag{1.218}$$

The new $S[l]$ is then updated using the solution of this inverse problem. The updating process stops when the QFI converges, and the final value is obtained.

For demonstration, the QFI is computed for N independent NV centers measuring a uniform magnetic field B_z. The NV probes are assumed to be in either i) a product of ground states or ii) a maximally entangled state. As shown in fig. 1.23, the maximum QFI scales as N and N^2, respectively, as expected. However, since this local update approach tends to get stuck in local extrema, several repetitions with different initial L values are required, which can be computationally expensive for large N.

Chapter 2

Results

Partial of this chapter contains the results of the published manuscript [40] with the following contributions:

Author	Author position	Scientific ideas (%)	Data generation (%)	Analysis & interpretation (%)	Paper writing (%)
Jirawat Saiphet	1	50	100	70	80
Daniel Braun	2	50	0	30	20
Title of paper: Simulation of the Dissipative Dynamics of Strongly Interacting NV Centers with Tensor Networks					
Status in publication process: Published					

2.1 Reconstruct Magnetic Field from ODMR

In the presence of an external magnetic field, NV centers with different principal axis orientations become distinguishable via Optically Detected Magnetic Resonance (ODMR). Due to the different alignments of their principal axes relative to the external magnetic field , the distinct NV orientations exhibit energy level splittings of different magnitudes, as observed in the ODMR spectrum. This distinction fails only at specific magnetic field orientations where these splittings become degenerate [57]. While the magnitude of the magnetic field projection along each NV axis, $B_z^{(i)}$, can be determined from the ODMR spectrum (as it is proportional to the Zeeman splitting), the full vector $\vec{B}$, including its direction, can also be reconstructed from the same data. This section details the procedure for reconstructing the external magnetic field vector using the ODMR splitting information.

As illustrated in fig. 2.1, $B_z^{(i)}$ represents the projection of the external magnetic field $\vec{B}$ onto the principal axis $\hat{c}i$ of the i-th NV center orientation. For a single

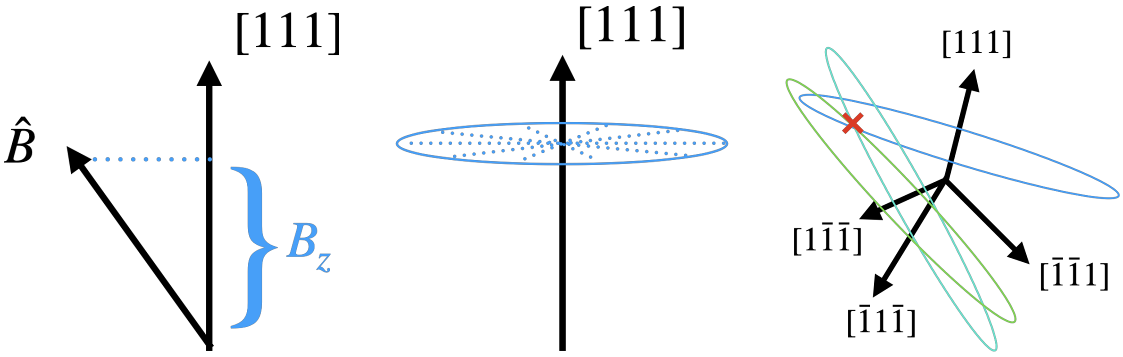

(a) (b) (c)

Figure 2.1: Reconstruction of the magnetic field vector $\vec{B}$ from its projections. (a) The projection of $\vec{B}$ onto the i-th NV principal axis, $B_z^{(i)} = \vec{B} \cdot \hat{c}_i$, determines the corresponding Zeeman splitting. (b) For a fixed $B_z^{(i)}$ (e.g., along the [111] axis), the endpoint of the vector $\vec{B}$ must lie on a specific plane perpendicular to $\hat{c}_i$. (c) The vector $\vec{B}$ is uniquely determined by the intersection point of three distinct planes, each defined by the measured projection onto a different NV axis.

orientation i, the condition $\vec{B} \cdot \hat{c}i = Bz^{(i)}$ defines a plane perpendicular to $\hat{c}i$. If the magnitude $|\vec{B}|$ is known, this condition restricts the possible directions of $\vec{B}$ such that the vector's endpoint lies on this plane. The equations defining these planes for the four possible NV axis alignments are as follows:

$$\begin{aligned}
[111] &: b_x + b_y + b_z = \sqrt{3}\cos\Big(\theta_{[111]}\Big), \\
[1\bar{1}\bar{1}] &: b_x - b_y - b_z = \sqrt{3}\cos\Big(\theta_{[1\bar{1}\bar{1}]}\Big), \\
[\bar{1}1\bar{1}] &: -b_x + b_y - b_z = \sqrt{3}\cos\Big(\theta_{[\bar{1}1\bar{1}]}\Big), \\
[\bar{1}\bar{1}1] &: -b_x - b_y + b_z = \sqrt{3}\cos\Big(\theta_{[\bar{1}\bar{1}1]}\Big),
\end{aligned} \tag{2.1}$$

where $\vec{b} = (b_x, b_y, b_z)$ is the unit vector along $\vec{B}$ (i.e., $\vec{B} = |\vec{B}|\vec{b}$), and $\cos(\theta_i) = B_z^{(i)}/|\vec{B}|$ relates the measured projection $B_z^{(i)}$ to the angle θ_i between $\vec{B}$ and the i-th principal axis $\hat{c}i$. The direction vector $\vec{b}$ corresponds to the common intersection point of these planes. Consequently, the components (bx, b_y, b_z) can be found by solving a system of three independent equations chosen from the set of four in eq. (2.1), provided the magnitude $|\vec{B}|$ is known (allowing the calculation of $\cos(\theta_i)$ from the measured $B_z^{(i)}$ values). We utilize the ODMR data from [21]. The relevant parameters are as follows:

- The magnitude of the magnetic field is $|\vec{B}| = 9\,\mathrm{mT}$.
- The Zeeman splittings $2B_z^{(i)}$ are approximately $(401, 308, 214, 117)\,\mathrm{MHz}$, derived from the ODMR spectrum, with associated uncertainties of $(\pm 15, \pm 6, \pm 7, \pm 3)\,\mathrm{MHz}$.

- It is assumed that the splittings correspond to the NV orientations [111], $[1\bar{1}\bar{1}]$, $[\bar{1}1\bar{1}]$, and $[\bar{1}\bar{1}1]$, respectively.

Three out of the four equations in eq. (2.1) are solved using the following Python script to determine $\vec{B}$.

```python
import numpy as np
import scipy.optimize as optimize
"""
Solve equations for a unit vector of B.
"""
def f(x):
    return [sign[0][0]*x[0] + sign[0][1]*x[1] + sign[0][2]*x[2] - np.sqrt(3)*cos_theta[0],
            sign[1][0]*x[0] + sign[1][1]*x[1] + sign[1][2]*x[2] + np.sqrt(3)*cos_theta[1],
            sign[2][0]*x[0] + sign[2][1]*x[1] + sign[2][2]*x[2] + np.sqrt(3)*cos_theta[2]]
sign = np.array([    [1.,  1.,  1.],
                     [ 1., -1., -1.],
                     [-1.,  1., -1.]     ])
Bvec = optimize.fsolve(f, [0,0,0]) #initial guess = (0,0,0)
```

As a result, $(b_x, b_y, b_z) = (0.16996038, 0.33133691, 0.89615474)$. To validate this result, we calculate the Zeeman splittings using the Hamiltonian:

$$\hat{H} = DS_z^2 + \gamma B_z^{(i)}, \tag{2.2}$$

where D represents the zero-field splitting parameter, γ is the gyromagnetic ratio, and $B_z^{(i)}$ is the magnetic field projection along the z-axis for the i-th NV orientation.

However, the recalculated Zeeman splittings show poor agreement with the original ODMR spectrum, as illustrated in fig. 2.2.

To improve the accuracy of our calculations, a correction is applied to the Hamiltonian in eq. (2.2) by incorporating all interaction terms with the magnetic field:

$$\begin{aligned} \hat{H} &= DS_z^2 + \gamma \vec{B} \cdot \vec{S} \\ &= DS_z^2 + \gamma |B| (\sin\theta \cos\phi \hat{S}_x \sin\theta \sin\phi \hat{S}_y + \cos\theta \hat{S}_z) \\ &= DS_z^2 + \gamma B_z \hat{S}_z + \gamma (B_x \hat{S}_x + B_y \hat{S}_y), \end{aligned} \tag{2.3}$$

Since $D \gg \gamma(B_x, B_y)$, the additional terms are treated as a perturbation Hamilto-

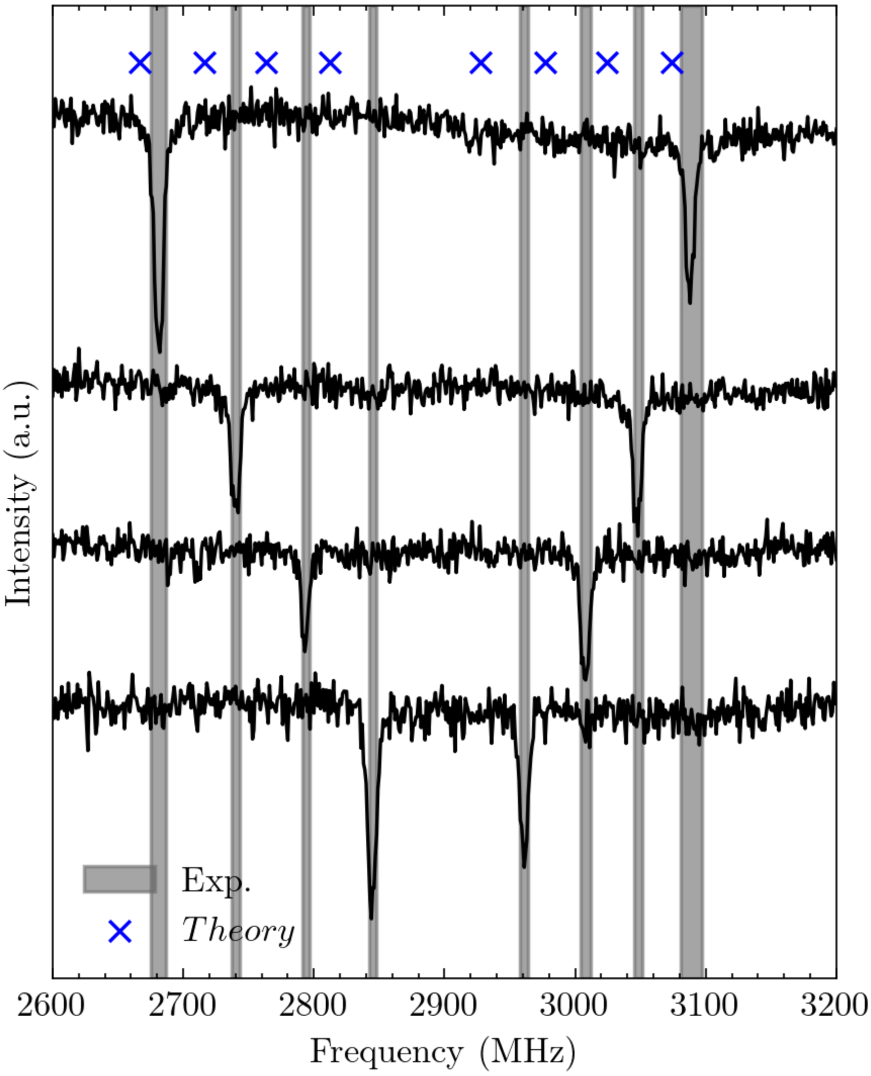

Figure 2.2: Zeeman splittings calculated using the first-order Hamiltonian do not match the experimental ODMR spectrum.

nian:

$$\hat{V} = \frac{\gamma}{\sqrt{2}} \begin{bmatrix} 0 & B_x - iB_y & 0 \\ B_x + iB_y & 0 & B_x - iB_y \\ 0 & B_x + iB_y & 0 \end{bmatrix}. \tag{2.4}$$

The energy contribution from the first-order perturbation is given by:

$$E_n^{(1)} = \langle n^{(0)}|\hat{V}|n^{(0)}\rangle; \qquad |n^{(0)}\rangle = \begin{bmatrix} |+1\rangle \\ |0\rangle \\ |-1\rangle \end{bmatrix}, \tag{2.5}$$

$$E_{|-1\rangle}^{(1)} = \begin{bmatrix} 0 & 0 & 1 \end{bmatrix} \hat{V} \begin{bmatrix} 0 \\ 0 \\ 1 \end{bmatrix} = 0, \tag{2.6}$$

$$E_{|0\rangle}^{(1)} = \begin{bmatrix} 0 & 1 & 0 \end{bmatrix} \hat{V} \begin{bmatrix} 0 \\ 1 \\ 0 \end{bmatrix} = 0, \tag{2.7}$$

$$E_{|+1\rangle}^{(1)} = \begin{bmatrix} 1 & 0 & 0 \end{bmatrix} \hat{V} \begin{bmatrix} 1 \\ 0 \\ 0 \end{bmatrix} = 0. \tag{2.8}$$

Since all first-order corrections are zero, we proceed to the second-order perturbation:

$$E_n^{(2)} = \left(\frac{\gamma}{\sqrt{2}}\right)^2 \sum_{k \neq n} \frac{|\langle k|\hat{V}|n\rangle|^2}{E_n^{(0)} - E_k^{(0)}}, \tag{2.9}$$

$$E_{|-1\rangle}^{(2)} = \frac{\gamma^2}{2}\left(\frac{|\langle +1|\hat{V}|-1\rangle|^2}{E_{|-1\rangle}^{(0)} - E_{|+1\rangle}^{(0)}} + \frac{|\langle 0|\hat{V}|-1\rangle|^2}{E_{|-1\rangle}^{(0)} - E_{|0\rangle}^{(0)}}\right) = \frac{B_x^2 + B_y^2}{2D}, \tag{2.10}$$

$$E_{|+1\rangle}^{(2)} = \frac{\gamma^2}{2}\left(\frac{|\langle 0|\hat{V}|+1\rangle|^2}{E_{|+1\rangle}^{(0)} - E_{|0\rangle}^{(0)}} + \frac{|\langle -1|\hat{V}|+1\rangle|^2}{E_{|+1\rangle}^{(0)} - E_{|-1\rangle}^{(0)}}\right) = \frac{B_x^2 + B_y^2}{2D}, \tag{2.11}$$

$$E_{|0\rangle}^{(2)} = \frac{\gamma^2}{2}\left(\frac{|\langle -1|\hat{V}|0\rangle|^2}{E_{|0\rangle}^{(0)} - E_{|-1\rangle}^{(0)}} + \frac{|\langle +1|\hat{V}|0\rangle|^2}{E_{|0\rangle}^{(0)} - E_{|+1\rangle}^{(0)}}\right) = \frac{-(B_x^2 + B_y^2)}{D}. \tag{2.12}$$

Since $B_x^2 + B_y^2 = |\vec{B}|^2 - B_z^2$, the energy levels of $|\pm 1\rangle$ are shifted by the same amount:

$$\begin{aligned} |\Delta E_{|\pm1\rangle}| &= E_{|\pm1\rangle}^{(2)} - E_{|0\rangle}^{(2)}, \\ &= \frac{3}{2}\frac{|\vec{B}|^2 - B_z^2}{D}. \end{aligned} \tag{2.13}$$

It is important to note that B_z differs for each NV center orientation. After

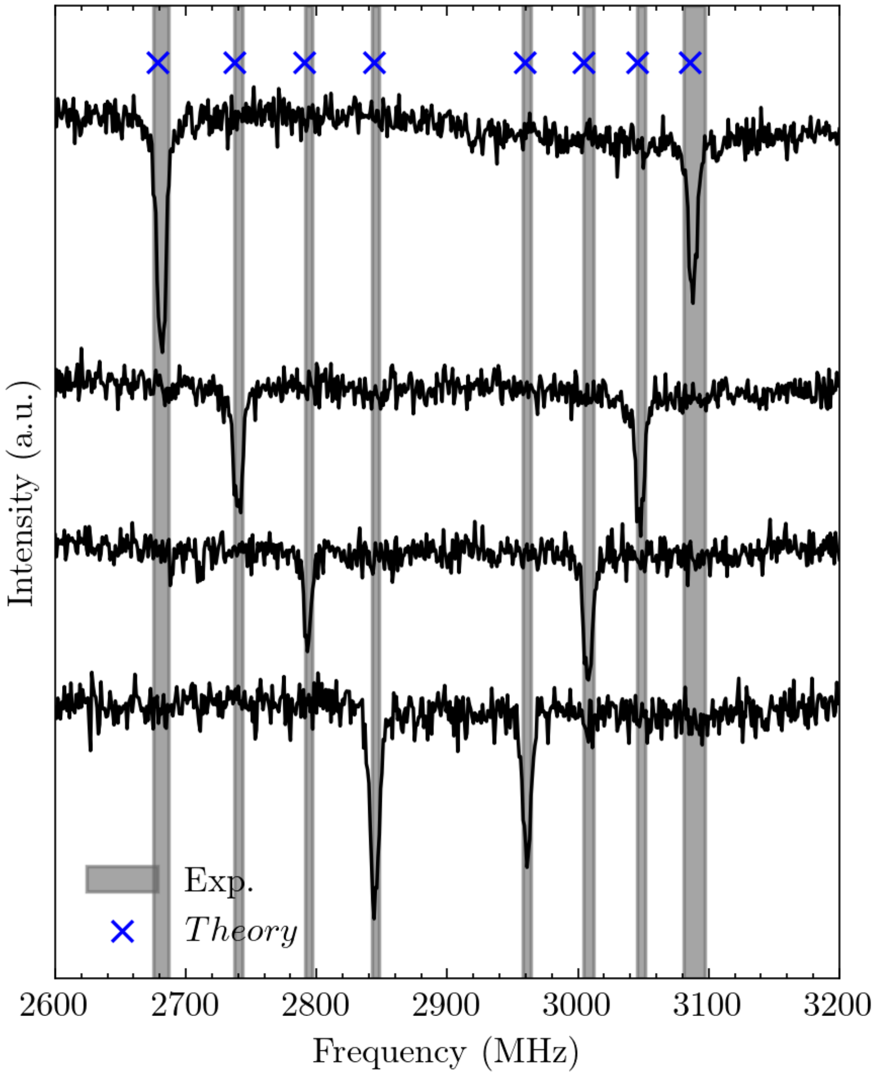

Figure 2.3: Zeeman splittings calculated after incorporating the second-order perturbation corrections match the experimental ODMR spectrum.

incorporating the corrections from eq. (2.13) into eq. (2.2), the calculated Zeeman splittings align with the experimental ODMR spectrum, as shown in fig. 2.3.

The time-evolution of the quantum state is governed by the Schrödinger equation and the master equation for a closed system and an open system, respectively. To simulate the dynamics of the quantum state, we need to solve these differential equaitons. For a small system, obtaining the exact dynamics is possible with the exact diagonalization (ED) method. However, as the system size increases slightly, the ED method becomes drastically inefficient due to its exponential computational complexity, and a simulation technique with more cost-efficient is required.

Since we are interested in the dynamics of the NV ensemble that have a long-range interaction, we need the MPS-based algorithm that supports the long-range Hamiltonian. For this reason, the algorithm that based on Trotter-Suzuki decomposition, such as the time-evolving block decimation (TEBD) algorithm, is not a suitable choice for the long-range interaction model because it is designed for the nearest-neighbor Hamiltonian. Even though long-range interaction model can be implemented by using swap gates, the error of the approximation increases with the interaction range because we need to perform the Trotter-Suzuki decomposition on the non-commuting operators; the errors is proportional to the number of swap gates that are required to implement the long-range interaction [3]. Furthermore, introducing the swap gates increasess exponentially overheads in the algorithm, which makes the algorithm less efficient [5].

Instead, we consider the real-time evolution algorithms that support the long-range model: i) time-dependent variational principle (TDVP) algorithm (section 1.8.2) and ii) W^{II} algorithm (section 1.8.1). In the following, we compare the runtime and validate the accuracy of two algorithms in simulating a long-range and strongly-interacting spin system. Then we discuss the results from simulations of the one-dimensional NV centers ensemble model.

2.2 Algorithms comparison

2.2.1 Simulation time complexity

First of all, we assess the computational complexity of each algorithm by measuring its simulation time. Specifically, the simulation time is the total time spent to execute a complete simulation run. To break down what this entails, for TDVP and W^{II}, the simulation time includes the construction of the tensor network state (MPS or MPDO) and operators (MPO), as well as the subsequent time evolution of the initial state. For exact diagonalization (ED), the simulation time comprises the time required to diagonalize the full Hamiltonian and apply the resulting time-evolution operator to the quantum state. The simulation times were measured using a local machine configured with an Intel i5-10500 processor (3.10 GHz, 12 cores), 64 GB of RAM, and running the Ubuntu 22.04 LTS operating system.

For fig. 2.4, we measured the simulation times for the real-time evolution under long-range interaction of a pure state, where the state was represented by an MPS, over 100 timesteps. The system sizes are up to $N = 10$ spins for tensor network methods. In the area of small N, ED is faster than both algorithms since there are more computational overheads in tensor calculations. However, the exponential scaling of ED increases its simulation time dramatically fast after $N = 6$, making it inefficient method. While using the tensor network shows slower growth in the simulation time due to the linear scaling from fixed bond dimenison. Note that the results from ED are only limited to $N = 9$ bacause our machine is running out of memory. Since our model is spin-1 particle that has a local dimension $d = 3$. Finding a diagonalization of $d^N \times d^N$ has a complexity scale of $\mathcal{O}(d^{3N})$. Hence, the maximum simulatible size by ED is quickly reached compared with the case of qubit model.

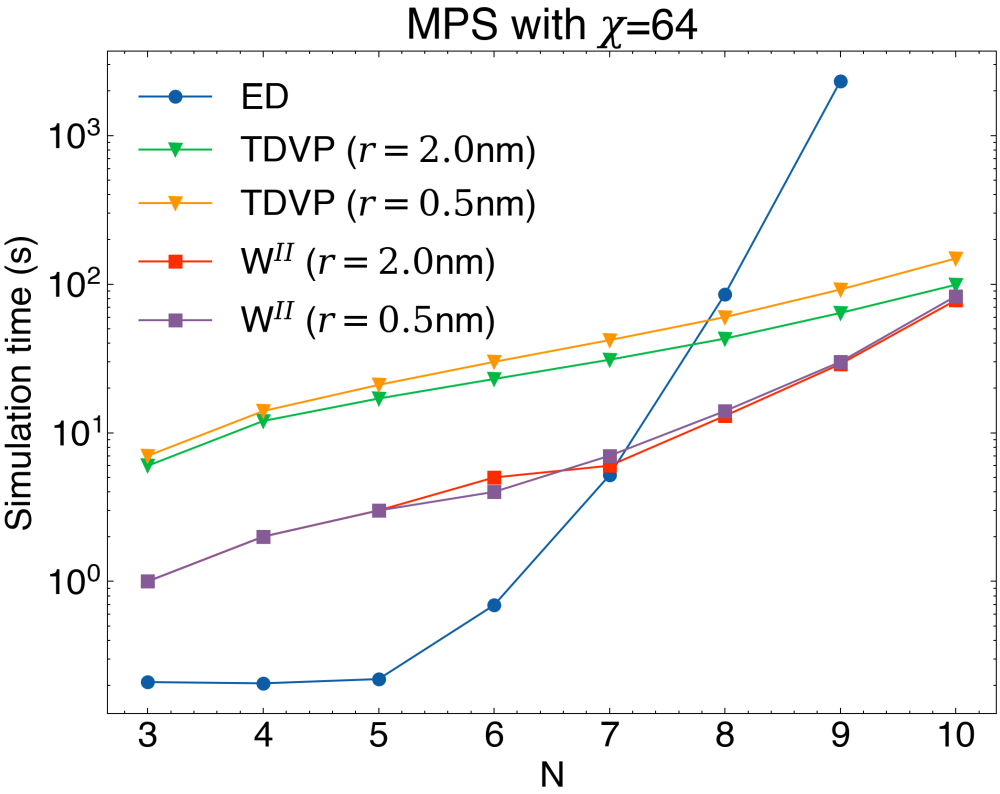

Figure 2.4: Total simulation times taken to simulate dynamcis for 100 timesteps using MPS by the exact diagonalization (ED), time-dependent variational principle (TDVP), and MPO W^{II} methods. The ED results are available only up to N=9 due to insufficient memory. The bond dimension of MPS is set to be 64 for TDVP and W^{II} algorithms.

fig. 2.5 illustrates the computational cost of simulating the real-time evolution of mixed states, using the MPDO formalism, again for a duration of 100 timesteps. As with the pure-state MPS simulations (see fig. 2.4), exact diagonalization (ED) initially outperforms tensor network methods for the smallest system sizes ($N = 2$ and $N = 3$). This efficiency is short-lived, however, as the inherent computational complexity of tensor network operations—such as contractions and singular value decompositions (SVDs)— quickly becomes surpassed by the exponential scaling of ED. In fact, ED's rapid memory requirements limited our simulations to $N = 4$, as reflected in fig. 2.5a. While MPDO simulations introduce errors from truncations, they enable calculations for larger systems. This increased capability stems from the fact that directly representing the vectorized density operator and the Liouvillian superoperator requires considerably more memory than the compressed MPDO format. By employing a constant bond dimension χ, MPDO significantly mitigates this memory demand, thus extending the reach of our simulations beyond what is feasible with ED. Notably, this demonstrates the value of tensor network techniques for simulating the dynamics of mixed states in extended quantum systems.

Comparing the two tensor network algorithms, we observe that the W^{II} method exhibits greater efficiency than TDVP for small system sizes (N). This difference likely originates from the dominant computational cost of applying an MPO directly to an MPS or MPDO, which scales as $\mathcal{O}(\chi_{\mathrm{MPO}}^3 d_{\mathrm{MPO}})$, where χ_{MPO} represents the MPO bond dimension and d_{MPO} is the local dimension [33]. In contrast, the variational approach employed by the two-site TDVP algorithm incurs a cost of $\mathcal{O}(3\chi_{\mathrm{MPO}} d_{\mathrm{MPO}})$. For small systems, the MPO bond dimension is relatively low due to fewer interacting pairs, resulting in a smaller value for χ_{MPO}. Consequently, the larger constant factor in the TDVP's cost renders it less computationally efficient in this regime. However, this constant becomes less significant as the system size (N) increases. With larger N, χ_{MPO} also grows, eventually dominating the computational cost, which favors TDVP's linear scaling. This transition is evident in the steeper increase in simulation times for the W^{II} method compared to TDVP, as illustrated in figs. 2.4 and 2.5a for larger N. To further validate this observation, we performed an additional comparison with both algorithms using a reduced MPDO bond dimension of $\chi_{\mathrm{MPDO}} = 16$ (see fig. 2.5b). In this scenario, we find that TDVP becomes more efficient than W^{II} for systems with $N > 7$.

2.2.2 Numerical accuracy and stability

Beyond assessing time complexity, we also evaluated the numerical accuracy and stability of the algorithms. While the MPS is a powerful technique for a wide range of quantum many-body systems, executing an MPS-based algorithm with MPDO can become unstable in an extreme condition. The instability arises because MPDO does not guarantee positivity of the quantum state [52]. Also, MPDO has larger bond dimensions compared to MPS, thus, it possibly has bigger accumulated numerical errors from an approximation procedure in the algorithm. Since the MPS/MPDO are a low-rank approximation of the full quantum state, the bond dimension χ is a key parameter that determines the accuracy of the approximation. For this reason, we have to carefully verify if the simulation techniques can provide reliable results for the NV ensemble at the limit of strong coupling.

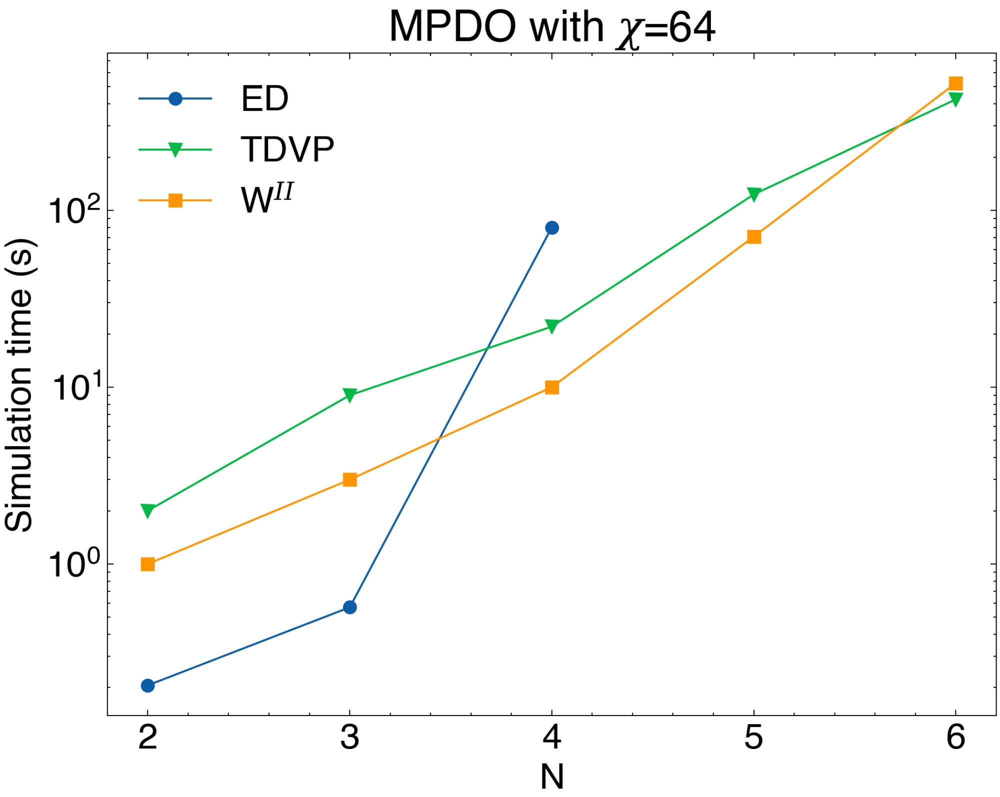

(a) Total simulation times taken to simulate dynamcis for 100 timesteps using MPDO.The ED results are available only up to N=4 due to insufficient memory.

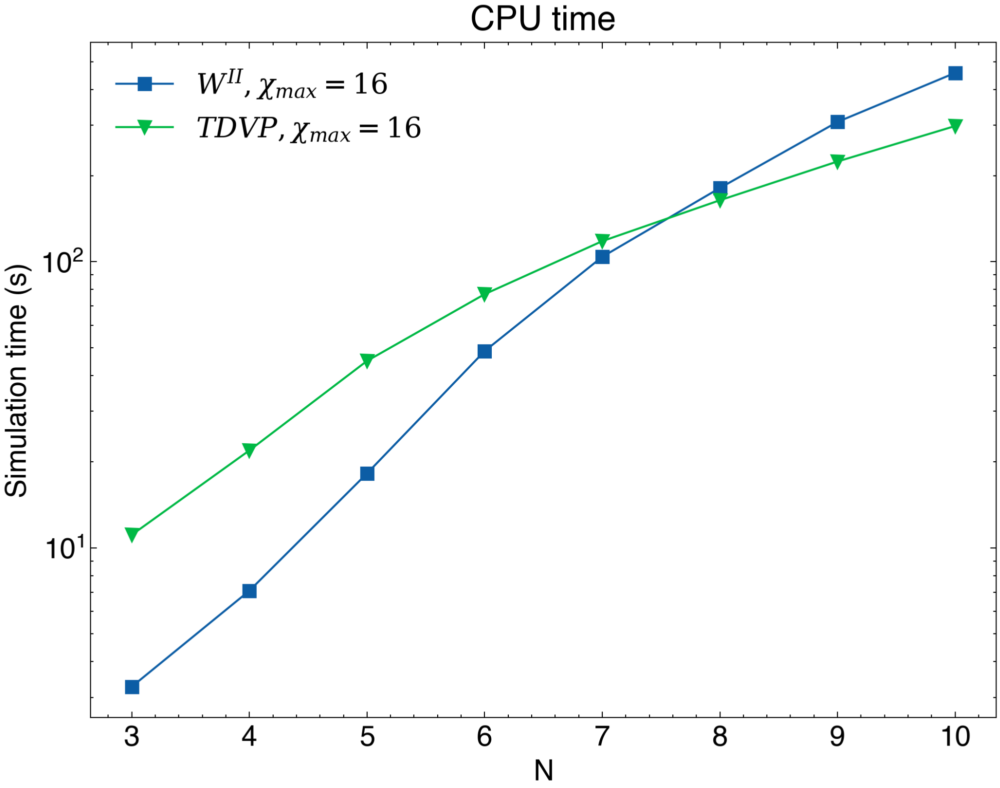

(b) In terms of simulation time, TDVP underperforms W^{II} in a small system but outperforms in the bigger system.

Figure 2.5

In order to verify how reliable the TDVP and W^{II} algorithms are, we investigate its numerical accuracy and stability in the certain parameter regime. We simulate the dynamcis of a spin-1 system in one dimensional chain with long-range ZZ interaction Hamiltonian, as in eq. (1.50), $\hat{H}_{ij} = (C_{ij}/r_{ij}^3)S_i^z S_j^z$. The local terms $\hat{H}_i = (D-\omega)(S_i^z)^2 + \Omega S_i^x$ is coupling $|0\rangle \leftrightarrow |-1\rangle$. The quantum state is given in MPDO of $|m_s = 0\rangle^{\otimes N}$ with maximum bond dimension $\chi_{\max} = 16$. fig. 2.6 we

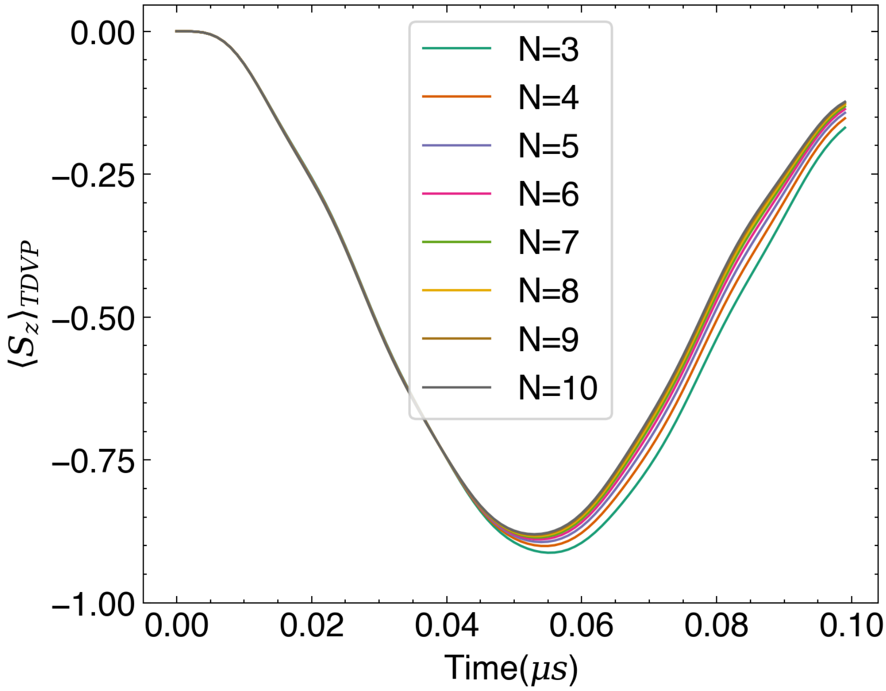

Figure 2.6: Expectation value $\langle S_z \rangle$ for 100 time steps calculated by TDVP with different number of spins N. The nearest spins are separated by $r = 2\,\text{nm}$

simulate real-time evolution of spin chains that consist of N spins, for from N =3 to N =10, and calculate an expectation value of the observable $\langle S_z \rangle / N$ for the first 100 timesteps. The results calculated by the two algorithms are given in two subfigures of fig. 2.7. First of all, we investigate that the same dynamics are produced from both W^{II} and TDVP. This is shown as insignificant discrepancy in the real part of $\langle S_z \rangle$ of the whole system produced by both methods, see fig. 2.7a. However, if considering in an imaginary part, which should be close to zero for an observable, we find the TDVP's results have 6 order-of-magnetude smaller than W^{II}'s. This is shown in fig. 2.7b. Furthermore, we observe numerical instability under certain condition in the W^{II} method; when the interaction is very strong and becomes more complex. Even when the system is as small as $N = 3$, shown in fig. 2.8, we use the interaction Hamiltonian in eq. (1.50) and let $r = 0.5$ nm. Here, the algorithm fails to produce a normalized value for expected magnetization, yielding $|\langle S_z \rangle / N| \ggg 1$. This observable divergence is not observed in the TDVP. We also

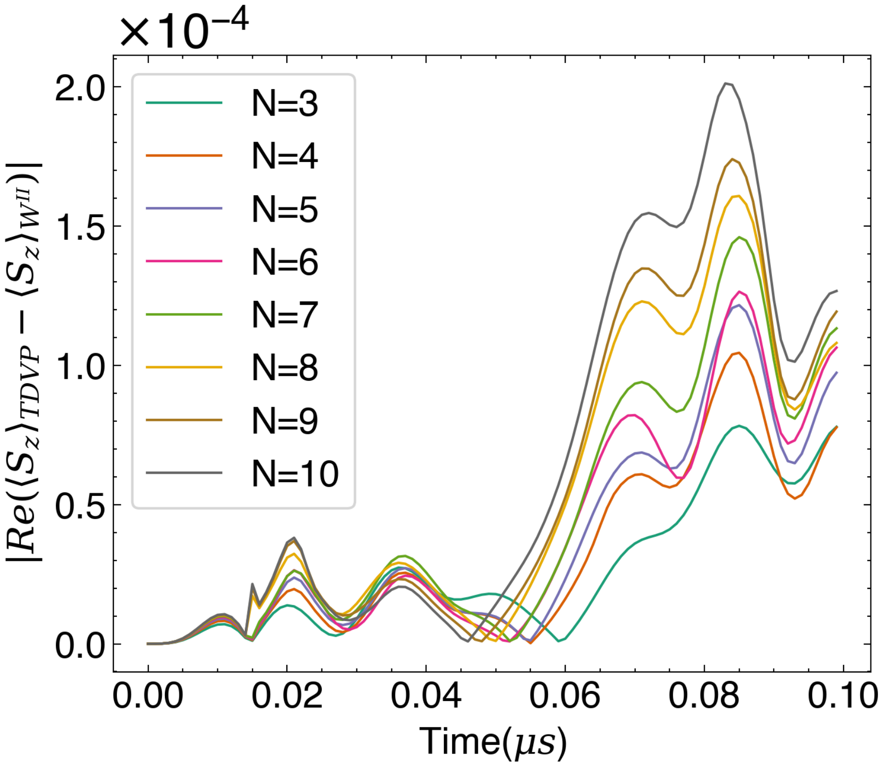

(a) The diffrent in real part of the observable, average magnetization of the system, calculated from TDVP and W^{II} algorithms.

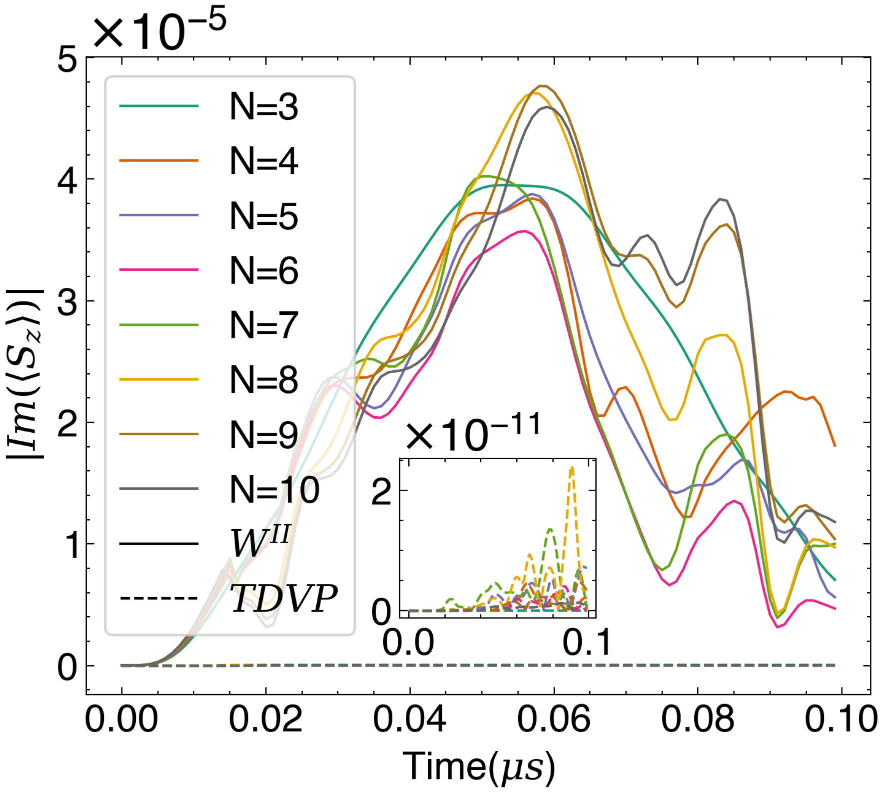

(b) Numerical errors of TDVP and W^{II} algorithms represented by an imaginary part of the observable. Results from TDVP shows significantly lower by 6 order-of-magnetude.

Figure 2.7

calculate the exact dynamics from the exact diagonalization method as a benchmark, which well validates the TDVP's result. We suspect that the large imaginary value and observable divergence in W^{II} are results of exploiting the complex time steps technique mentioned in section 1.8.1 to improve the propagation error. As using the technique does not preserve unitarity of the propagator. However, without the technique, the numerical error of propagating the quantum state with W^{II} method compared to the exact evolution dramatically degrades from $\mathcal{O}(dt^2)$ to $\mathcal{O}(dt)$. In this case, the algorithm would not be able to capture the correct dynamics even in the weaker interaction regime. Since the W^{II} method exhibits limitations in the strong interaction regime, rendering it inadequate for our purposes. Therefore, we select TDVP as a main algorithm in our simulations. In later sections, all tensor network simulation of NV centers ensemble are produced by TDVP.

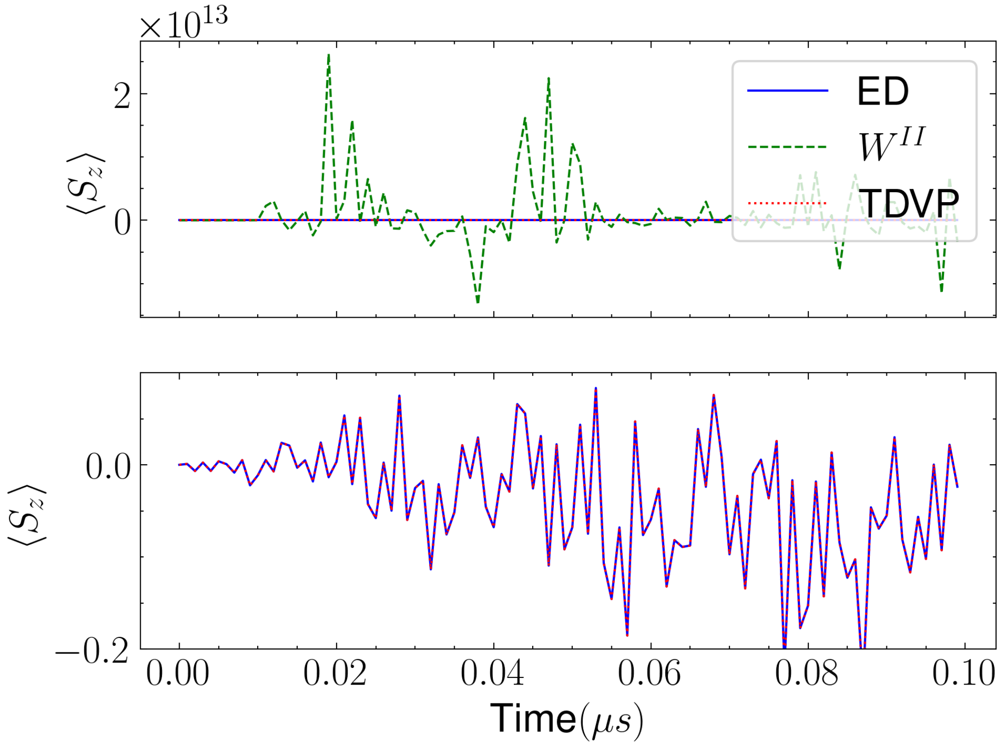

Figure 2.8: W^{II} method becomes instable when interaction is stronger and more complex, leading to the unphysical observable. Meanwhile, the TDVP can perfectly follow the exact dynamics.

2.3 Dynamical simulation of NV centers ensemble

We model an ensemble of NV centers as a one-dimensional spin chain with long-range interactions. To incorporate dissipative effects into the quantum dynamics, we employ the Matrix Product Density Operator (MPDO) formalism for our simulations. We assume a uniform separation r between nearest-neighbor spins, i.e., $r_{i,i+1} = r$ for all $i = 1, 2, \ldots, N-1$. The spins are arranged linearly in the xy-plane, with positions given by $\vec{r}^{(i)} = r(i, i, 0)/\sqrt{2}$. Such one-dimensional arrangements are experimentally feasible, for example, through the fabrication of diamond nanopillars [49] or the use of nano-scale apertures during growth [4]. We investigate the strong interaction regime by setting the inter-spin separation r to the few-nanometer scale. For context, typical experiments with dense NV ensembles report average separations $r_{\text{avg}} \approx 10\,\text{nm}$ [54, 53], while minimum separations down to $r \sim 5\,\text{nm}$ have been achieved [21].

Unless specified otherwise, our simulations adhere to the following conditions:

1. The external magnetic field B_z is set such that the Zeeman splitting is $2g_s\mu_B B_z = 2\pi \times 407\,\text{MHz}$, matching the level splitting derived from fig. 2.3.
2. A constant and uniform microwave drive is applied resonantly to the $|0\rangle \leftrightarrow |-1\rangle$ transition, with Rabi frequency $\Omega = 2\pi \times 2.00\,\text{MHz}$ and driving frequency $\omega = D - g_s\mu_B B_z$.
3. All NV centers belong to the same orientation group, with their symmetry axes aligned parallel to the [111] crystallographic direction.
4. The simulation time step is $dt = 1\,\text{ns}$.
5. The system is initialized in the product state $|0\rangle^{\otimes N}$.

2.3.1 Bond truncation error

A primary source of error in simulations based on Matrix Product States (MPS) or MPDOs is the truncation error introduced by restricting the bond dimension to a maximum value, χ_{max}. When the number of Schmidt coefficients required to represent the state across a bond exceeds χ_{max}, the smallest coefficients are discarded. The error associated with a single bond truncation is quantified by the sum of the squares of the discarded singular values s_k:

$$\epsilon = \sqrt{\sum_{k>\chi_{\text{max}}} (s_k)^2}\,. \tag{2.14}$$

For systems exhibiting area-law entanglement scaling, such as those dominated by nearest-neighbor interactions, this error typically remains bounded during time evolution. In such cases, the required bond dimension grows slowly, allowing for efficient simulation of large systems with controlled errors. However, in our system featuring small separations, long-range interactions become significant. The entanglement structure of states evolving under long-range interactions generally does not adhere to an area law. Consequently, we investigate the impact of truncation errors in our MPDO simulations by comparing them against numerically exact results obtained via exact diagonalization (ED).

We first evaluate the truncation error for unitary evolution ($\gamma = 0$, corresponding to simulating a pure state) using the MPDO. Figures 2.9 and 2.10 compare MPDO simulations for $N = 4$ and $N = 7$ NV centers, respectively, with ED results for different maximum bond dimensions $\chi_{\max}$ and separations $r \in \{1.5, 2.0\}$ nm. Note that the ED results are obtained by simulating the pure state evolution for computational efficiency. As expected, stronger interactions (smaller r) lead to larger truncation errors for a fixed system size and $\chi_{\max}$. For $N = 4$, significant deviations from the ED results are observed when $\chi_{\max} < 64$, particularly for $\chi_{\max} = 16$ (figs. 2.9b and 2.9d). For the larger system size $N = 7$, substantial errors arise even with larger bond dimensions, especially at smaller separations (figs. 2.10c and 2.10d). Simulations using smaller $\chi_{\max}$ accurately reproduce the exact dynamics only for a limited time, until the entanglement growth necessitates a bond dimension exceeding $\chi_{\max}$. Beyond this point, truncation errors accumulate, causing the MPDO results to diverge from the exact solution.

These findings highlight that capturing the dynamics of strongly interacting long-range systems requires larger values of $\chi_{\max}$, thereby reducing the computational efficiency of MPS/MPDO methods compared to their application in short-range interacting systems.

2.3.2 Simulation with dissipation

We now introduce dissipation into the model by setting a uniform rate $\gamma_i = \gamma \neq 0$ for all spins i. Numerical values of γ are consistently given in units of $(\mu\text{s})^{-1}$. We model dissipation using local dephasing Lindblad operators, $\hat{L}_i = \sqrt{\gamma}\hat{S}_z^{(i)}$, acting independently on each spin. This form of dissipation is relevant, for instance, to noise originating from magnetic field fluctuations. In this scenario, dissipation is expected to counteract the entanglement growth driven by interactions, potentially limiting the required bond dimension during time evolution.

Figure 2.11 presents the absolute errors in the average magnetization for dissipative dynamics ($N = 4$), comparing MPDO simulations with ED results for various $\chi_{\max}$, separations r, and dephasing rates γ. The results demonstrate that, for a fixed $\chi_{\max}$, the simulation error is generally smaller in the presence of dissipation compared to the purely unitary case (cf. fig. 2.9). When dissipation (larger γ) limits the growth of entanglement across bipartitions, the MPDO representation requires smaller bond dimensions. Consequently, bond truncation becomes more effective, introducing smaller errors. This illustrates the interplay between interaction-driven entanglement growth and the suppressive effect of dissipation.

To further quantify the complexity of the MPDO representation and gain insight into entanglement dynamics, we calculate the Operator Entanglement Entropy (opEE). We compute the opEE of the reduced density matrix associated with a bipartition of the system at the central bond (connecting sites $\lfloor N/2 \rfloor$ and $\lfloor N/2 \rfloor + 1$). We employ the von Neumann entropy definition applied to the squared singular values $\{\lambda_i^2\}$ obtained from the Schmidt decomposition of the vectorized density operator $|\rho\rangle\rangle$ across this bond [28]:

$$S_{op} = -\sum_{i}^{\chi} (\lambda_i)^2 \log_2 (\lambda_i)^2 \,. \tag{2.15}$$

Here, λ_i are the singular values from the singular value decomposition (SVD) across the cutting bond for the MPDO tensor network representing a vectorized operator $|\rho\rangle$, and the sum runs up to the bond dimension χ. The squares λ_i^2 form a probability distribution related to the purity, $\sum_i \lambda_i^2 = \mathrm{Tr}(\rho^2)$.

Note that, in general, opEE does not directly quantify entanglement for mixed states in the same way von Neumann entropy does for pure states. However, for a pure state $\rho = |\psi\rangle\langle\psi|$, it can be shown (see eq. (1.161)) that the opEE is exactly twice the standard von Neumann entanglement entropy $S(|\psi\rangle)$ of the state vector $|\psi\rangle$:

$$S_{op}(|\rho\rangle\rangle) = 2S(|\psi\rangle) \,. \tag{2.16}$$

Thus, the opEE provides a measure related to entanglement growth and serves as a useful indicator of the representational complexity of the MPDO, which correlates with the potential for truncation errors [37].

The bond dimension is typically largest near the center of the chain. fig. 2.12 displays the time evolution of the opEE calculated across this central bond for systems of size $N = 4$ and $N = 7$. fig. 2.12a ($N = 4$) and fig. 2.12b ($N = 7$) show results for unitary evolution ($\gamma = 0$), while subfigures fig. 2.12c ($N = 4$) and fig. 2.12d ($N = 7$) illustrate the effect of dissipation ($\gamma > 0$). The plots reveal that the opEE growth rate increases with stronger interactions (smaller r). This observation is consistent with the earlier finding that stronger interactions lead to larger truncation errors for a fixed $\chi_{\max}$. Interestingly, for the strongest interaction considered ($r = 1.5\,\mathrm{nm}$) under unitary evolution, the opEE grows rapidly initially but then exhibits a temporary plateau or saturation behavior before potentially resuming growth (figs. 2.12a and 2.12b). As shown in figs. 2.12c and 2.12d, dissipation effectively suppresses the generation of opEE, with higher dissipation rates γ leading to lower saturation values.

We find that the saturation behavior observed in the opEE growth for the strong interaction regime ($r = 1.5\,\mathrm{nm}$) is sensitive to the Rabi frequency Ω. This behavior changes when the spins are driven with a larger Rabi frequency. fig. 2.13 shows the opEE dynamics for $N = 4$ up to $t = 0.2\,\mu\mathrm{s}$ when the Rabi frequency is doubled to $\Omega = 2\pi \times 4.00\,\mathrm{MHz}$. With the doubled Rabi frequency, the initial opEE growth is faster, reaching a higher peak value before exhibiting oscillations or decline around $t \approx 0.12\,\mu\mathrm{s}$ (fig. 2.13a). The effect of dissipation is also shown (fig. 2.13b). Further details regarding the influence of very small r will be discussed in section 2.4.2.

2.4 Entanglement Generation and QFI Dynamics

2.4.1 QFI calculation with MPDO

This section investigates the generation of entanglement among an ensemble of NV centers, driven by constant pulses and mediated by dipole-dipole interactions. Entanglement is a crucial resource for achieving quantum-enhanced probe sensitivity. We employ the Quantum Fisher Information (QFI) as a criterion to detect and quantify entanglement within the system.

As established in section 1.11.1, the maximum achievable QFI for an unentangled probe state in a noiseless magnetic field measurement scales linearly with the number of particles, N:

$$\max F_{\mathrm{prod}}(B_z, N) = N. \tag{2.17}$$

Conversely, for an entangled probe state, the maximum QFI can scale quadratically with N:

$$\max F_{\mathrm{ent}}(B_z, N) = N^2. \tag{2.18}$$

Therefore, based on this scaling difference, an entanglement criterion ξ^2 for a quantum state $\hat{\rho}$ can be defined as the ratio of its QFI, $F(\hat{\rho}, \hat{O})$, to the system size N [36]:

$$\xi^2 = \frac{F(\hat{\rho}, \hat{O})}{N}, \tag{2.19}$$

$$\text{where } 1 < \xi^2 \leq N \quad \text{indicates entanglement.} \tag{2.20}$$

Satisfying the condition $\xi^2 > 1$ violates the bound for product states given by eq. (2.17), thus certifying the presence of entanglement in the state $\hat{\rho}$. Specifically,

$\xi^2 > 1$ indicates the presence of partial, k-particle entangled state, for $k < N$. While values approaching the upper bound, $\xi^2 \approx N$, suggest maximal or near-maximal entanglement [9, 22].

To study the emergence of entanglement, we simulate the system's evolution using the Time-Dependent Variational Principle (TDVP) algorithm. The QFI dynamics are obtained by computing the QFI at each time step of the simulation using the tensor network methods. The method for calculating the QFI depends on the chosen tensor network representation. For Matrix Product Density Operators (MPDOs), which can represent general mixed states, the QFI is obtained by computing the optimal Symmetric Logarithmic Derivative (SLD) via a local optimization procedure (eqs. (1.211) and (1.215)). In contrast, for pure states represented by Matrix Product States (MPS), the QFI can be calculated more directly and efficiently from the variance of the relevant operator (eq. (1.178)). While the MPS approach is computationally less expensive, it is limited to pure states. The MPDO method offers generality for mixed states but introduces a potential downside: the local optimization for the SLD may converge to sub-optimal solutions (*false traps*) instead of the global optimum. To address this challenge, we implement a strategy involving multiple optimization repetitions initiated with different random SLDs, ultimately selecting the result that yields the highest QFI. A comparison of the QFI dynamics calculated using both methods for the same Hamiltonian is presented in section 2.4.1. The MPDO results shown were obtained using 10 optimization repetitions. As demonstrated in the figure and mentioned previously, the need to optimize the SLD can introduce numerical noise into the MPDO-based QFI calculation, whereas the MPS-based QFI closely tracks the results from exact diagonalization (ED). Therefore, the MPS approach should be employed whenever the system state remains pure, e.g. the dynamic are unitary, owing to its computational efficiency and accuracy. The MPDO method, despite its higher computational cost and potential for optimization-induced fluctuation, is essential when dealing with mixed states, such as those arising from dynamics involving dissipation or decoherence.

We simulated the short-time unitary dynamics (up to 200 ns) of $N = 2, 3, 4$ interacting NV centers under constant microwave driving using the MPDO representation, with results shown in fig. 2.15. The QFI was computed at each time step. To address the potential convergence of the SLD optimization to local minima, we performed 10 optimizations with random initializations at each step and selected the maximum QFI value. The resulting QFI dynamics exhibit significant fluctuations, particularly for larger N and higher Rabi frequencies. This behavior stems from the increasing complexity of the SLD optimization landscape, which raises the likelihood of trapping in local optima. We employed a heuristic strategy to partially mitigate this, using the optimized SLD from the preceding time step as one of initial guesses for the current one, which tends to yield smoother dynamics. For clearer visualization, the insets display a 10-step moving average of the QFI. As observed in the plots, systems with weaker interactions ($r = 4.0$,nm) generate QFI values approaching the maximum for separable states ($F_{\mathrm{prod},N} = N$, eq. (2.17)). The QFI generally increases over the simulation period as the NV separation decreases, corresponding to stronger interactions. Crucially, for separations $r \leq 2.5$,nm, the QFI surpasses the separable bound (eq. (2.17)), confirming the presence of interaction-induced entanglement. This entanglement is a key resource for enhancing the sensitivity of quantum probes in metrological tasks.

Dissipation, however, significantly degrades the achievable quantum-enhanced sensitivity. Figure 2.16 demonstrates this effect by simulating dynamics under dephasing ($\hat{c} = \hat{S}_z$ for all NVs). Unlike the unitary case, a non-zero dephasing rate γ causes a substantial reduction in the QFI at later times. In this specific simulation, entanglement generated after $t \approx 90$,ns is eliminated.

2.4.2 Effect from strong interaction

To obtain a clearer view of entanglement creation over longer time scales, we calculate the entanglement criterion ξ^2 defined in eq. (2.20) for the dynamics of interacting NVs up to $3\,\mu$s. We assign each NV center a principal axis index: $1 = [111], 2 = [\bar{1}11], 3 = [1\bar{1}1]$, and $4 = [11\bar{1}]$. These indices refer to the orientation of the NV center's principal axis relative to the diamond crystal structure. NV centers with parallel axes (e.g., index 1 and 1) experience stronger dipole-dipole interaction than those with non-parallel axes (e.g., index 1 and 2) at the same separation distance. The results are presented in fig. 2.17. Regions where $\xi^2 \leq 1$ (no certified entanglement) are colored grey, while other colors indicate varying degrees of entanglement ($\xi^2 > 1$). The plots show that entanglement is generated sooner (i.e., at shorter times) when the interaction is stronger. This is confirmed by comparing the ξ^2 values at the same separation r between systems containing NV centers with parallel versus non-parallel principal axes; parallel axes lead to faster entanglement generation. When increasing the system size to $N = 3$, the system becomes partially entangled (indicated by $\xi^2 > 1$) at approximately the same rate as for $N = 2$ under similar interaction strengths. However, the condition for maximal entanglement, $\xi^2 \approx N$, is not reached within the simulated time frame for $N = 3$. These results suggest that constant driving pulses are insufficient to achieve maximally entangled states in systems with $N > 2$ within practical timescales. Furthermore, generating entanglement faster, potentially before the onset of significant decoherence, likely requires replacing constant pulses with optimized control sequences. We explore this approach in section 2.5.

Notably, in both fig. 2.15 and fig. 2.17, we observe no entanglement generation for the case of $r = 1.0\,\mathrm{nm}$ with parallel axes, despite this configuration having the strongest interaction strength. This phenomenon is explained by the large interaction-induced energy level shift, ΔE_{int}, which causes significant detuning from the driving frequency ω. The shift ΔE_{int} can be estimated from the eigenvalues of the interaction Hamiltonian $\hat{H}_{int}$. Typically, this shift is considered negligible compared to the zero-field splitting D, and the driving frequency ω is set resonant with the unperturbed transition frequency (e.g., $\omega \approx \Delta_- = D - g_s \mu_B B_z$ for the $|0\rangle \leftrightarrow |-1\rangle$ transition, assuming B_z is the external field along the NV axis). However, at very close separations like $r = 1.0\,\mathrm{nm}$, an effect of the interaction-induced shift ΔE_{int} becomes significant, rendering the drive off-resonant. As demonstrated in fig. 2.18, the entanglement criterion ξ^2 for $r = 1.0\,\mathrm{nm}$ (parallel axes) is plotted as a function of a frequency shift $\omega_{\mathrm{shifted}}$, where the applied driving frequency is $\omega = \Delta_- + \omega_{\mathrm{shifted}}$. As expected, entanglement generation ($\xi^2 > 1$) is recovered when the frequency adjustment compensates for the interaction-induced shift, i.e., when $\omega_{\mathrm{shifted}} \approx \Delta E_{\mathrm{int}}$, bringing the drive back into resonance with the shifted energy levels.

2.5 Generate entanglement with optimal controls

Entanglement is a crucial resource for achieving quantum-enhanced sensitivity in spin-defect probes. As established previously, driving the probe with constant pulses proves inefficient for generating entanglement for $N > 2$ systems, particularly when aiming to prepare maximally entangled states within strict time constraints. This section addresses the optimal control problem of preparing entanglement between NV centers within the probe. We demonstrate that entanglement can be generated via the dipole-dipole interaction using optimal control fields. Furthermore, we utilize the quantum optimal control toolbox `QuOCS` [39] to solve this problem.

2.5.1 Control problem

We formulate the entanglement generation task as an optimal control problem. The objective is to find the time-dependent control fields, collectively denoted as $u(t)$, that maximize the objective function defined as a fidelity $F(u)$ with respect to a desired pure target state $|\phi_f\rangle$:

$$F(u) = F(\rho(t), \phi_f) = \langle\phi_f|\rho(t)|\phi_f\rangle, \tag{2.21}$$

where $\rho(t)$ is the system state at the time t. Equivalently, we can define a cost function to be minimized, corresponding to the infidelity: $F_{\text{cost}}(u) = 1 - F(u)$.

For a given total evolution time T, the initial state $\rho(0)$ evolves under the unitary operator $U(t)$, generated by the time-dependent total Hamiltonian $H(t)$. This Hamiltonian is the sum of a drift term $H_0(t)$ and a control term $H_{\text{ctrl}}(t)$:

$$H(t) = H_0(t) + H_{\text{ctrl}}(t). \tag{2.22}$$

The drift Hamiltonian $H_0(t)$, expressed in the rotating frame, describes the internal system dynamics, including the NV zero-field splittings, the Zeeman interaction, and the dipole-dipole interactions between NV centers:

$$H_0(t) = \sum_{i=1}^{N}((D - \omega_i)S_{z,i}^2 + B_{z,i}S_z) + \sum_{i\neq j} H_{\text{dip},(i,j)}, \tag{2.23}$$

where $H_{\text{dip}(i,j)}$ is the effective dipole-dipole interaction given by eq. (1.52). The control Hamiltonian $H_{\text{ctrl}}(t)$ describes the interaction with external microwave fields, represented by the time-dependent pulse functions $(u_x(t), u_y(t))$, which are the functions to be optimized:

$$H_{\text{ctrl}}(t) = \sum_{i}^{N} \left(u_{x,i}(t)S_{x,i} + u_{y,i}(t)S_{y,i}\right). \tag{2.24}$$

where $S_{x,i}$ and $S_{y,i}$ are spin operators acting only to i^{th} spin.

In summary, the goal is to find the optimal pulse functions $(u_x(t), u_y(t))$ that minimize the cost function $F_{\text{cost}}(u)$ (i.e., minimize the infidelity $1 - F(u)$) at the final time T, thereby driving the system from $\rho(0)$ to a state as close as possible to the target state $|\phi_f\rangle$.

2.5.2 dCRAB

The optimal control pulses $(u_x(t), u_y(t))$ are determined using the dressed Chopped Random Basis (dCRAB) algorithm [27, 38], as implemented in the Python-based quantum optimal control toolbox `QuOCS` [39]. This algorithm is a variant of the Chopped Random Basis (CRAB) method, a popular approach for quantum optimal control. By definition, the CRAB algorithm expands the control pulse $u(t)$ in terms of a finite set of N_c basis functions $u_i(t)$:

$$u(t) = \sum_{i=1}^{N_c} c_i u_i(t). \tag{2.25}$$

The optimization problem then reduces to finding the set of optimal coefficients c_i that minimize the cost function $F_{\text{cost}}(u)$. By choosing a finite number of basis functions N_c (i.e., "chopping" the basis), the dimension of the search space is reduced. For instance, choosing $N_c = 2$ restricts the search to a two-dimensional parameter space. A standard search algorithm, often a gradient-free method like the Nelder-Mead simplex algorithm [30], can then be employed to find the optimal coefficients c_i. The specific choice of algorithm is typically arbitrary within this class. Optionally, if an initial guess pulse $u_0(t)$ is available (which might not be representable by the chosen basis functions alone), it can be incorporated as a starting point, modifying the expansion as follows:

$$u(t) = u_0(t)(1 + \sum_{i=1}^{N_c} c_i u_i(t)). \tag{2.26}$$

However, using a fixed, chopped basis can cause the search algorithm to converge to a local minimum. To mitigate this, the CRAB algorithm employs randomly chosen basis functions to explore a broader search space. For instance, trigonometric basis functions like sine functions are commonly used:

$$u(t) = \Lambda(t) \sum_{i=1}^{N_c} c_i \sin(\omega_i t), \tag{2.27}$$

with frequencies ω_i typically chosen randomly within a range $[0, \omega_{\max}]$, where $\omega_{\max}$ is related to the experimental bandwidth. A possible choice is $\omega_i = \frac{\omega_{\max}}{N_c}(i + r_i + \frac{1}{2})$, where r_i are random numbers drawn from the interval $[-0.5, 0.5]$. Here, $\Lambda(t)$ is a smooth envelope or shape function ensuring the pulse amplitude starts and ends at zero. Its steepness parameter s, which can be set arbitrarily, determines how quickly the pulse ramps up and down. A common form for this function is:

$$\Lambda(t) = tanh(sin(\frac{\pi t}{2T})s)tanh(-sin(\frac{\pi(t-T)}{2T})s). \tag{2.28}$$

To further enhance the avoidance of local minima and explore the search space more effectively, the dressed CRAB (dCRAB) variant introduces an extra layer of iterative searches over different random bases. Each such search constitutes a "super-iteration". In dCRAB, after the optimizer converges during the $(j-1)$-th super-iteration, yielding pulse $u^{j-1}(t)$, a new set of random basis functions $u_i^j(t)$ is generated for the j-th super-iteration. The pulse $u^{j-1}(t)$ serves as the initial guess for this new stage. The pulse parametrization for the j-th super-iteration is:

$$u^j(t) = c_0^j u^{j-1}(t) + \sum_{i=1}^{N_c} c_i^j u_i^j(t), \tag{2.29}$$

and the final optimized pulse after a total of N_{SI} super-iterations is the sum of the optimized basis contributions from all super-iterations:

$$u_{\text{opt}}(t) = \sum_{j=1}^{N_{\text{SI}}} \sum_{i=1}^{N_c} c_i^{\text{opt},j} u_i^j(t). \tag{2.30}$$

Consequently, in each super-iteration, the optimization explores new directions defined by the coefficients $(c_1^j, \cdots, c_{N_c}^j)$ associated with the new random basis $u_i^j(t)$, while the coefficient c_0^j allows refinement along the direction of the previously optimized pulse $u^{j-1}(t)$. This "dressing" of the new search with the previous result helps navigate the optimization landscape more effectively.

2.5.3 GHZ state preparation

We now present the results for determining the optimal control pulses required to prepare entanglement among NV centers. In the simulations, the system is initialized in the product ground state $|0\rangle^{\otimes N}$. The target state is the N-particle GHZ state, which is maximally entangled. Specifically for the NV center's spin-1 basis, we define the target GHZ state involving the $|0\rangle$ and $|-1\rangle$ levels as:

$$|\text{GHZ}\rangle = \frac{1}{\sqrt{2}}(|0\rangle^{\otimes N} + |-1\rangle^{\otimes N}). \tag{2.31}$$

Over the time interval $[0, T]$, the control pulses $(u_x(t), u_y(t))$ are applied to the NV centers. The system evolves under the Hamiltonian given in eq. (2.22), which includes the dipole-dipole interactions between NVs. The time evolution is simulated using the Time-Dependent Variational Principle (TDVP) algorithm, detailed in section 1.8.2. Following the evolution up to the final time T, the fidelity $F(u)$ with respect to the target state $|\phi_f\rangle = |\text{GHZ}\rangle$ is calculated as the overlap $F(u) = \langle\phi_f|\rho(T)|\phi_f\rangle$, where $\rho(T)$ is the final state. This fidelity determines the cost function to be minimized: $F_{\text{cost}}(u) = 1 - F(u)$. The cost function is also referred to as the figure of merit (FOM). The minimization of the cost function is performed using the `QuOCS` toolbox, which optimizes the pulse parameters via the dCRAB method.

A schematic of this process is depicted in fig. 2.20.

Figure 2.21 shows the results of optimizing the control pulses to prepare the GHZ state for $N = 3$ NV centers, leveraging their strong dipole-dipole interaction. The initial state is $\rho_0 = |0\rangle\langle 0|^{\otimes 3}$. All NV centers have their principal axes aligned along the [111] direction and are positioned along a 1-dimensional chain in the xy-plane, with coordinates $\vec{r}_j = (j \cdot r, j \cdot r, 0)/\sqrt{2}$ for $j = 1, 2, 3$. The nearest-neighbor separation is set to $r = 2\,\mathrm{nm}$. Within each optimization step, the system's evolution under the control pulses $(u_x(t), u_y(t))$ is simulated for a total duration $T = 0.4\,\mu s$. The pulses were optimized over 1000 iterations using the dCRAB algorithm with the following settings:

1. Pulse basis: Sine functions ($N_c = 2$).
2. Number of super-iterations: $N_{\mathrm{SI}} = 5$.
3. Shape function (eq. (2.28)) steepness: $s = 30$.
4. Pulse amplitude constraint: $u_{x,y}(t) \in [-15, 15]\,\mathrm{MHz}$.
5. Amplitude variation parameter (dCRAB setting): 10.0.

Figure 2.21a illustrates the minimization of the cost function (FOM) over the optimization iterations. The observed spikes correspond to the basis randomization at the start of each super-iteration. Upon completion of the optimization, the final state ρ_f achieves a fidelity $F_{\mathrm{GHZ}} = \langle \mathrm{GHZ}|\rho_f|\mathrm{GHZ}\rangle = 0.987$. As shown by the state population histogram in fig. 2.21b, the final state is predominantly a superposition of the $|000\rangle$ and $|---\rangle$ components, with only small populations in other basis states. The corresponding optimal control pulses $(u_x(t), u_y(t))$ are displayed in fig. 2.22.

While optimizing pulses yielded successful results for the strongly interacting case ($r = 2\,\mathrm{nm}$), the optimization becomes more challenging when considering weaker, experimentally realistic interaction strengths. We performed an optimization using interaction parameters extracted from experimental measurements on a three-NV sample reported in [21]. The pairwise dipole-dipole interaction strengths were set to 53.0 kHz, 24.1 kHz, and 4.6 kHz, corresponding to approximate NV separations of 12.5 nm, 16.3 nm, and 28.2 nm, respectively. These interaction strengths are roughly two orders of magnitude weaker than the $\approx 6.5\,\mathrm{MHz}$ interaction strength considered for the $r = 2\,\mathrm{nm}$ separation. For this scenario, the pulse duration was set to $T = 2.0\,\mu s$. As shown in fig. 2.23, the optimization failed to prepare the target GHZ state with high fidelity within this timeframe. This suggests that generating significant entanglement via weaker dipole-dipole interactions requires longer evolution times. However, simulating longer evolution times substantially increases the computational cost, as maintaining numerical accuracy necessitates small time steps in the TDVP algorithm. Therefore, finding optimal control pulses for NV ensembles with realistic interaction strengths presents a significant computational challenge due to the required longer simulation times.

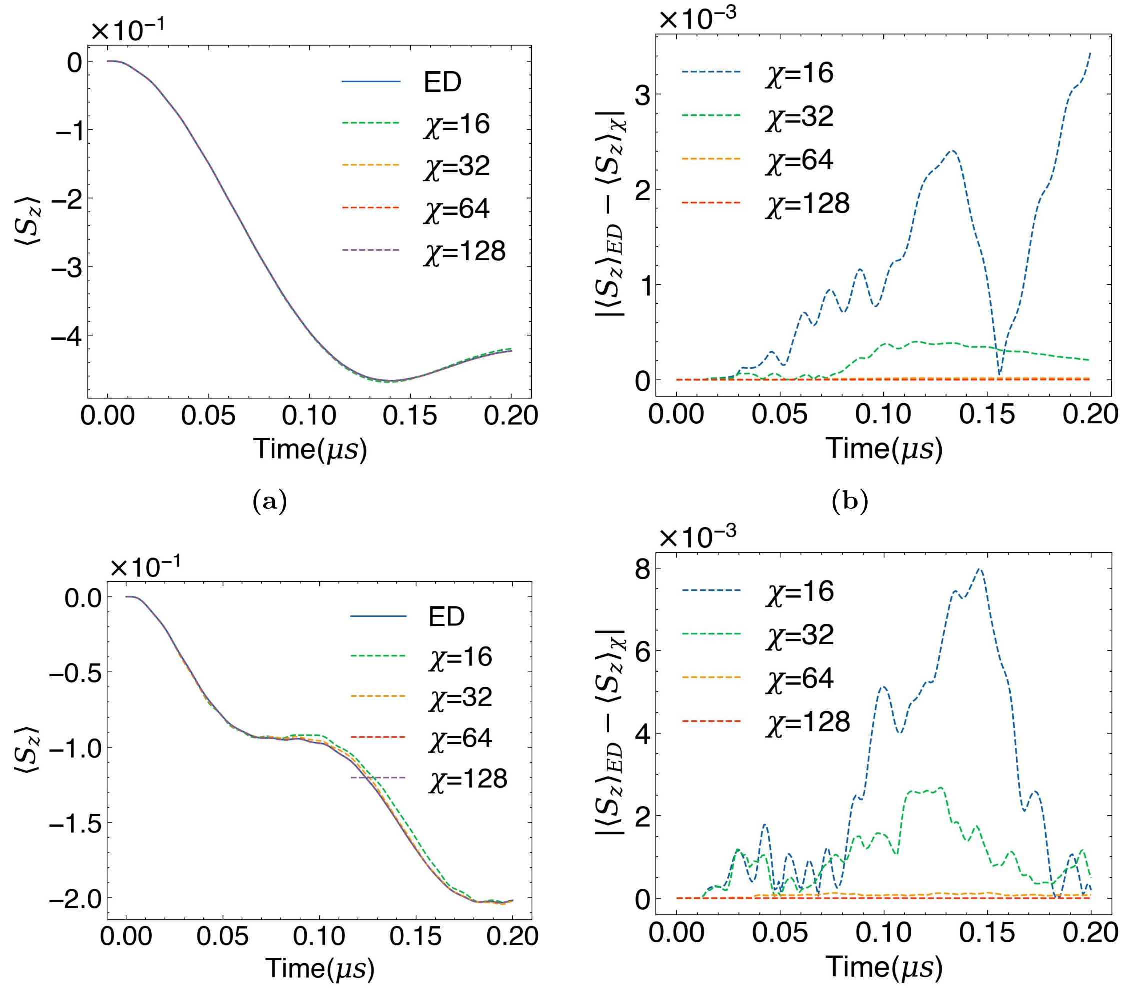

(a)

(b)

(c)

(d)

Figure 2.9: Unitary evolution ($\gamma = 0$) of $N = 4$ NV centers. (a, c) Average magnetization $\langle S_z \rangle = \frac{1}{N} \sum_i \langle S_z^{(i)} \rangle$ versus time, comparing MPDO simulations with varying $\chi_{\max}$ to exact diagonalization (ED). (b, d) Absolute error in average magnetization, $|\langle S_z \rangle_{\mathrm{MPDO}} - \langle S_z \rangle_{\mathrm{ED}}|$, for the simulation time ($t = 0.2\,\mu$s) as a function of $\chi_{\max}$. Top row (a, b): $r = 2.0\,$nm. Bottom row (c, d): $r = 1.5\,$nm.

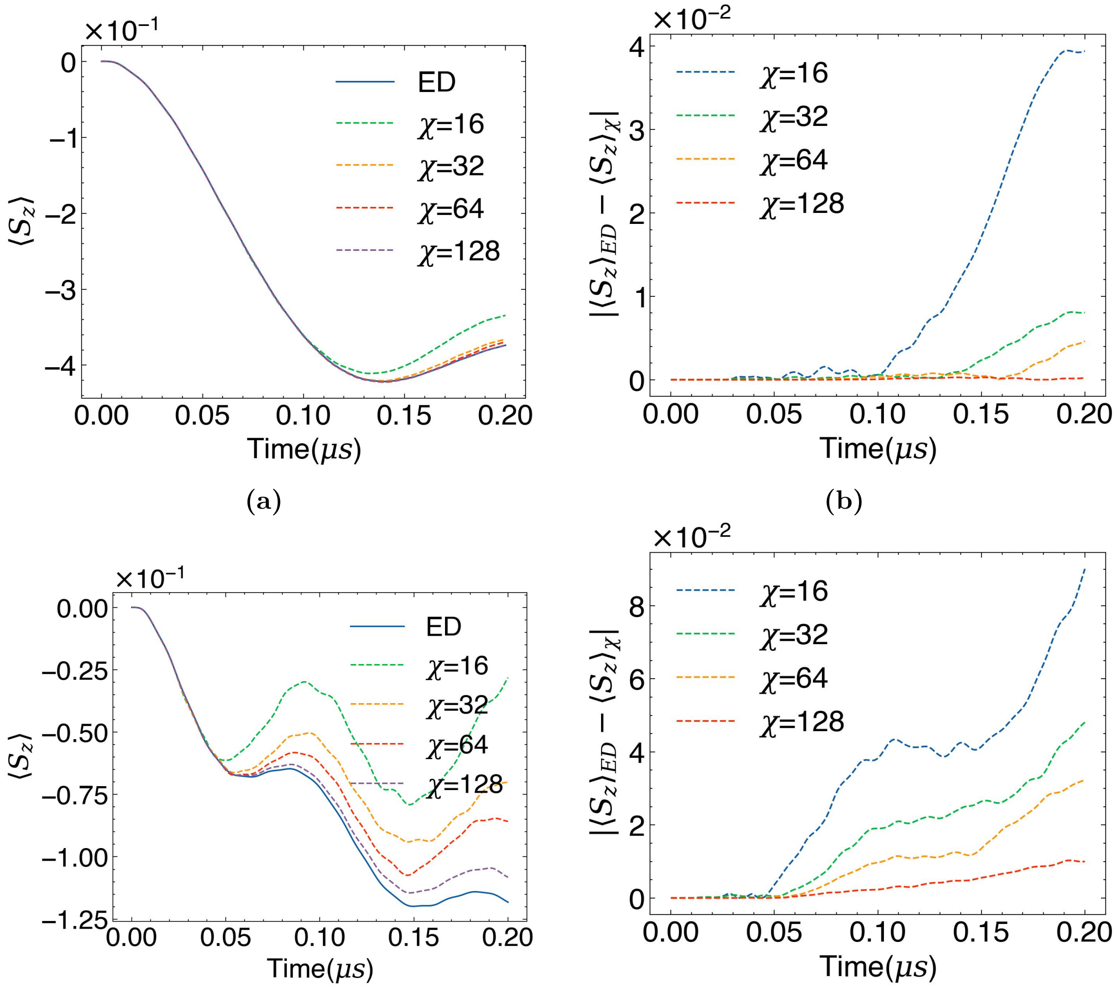

(a) **(b)**

(c) **(d)**

Figure 2.10: Unitary evolution ($\gamma = 0$) of $N = 7$ NV centers. (a, c) Average magnetization $\langle S_z \rangle$ versus time, comparing MPDO simulations with varying $\chi_{\max}$ to exact diagonalization (ED). (b, d) Absolute error in average magnetization for the simulation time ($t = 0.2\,\mu$s) as a function of $\chi_{\max}$. Top row (a, b): $r = 2.0\,$nm. Bottom row (c, d): $r = 1.5\,$nm.

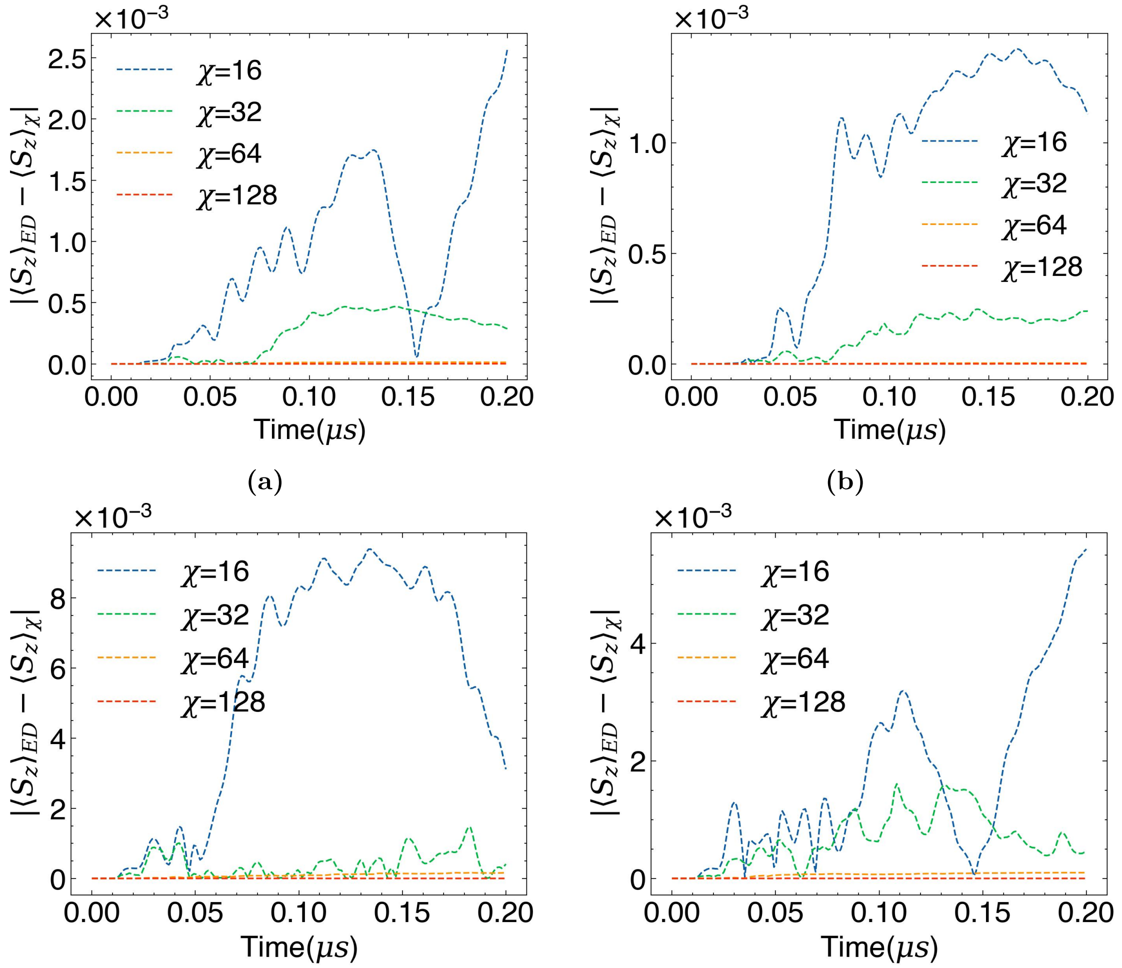

(a) **(b)**

(c) **(d)**

Figure 2.11: Numerical errors in MPDO simulations of dissipative dynamics for $N = 4$ NV centers, compared to exact diagonalization. Plots show the absolute error in average magnetization, $|\langle S_z\rangle_{\mathrm{MPDO}} - \langle S_z\rangle_{\mathrm{ED}}|$, for the simulation time ($t = 0.2\,\mu\mathrm{s}$) as a function of $\chi_{\max}$. Dephasing operator $\hat{L}_i = \sqrt{\gamma}\hat{S}_z^{(i)}$. (a) $r = 2.0\,\mathrm{nm}$, $\gamma = 1.0\,(\mu\mathrm{s})^{-1}$. (b) $r = 2.0\,\mathrm{nm}$, $\gamma = 5.0\,(\mu\mathrm{s})^{-1}$. (c) $r = 1.5\,\mathrm{nm}$, $\gamma = 1.0\,(\mu\mathrm{s})^{-1}$. (d) $r = 1.5\,\mathrm{nm}$, $\gamma = 5.0\,(\mu\mathrm{s})^{-1}$.

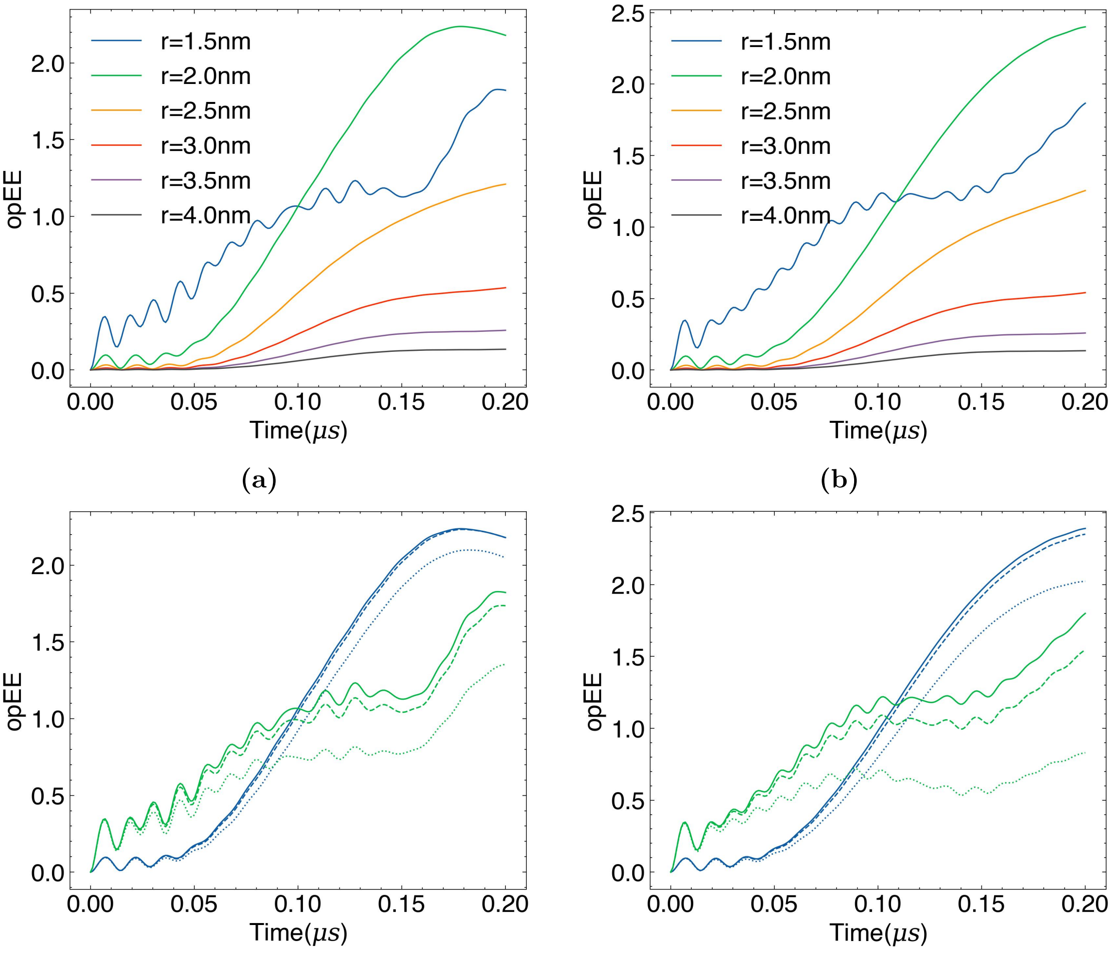

(a) **(b)**

(c) **(d)**

Figure 2.12: Operator Entanglement Entropy (opEE, eq. (2.15)) across the central bond as a function of time. (a) $N = 4$, unitary evolution ($\gamma = 0$). (b) $N = 7$, unitary evolution ($\gamma = 0$). Line colors indicate separation r. (c) $N = 4$, dissipative evolution. (d) $N = 7$, dissipative evolution. Line colors indicate separation r (Green: $r = 1.5\,\mathrm{nm}$, Blue: $r = 2.0\,\mathrm{nm}$), and line styles indicate dissipation rate γ (solid: $\gamma = 0.0$, dashed: $\gamma = 1.0\,(\mu\mathrm{s})^{-1}$, dotted: $\gamma = 5.0\,(\mu\mathrm{s})^{-1}$).

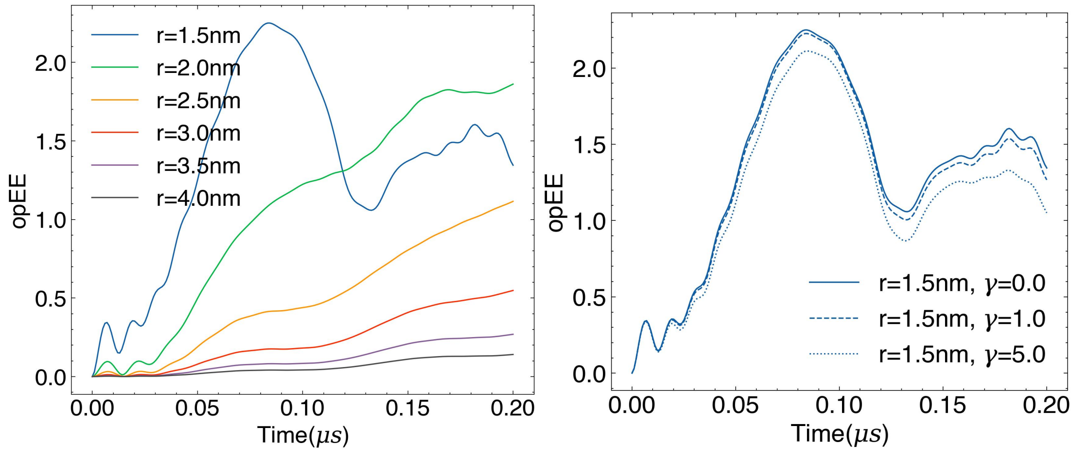

(a) **(b)**

Figure 2.13: Effect of doubled Rabi frequency ($\Omega = 2\pi \times 4.00\,\mathrm{MHz}$) on Operator Entanglement Entropy (opEE) across the central bond for $N = 4$. (a) Unitary evolution ($\gamma = 0$). (b) Dissipative evolution with $\gamma = 1.0, 5.0\,(\mu\mathrm{s})^{-1}$. Line colors indicate separation r (Green: $r = 1.5\,\mathrm{nm}$, Blue: $r = 2.0\,\mathrm{nm}$).

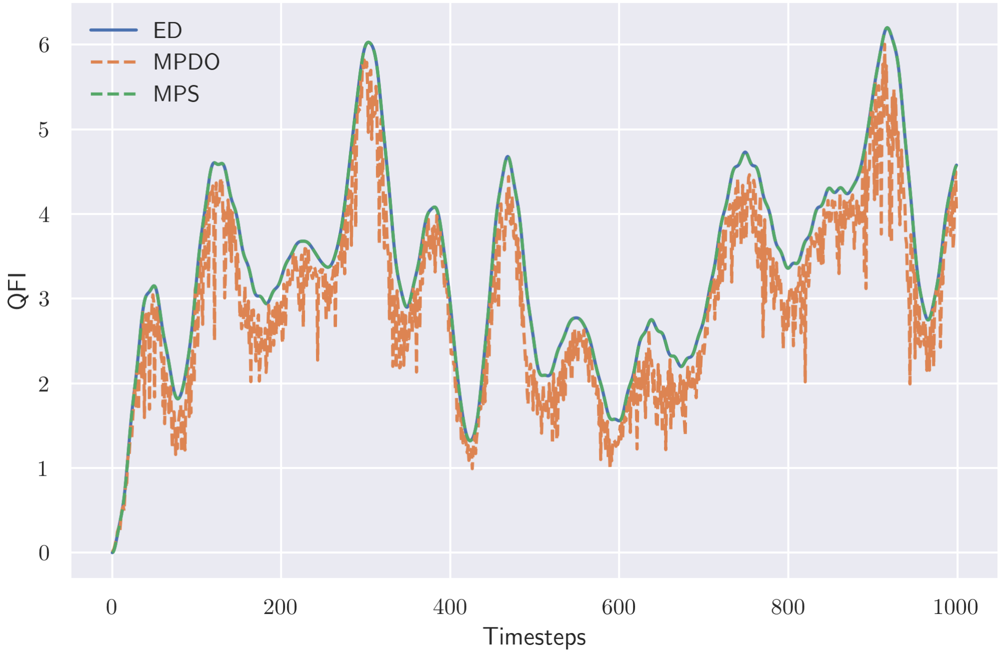

Figure 2.14: Comparison of Quantum Fisher Information (QFI) dynamics calculated using Matrix Product State (MPS) and Matrix Product Density Operator (MPDO) representations for the same Hamiltonian. The optimization required to find the Symmetric Logarithmic Derivative (SLD) for the MPDO approach can introduce numerical fluctuation, leading to less smooth results compared to the MPS calculation, which shows excellent agreement with exact diagonalization (ED).

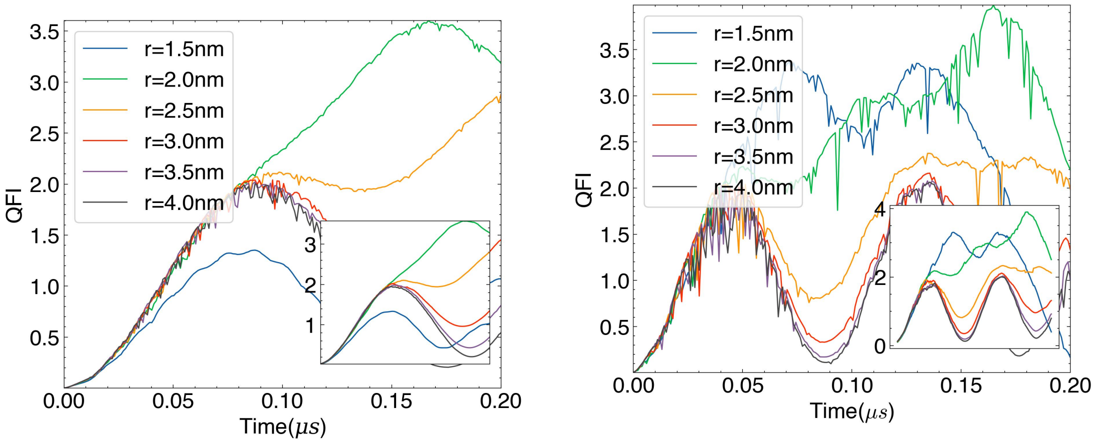

(a) $N = 2$, $\Omega = (2\pi)2\text{MHz}$

(d) $N = 2$, $\Omega = (2\pi)4\text{MHz}$

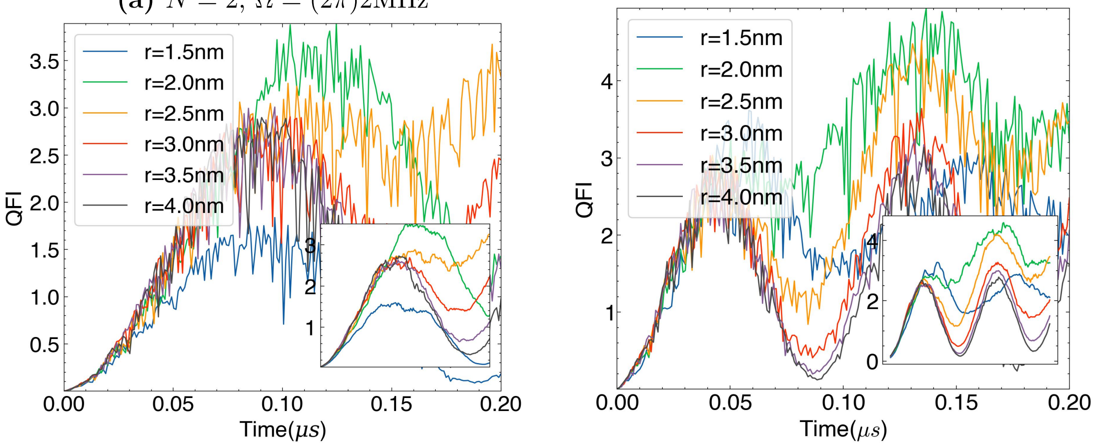

(b) $N = 3$, $\Omega = (2\pi)2\text{MHz}$

(e) $N = 3$, $\Omega = (2\pi)4\text{MHz}$

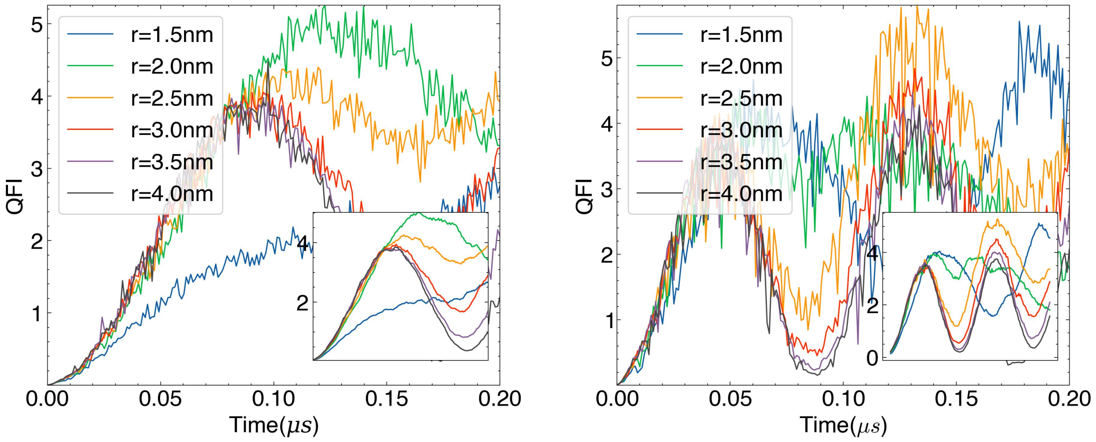

(c) $N = 4$, $\Omega = (2\pi)2\text{MHz}$

(f) $N = 4$, $\Omega = (2\pi)4\text{MHz}$

Figure 2.15: QFI dynamics for $N = 2, 3, 4$ NV centers calculated using the MPDO representation for various NV separations r (indicated by color) and two Rabi frequencies Ω. Each point represents the maximum QFI obtained from 10 SLD optimization initializations. The insets show the corresponding 10-step moving average of the QFI to reduce noise visualization.

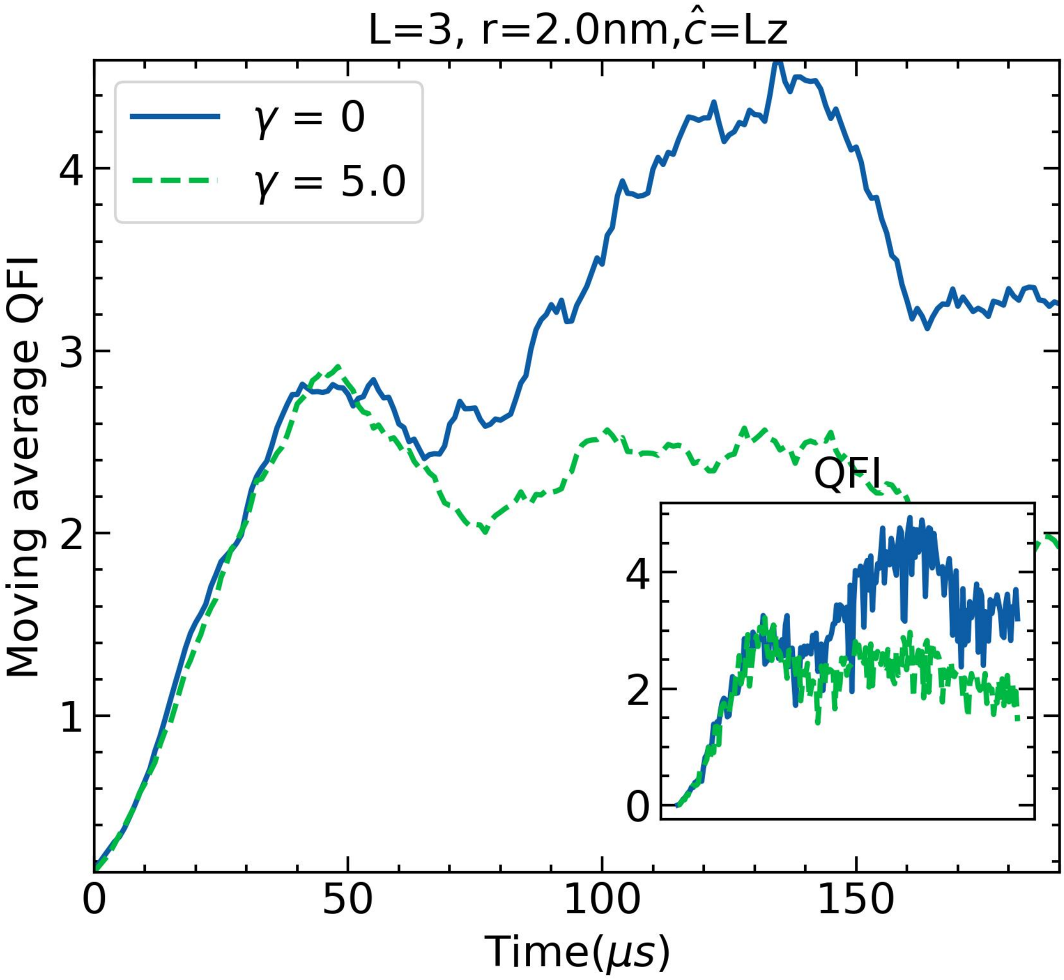

Figure 2.16: Comparison of QFI dynamics for $N = 3$ NVs with separation $r = 2.0\,\mathrm{nm}$ under unitary evolution (blue) versus evolution with dephasing ($\hat{c} = \hat{S}_z$, green). Dissipation, modeled with a dephasing rate $\gamma = 5.0\,\mathrm{MHz}$, significantly suppresses the QFI generated by the interaction, particularly at later times.

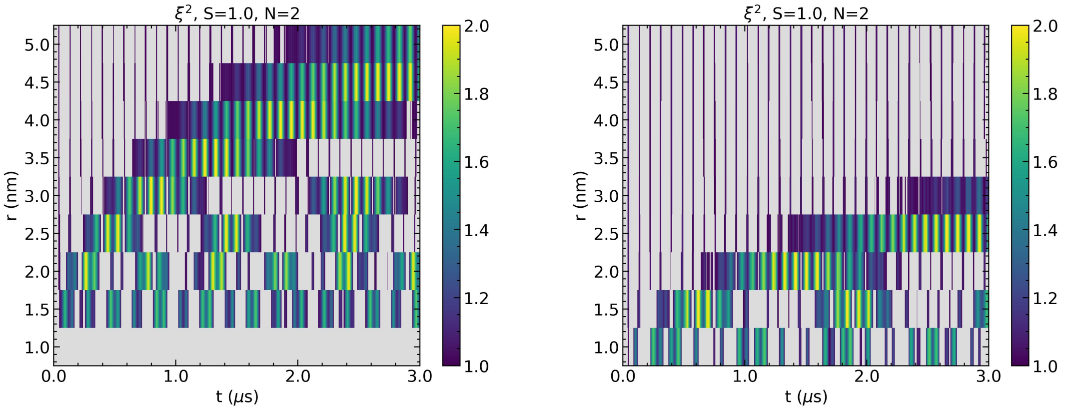

(a) $N = 2$ with principal axis index $(1, 1)$.   **(c)** $N = 2$ with principal axis index $(1, 2)$.

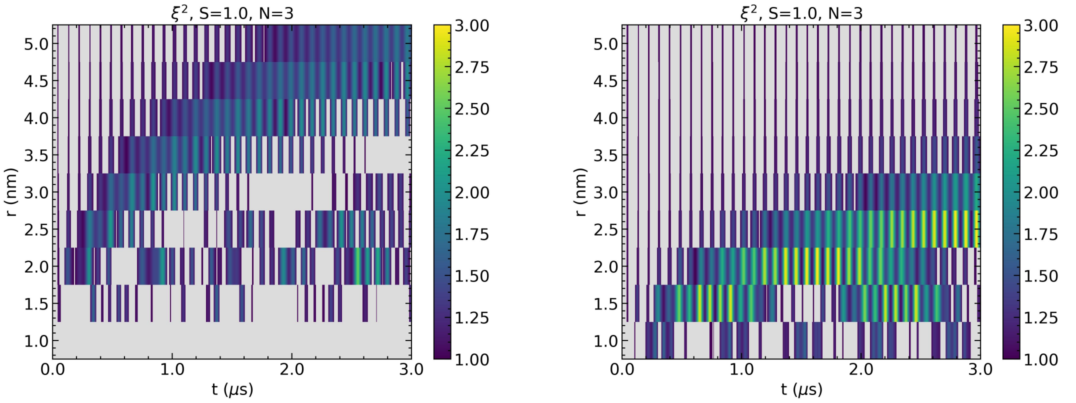

(b) $N = 3$ with principal axis index $(1, 1, 1)$.   **(d)** $N = 3$ with principal axis index $(1, 2, 1)$.

Figure 2.17: Entanglement criterion $\xi^2 = F_Q/N$ over time as a function of NV separation r for $N = 2$ and $N = 3$ systems with different principal axis orientations. Colored regions indicate $\xi^2 > 1$, signifying entanglement. Parallel axes lead to stronger interactions and faster entanglement generation compared to non-parallel axes at the same r. $\Omega = (2\pi)2\,\mathrm{MHz}$.

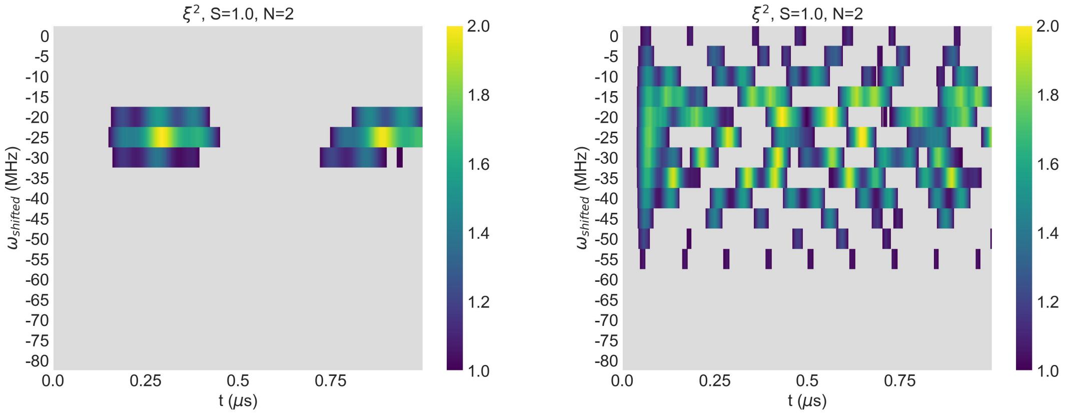

(a) $\Omega = (2\pi)2\text{MHz}$, $\Delta E_{\text{int}} = -26.01\text{MHz}$. **(c)** $\Omega = (2\pi)4\text{MHz}$, $\Delta E_{\text{int}} = -26.01\text{MHz}$.

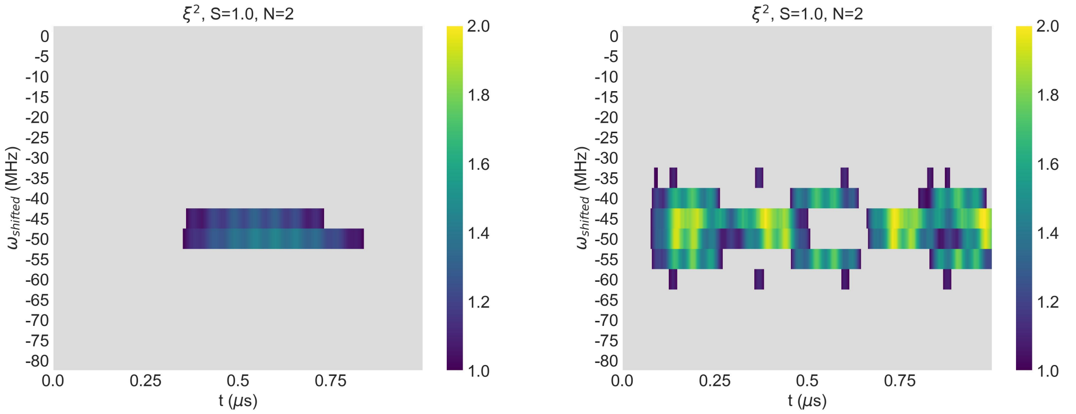

(b) $\Omega = (2\pi)2\text{MHz}$, $\Delta E_{\text{int}} = -52.00\text{MHz}$. **(d)** $\Omega = (2\pi)4\text{MHz}$, $\Delta E_{\text{int}} = -52.00\text{MHz}$.

Figure 2.18: Entanglement criterion ξ^2 for two NV centers with parallel axes at $r = 1.0\,\text{nm}$, plotted as a function of the driving frequency shift ω_{shifted}. Entanglement generation ($\xi^2 > 1$, colored regions) is suppressed when $\omega_{\text{shifted}} = 0$ (drive resonant with unperturbed levels) but is recovered when ω_{shifted} compensates for the interaction-induced energy shift ΔE_{int}.

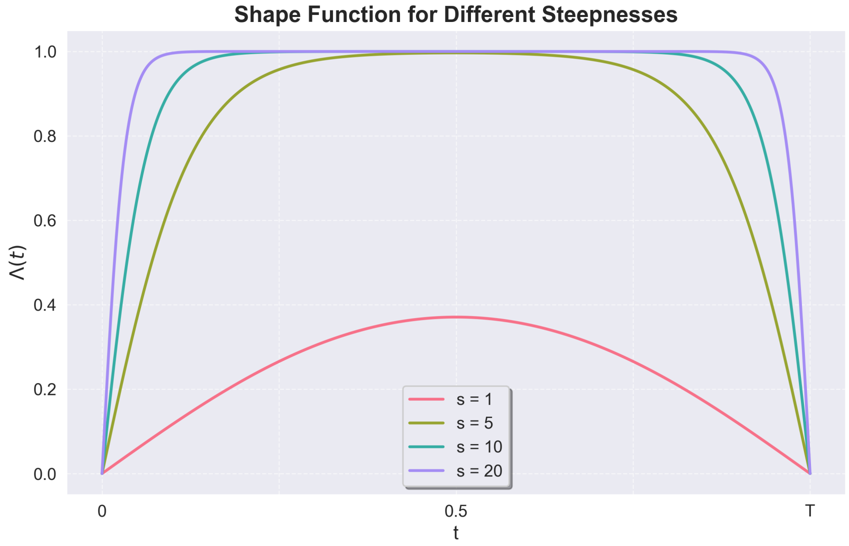

Figure 2.19: A shape function as defined in eq. (2.28) with different steepness parameters s.

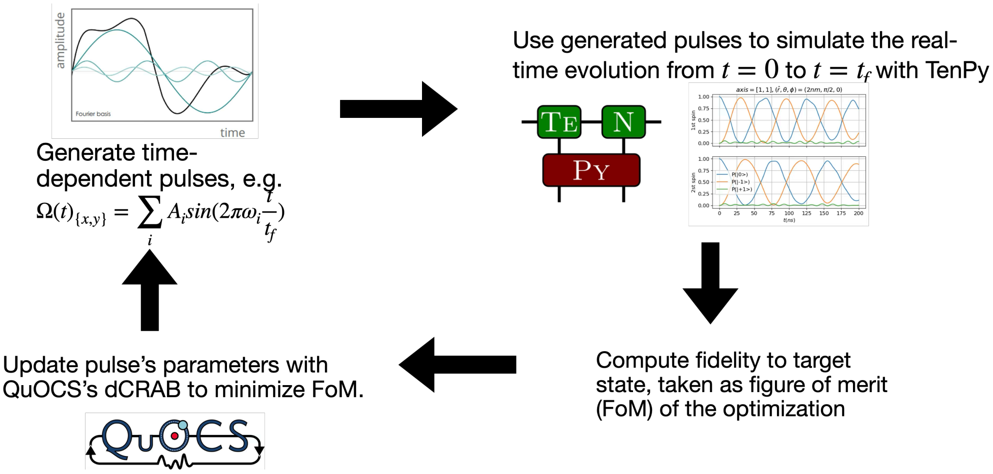

Figure 2.20: Diagram illustrating the integration of the tensor network dynamical simulation within the pulse optimization loop.

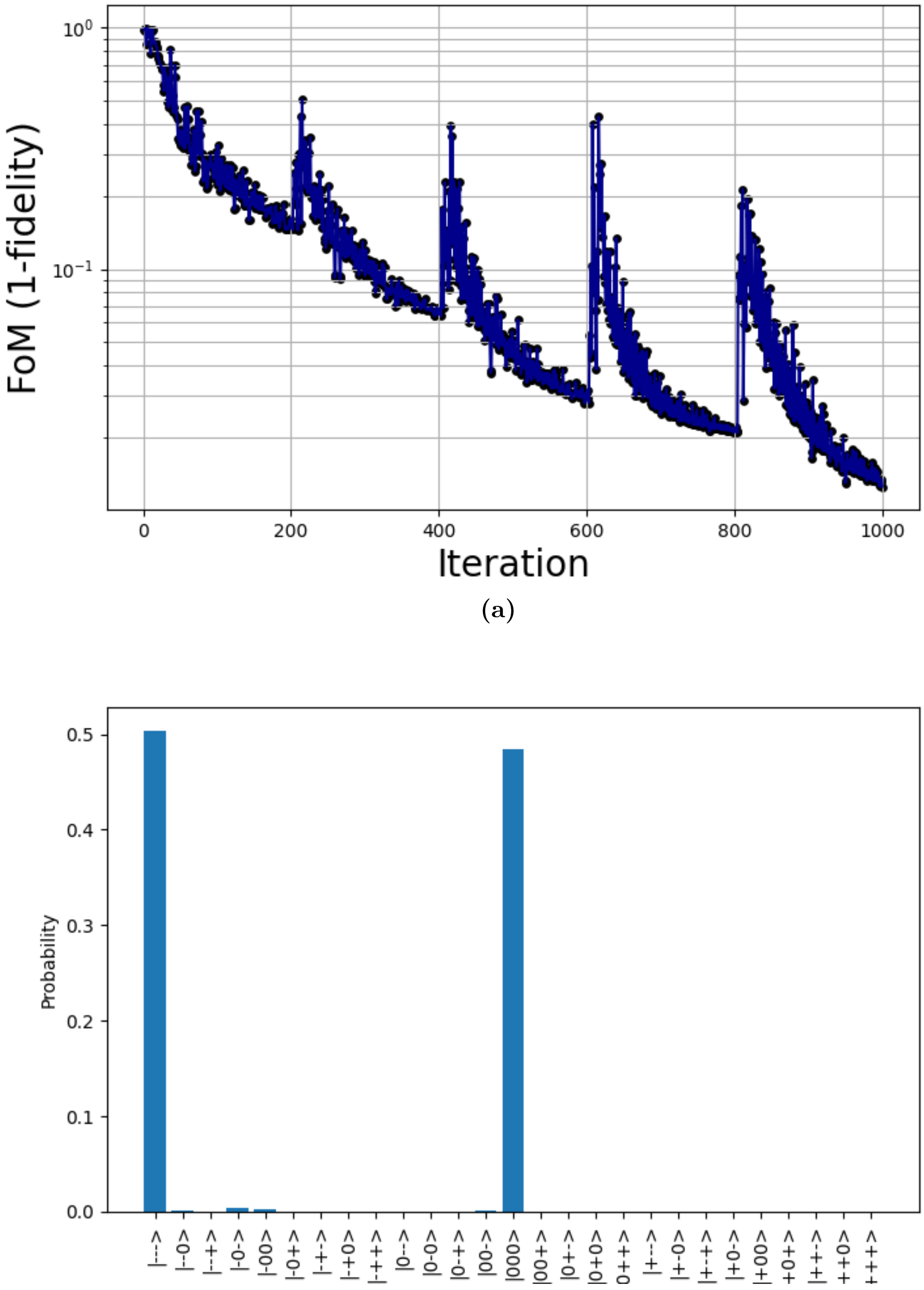

(a)

(b)

Figure 2.21: The pulse optimization to prepare NV centers in the GHZ state for $N = 3$, $r = 2\,\text{nm}$. All NV's principal axes are aligned along the [111] direction. (a): Figure of merit (cost function) as a function of iteration. The cost function is defined as $F_{\text{cost}}(u) = 1 - F(u)$, where $F(u)$ is the fidelity to the target state. (b): The probability distribution of the final state. The histogram shows that the final state is close to the target state, indicating that the optimization was successful.

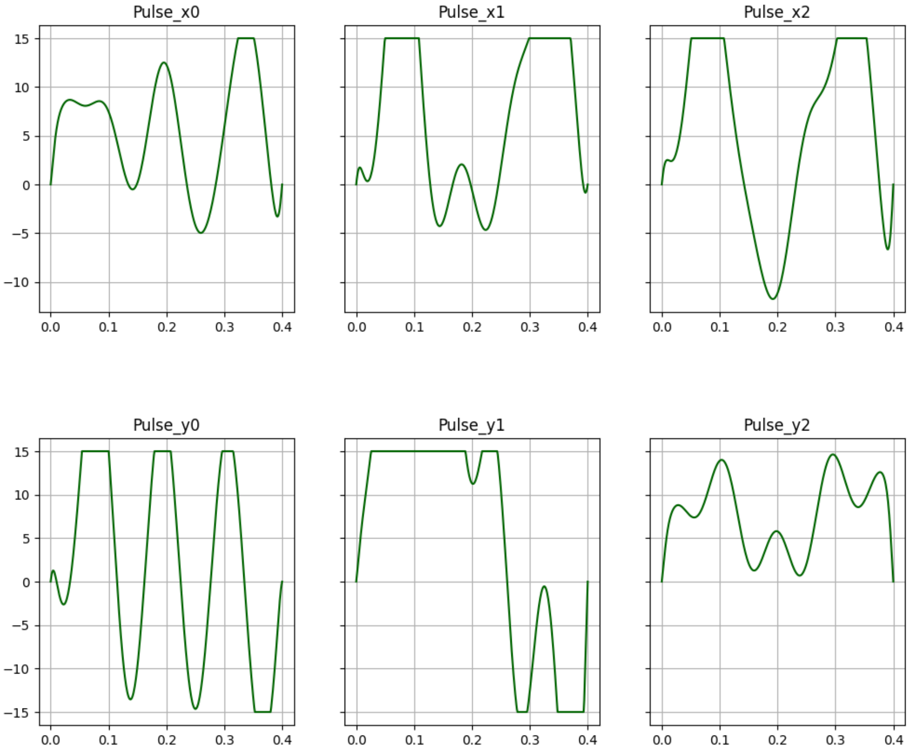

Figure 2.22: The optimal control pulses $(u_x(t), u_y(t))$ to prepare NV centers in the GHZ state for $N = 3$, $r = 2\,\mathrm{nm}$. All NV's principal axes are aligned along the [111] direction.

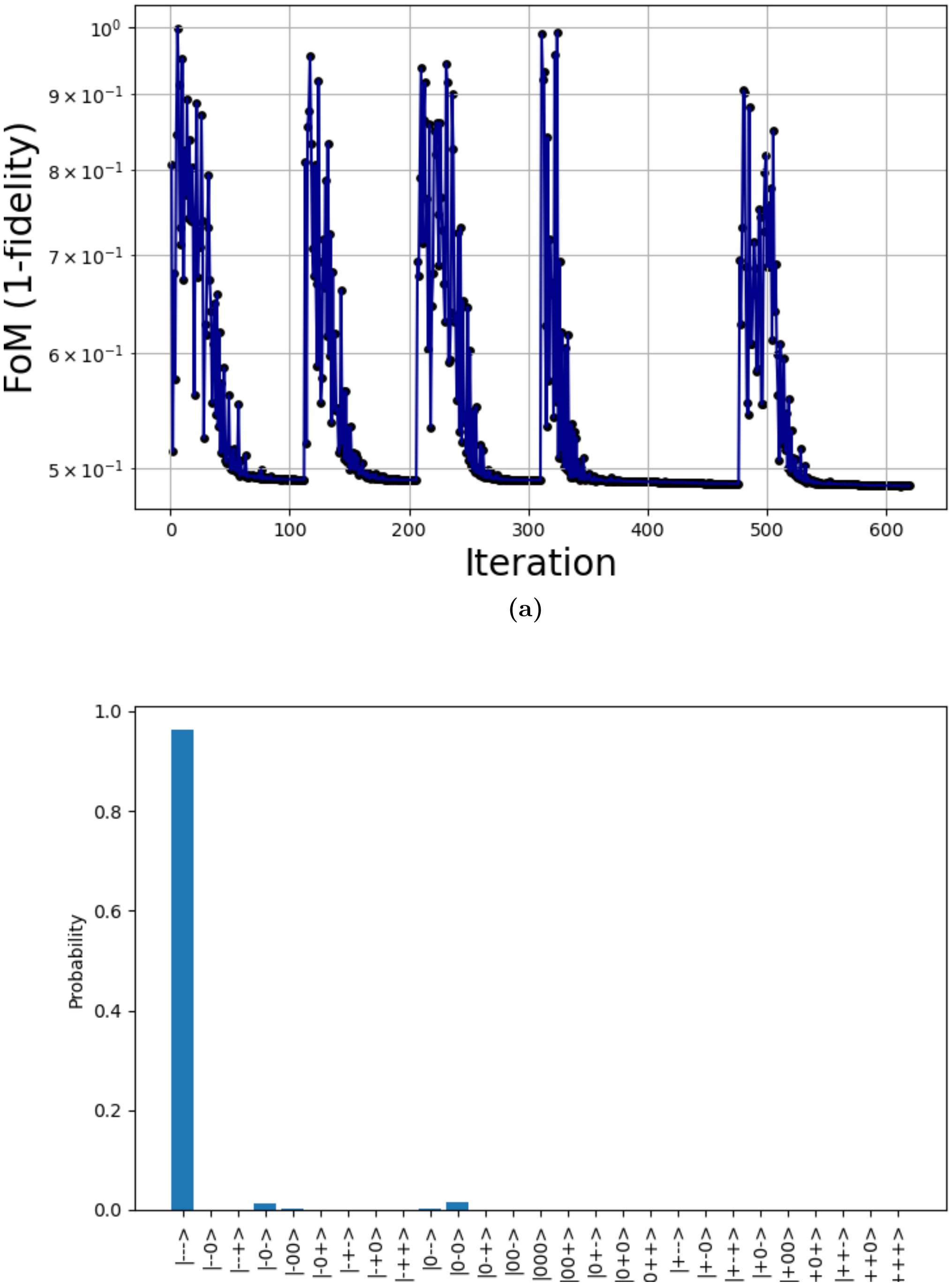

(a)

(b)

Figure 2.23: The pulse optimization to prepare NV centers in the GHZ state for $N = 3$, The interaction strengths are obtained from actual sample in an experiment. (a): Figure of merit (cost function) as a function of iteration. The cost function is defined as $F_{\text{cost}}(u) = 1 - F(u)$, where $F(u)$ is the fidelity to the target state. (b): The probability distribution of the final state. The histogram shows that the final state is close to the target state, indicating that the optimization was successful.

Chapter 3

Conclusion and Outlook

Dense ensembles of Nitrogen-Vacancy (NV) centers represent a significant platform for quantum metrology, offering potential sensitivity enhancements derived from inter-NV interactions. This thesis focused on developing and applying tensor network (TN) methods to simulate the dissipative temporal dynamics of such strongly interacting NV center ensembles. Addressing the computational limitations inherent in exact diagonalization for large system sizes, we modeled the strongly interacting dense ensemble using a one-dimensional tensor network representation incorporating long-range interactions. To account for dissipation, mixed quantum states were represented using the Matrix Product Density Operator (MPDO) formalism, an extension of the Matrix Product State (MPS) framework suitable for density matrices.

We investigated two tensor network time-evolution algorithms capable of handling the long-range Hamiltonian: i) the W^{II} Matrix Product Operator (MPO) method and ii) the time-dependent variational principle (TDVP). The reliability and accuracy of these algorithms for solving the Lindblad master equation using MPDOs in the strong interaction regime were systematically compared. While TDVP exhibited lower computational efficiency for small system sizes, its time complexity scaling became comparable to the W^{II} MPO method for larger systems. However, the W^{II} MPO method was observed to produce unphysical results for certain observables due to numerical divergences. In contrast, TDVP demonstrated superior numerical stability, evidenced by significantly smaller errors in the imaginary components of calculated expectation values, indicating better preservation of hermiticity. These findings led us to conclude that TDVP is the more reliable algorithm within the parameter regimes relevant to this work. Furthermore, we assessed the impact of the finite maximum bond dimension (χ) by comparing the average magnetization calculated via MPDO against exact diagonalization.

The results confirmed that stronger interactions require larger bond dimensions to maintain accuracy, as increased entanglement leads to larger truncation errors. Notably, the inclusion of dissipation was shown to suppress entanglement entropy growth, thereby, for the smae bond dimension, enhancing the accuracy achievable for a given computational cost. This highlights the suitability of TN methods, particularly MPDOs, for simulating open quantum systems.

Turning to applications in quantum sensing, we calculated the Quantum Fisher Information (QFI) of the evolving quantum state to quantify the metrological potential. The QFI was computed by variationally approximating the Symmetric Logarithmic Derivative (SLD) as an MPO, where local tensors were optimized iteratively via a sweeping procedure. As the QFI establishes the ultimate achievable sensitivity bound, optimized over all possible POVM measurements and unbiased estimators, it serves as a crucial metric for assessing sensitivity improvements and the role of entanglement. While sensitivity scales linearly with the number of independent spins (Standard Quantum Limit, SQL), interactions can generate entanglement, potentially enabling sensitivity beyond this limit. Our results for driven ensembles demonstrated that strong interactions indeed lead to QFI values exceeding the SQL, confirming entanglement-enhanced sensitivity. Additionally, we observed that for very strong interactions, the effectiveness of constant microwave driving pulses in generating useful entanglement can be diminished. This occurs because interaction-induced energy level shifts can detune the spins significantly from the driving field resonance. In such regimes, altering microwave parameters, such as intensities or Rabi frequencies, is necessary to optimize sensitivity.

Finally, we employed optimal control techniques to explore the maximization of the probe's sensitivity through targeted state preparation. While constant pulses can generate partial entanglement, reaching the fundamental Heisenberg limit often requires dynamically shaped pulses. We successfully demonstrated this by optimizing pulse shapes over a finite evolution time to prepare a three-NV center state with high fidelity to the Greenberger-Horne-Zeilinger (GHZ) state, a canonical resource for quantum-enhanced metrology.

Despite the theoretical possibility of maximizing entanglement with strong interactions using optimal control, translating these findings into experimental practice remains challenging. A primary difficulty arises because typical coupling strengths in experimental samples are considerably weaker than those often assumed in simulations favouring rapid entanglement generation. Consequently, longer pulse durations are required to achieve significant entanglement enhancement in realistic systems. Computationally, simulating these long evolutions accurately demands small time steps to control numerical errors, particularly with variational methods like TDVP. This combination significantly increases the simulation time required for each iteration within an optimal control loop. Considering these constraints, it remains an open question whether optimal pulses for realistic experimental parameters can be found within a feasible computational timeframe. Addressing this scalability challenge is an important direction for future research.

Bibliography

[1] Priyadharshini Balasubramanian et al. “dc Magnetometry with Engineered Nitrogen-Vacancy Spin Ensembles in Diamond”. In: *Nano Lett.* 19.9 (Sept. 2019). Publisher: American Chemical Society, pp. 6681–6686. ISSN: 1530-6984. DOI: `10.1021/acs.nanolett.9b02993`. URL: `https://doi.org/10.1021/acs.nanolett.9b02993`.

[2] Erik Bauch et al. “Decoherence of ensembles of nitrogen-vacancy centers in diamond”. In: *PHYSICAL REVIEW B* 102 (2020), p. 134210. DOI: `10.1103/PhysRevB.102.134210`.

[3] Daniel Bauernfeind, Markus Aichhorn, and Hans Gerd Evertz. *Comparison of MPS based real time evolution algorithms for Anderson Impurity Models*. arXiv:1906.09077 [cond-mat]. June 2019. DOI: `10.48550/arXiv.1906.09077`. URL: `http://arxiv.org/abs/1906.09077`.

[4] Igal Bayn et al. “Generation of Ensembles of Individually Resolvable Nitrogen Vacancies Using Nanometer-Scale Apertures in Ultrahigh-Aspect Ratio Planar Implantation Masks”. In: *Nano Letters* 15.3 (Mar. 2015). Publisher: American Chemical Society, pp. 1751–1758. ISSN: 1530-6984. DOI: `10.1021/nl504441m`. URL: `https://doi.org/10.1021/nl504441m`.

[5] Alberto Giuseppe Catalano. *Numerically efficient unitary evolution for Hamiltonians beyond nearest-neighbors*. arXiv:2402.05198 [cond-mat]. Feb. 2024. DOI: `10.48550/arXiv.2402.05198`. URL: `http://arxiv.org/abs/2402.05198`.

[6] Krzysztof Chabuda et al. “Tensor-network approach for quantum metrology in many-body quantum systems”. en. In: *Nature Communications* 11.1 (Jan. 2020). Number: 1 Publisher: Nature Publishing Group, p. 250. ISSN: 2041-1723. DOI: `10.1038/s41467-019-13735-9`. URL: `https://www.nature.com/articles/s41467-019-13735-9`.

[7] Chen Cheng. “Many-body localization in clean chains with long-range interactions”. In: *Phys. Rev. B* 108 (15 Oct. 2023), p. 155113. DOI: `10.1103/`

PhysRevB.108.155113. URL: https://link.aps.org/doi/10.1103/PhysRevB.108.155113.

[8] Thomas L. Curtright, David B. Fairlie, and Cosmas K. Zachos. "A Compact Formula for Rotations as Spin Matrix Polynomials". en. In: *SIGMA. Symmetry, Integrability and Geometry: Methods and Applications* 10 (Aug. 2014). Publisher: SIGMA. Symmetry, Integrability and Geometry: Methods and Applications, p. 084. ISSN: 18150659. DOI: 10.3842/SIGMA.2014.084. URL: http://www.emis.de/journals/SIGMA/2014/084/.

[9] Federico Dell'Anna et al. "Quantum Fisher information and multipartite entanglement in spin-1 chains". In: *Physical Review B* 108.14 (Oct. 2023). Publisher: American Physical Society, p. 144414. DOI: 10.1103/PhysRevB.108.144414. URL: https://link.aps.org/doi/10.1103/PhysRevB.108.144414.

[10] "Diamond nitrogen-vacancy center charge state ratio determination at a given sample point". en-US. In: *Journal of Luminescence* 248 (Aug. 2022). Publisher: North-Holland, p. 118981. ISSN: 0022-2313. DOI: 10.1016/j.jlumin.2022.118981. URL: https://www.sciencedirect.com/science/article/abs/pii/S0022231322002563.

[11] Bo L. Dwyer et al. "Probing Spin Dynamics on Diamond Surfaces Using a Single Quantum Sensor". In: *PRX Quantum* 3 (4 Dec. 2022), p. 040328. DOI: 10.1103/PRXQuantum.3.040328. URL: https://link.aps.org/doi/10.1103/PRXQuantum.3.040328.

[12] Simon Essink. "Boundary-Driven XXZ Spin-1/2 Chain". PhD thesis. Bonn: Universität Bonn, 2018. URL: https://www.pi.uni-bonn.de/kollath/en/publications/thesis_essink_final_version.pdf.

[13] D. Farfurnik, Y. Horowicz, and N. Bar-Gill. "Identifying and decoupling many-body interactions in spin ensembles in diamond". In: *Phys. Rev. A* 98 (3 Sept. 2018), p. 033409. DOI: 10.1103/PhysRevA.98.033409. URL: https://link.aps.org/doi/10.1103/PhysRevA.98.033409.

[14] Regina Finsterhölzl et al. "Using Matrix-Product States for Open Quantum Many-Body Systems: Efficient Algorithms for Markovian and Non-Markovian Time-Evolution". en. In: *Entropy* 22.9 (Sept. 2020). Number: 9 Publisher: Multidisciplinary Digital Publishing Institute, p. 984. ISSN: 1099-4300. DOI: 10.3390/e22090984. URL: https://www.mdpi.com/1099-4300/22/9/984.

[15] F. Fröwis, V. Nebendahl, and W. Dür. “Tensor operators: Constructions and applications for long-range interaction systems”. In: *Physical Review A* 81.6 (June 2010). Publisher: American Physical Society, p. 062337. DOI: `10.1103/PhysRevA.81.062337`. URL: `https://link.aps.org/doi/10.1103/PhysRevA.81.062337`.

[16] Takahiro Fukui et al. “Perfect selective alignment of nitrogen-vacancy centers in diamond”. en. In: *Applied Physics Express* 7.5 (Apr. 2014). Publisher: IOP Publishing, p. 055201. ISSN: 1882-0786. DOI: `10.7567/APEX.7.055201`. URL: `https://iopscience.iop.org/article/10.7567/APEX.7.055201/meta`.

[17] Gerald E. Fux et al. “Tensor network simulation of chains of non-Markovian open quantum systems”. en. In: *Phys. Rev. Research* 5.3 (Aug. 2023), p. 033078. ISSN: 2643-1564. DOI: `10.1103/PhysRevResearch.5.033078`. URL: `https://link.aps.org/doi/10.1103/PhysRevResearch.5.033078`.

[18] Vittorio Giovannetti, Seth Lloyd, and Lorenzo Maccone. “Advances in quantum metrology”. en. In: *Nature Photonics* 5.4 (Apr. 2011). Publisher: Nature Publishing Group, pp. 222–229. ISSN: 1749-4893. DOI: `10.1038/nphoton.2011.35`. URL: `https://www.nature.com/articles/nphoton.2011.35`.

[19] Vittorio Giovannetti, Seth Lloyd, and Lorenzo Maccone. “Quantum Metrology”. In: *Physical Review Letters* 96.1 (Jan. 2006). Publisher: American Physical Society, p. 010401. DOI: `10.1103/PhysRevLett.96.010401`. URL: `https://link.aps.org/doi/10.1103/PhysRevLett.96.010401`.

[20] Vittorio Giovannetti, Seth Lloyd, and Lorenzo Maccone. “Quantum-Enhanced Measurements: Beating the Standard Quantum Limit”. In: *Science* 306.5700 (Nov. 2004). Publisher: American Association for the Advancement of Science, pp. 1330–1336. DOI: `10.1126/science.1104149`. URL: `https://www.science.org/doi/10.1126/science.1104149`.

[21] Moriyoshi Haruyama et al. “Triple nitrogen-vacancy centre fabrication by C5N4Hn ion implantation”. In: *Nature Communications 2019 10:1* 10.1 (June 2019). Publisher: Nature Publishing Group, pp. 1–9. ISSN: 2041-1723. DOI: `10.1038/s41467-019-10529-x`. URL: `https://www.nature.com/articles/s41467-019-10529-x`.

[22] Philipp Hyllus et al. “Fisher information and multiparticle entanglement”. In: *Physical Review A* 85.2 (Feb. 2012). Publisher: American Physical Society, p. 022321. DOI: `10.1103/PhysRevA.85.022321`. URL: `https://link.aps.org/doi/10.1103/PhysRevA.85.022321`.

[23] I Jakobi et al. "Efficient creation of dipolar coupled nitrogen-vacancy spin qubits in diamond". en. In: *Journal of Physics: Conference Series* 752.1 (Sept. 2016). Publisher: IOP Publishing, p. 012001. ISSN: 1742-6596. DOI: `10.1088/1742-6596/752/1/012001`. URL: `https://dx.doi.org/10.1088/1742-6596/752/1/012001`.

[24] Marcin Jarzyna and Rafał Demkowicz-Dobrza ński. "Matrix Product States for Quantum Metrology". In: *Phys. Rev. Lett.* 110 (24 June 2013), p. 240405. DOI: `10.1103/PhysRevLett.110.240405`. URL: `https://link.aps.org/doi/10.1103/PhysRevLett.110.240405`.

[25] Kosuke Kimura et al. "Creation of multiple NV centers by phthalocyanine ion implantation". en. In: *Applied Physics Express* 15.6 (May 2022). Publisher: IOP Publishing, p. 066501. ISSN: 1882-0786. DOI: `10.35848/1882-0786/ac7030`. URL: `https://dx.doi.org/10.35848/1882-0786/ac7030`.

[26] G. Kucsko et al. "Critical Thermalization of a Disordered Dipolar Spin System in Diamond". In: *Phys. Rev. Lett.* 121 (2 July 2018), p. 023601. DOI: `10.1103/PhysRevLett.121.023601`. URL: `https://link.aps.org/doi/10.1103/PhysRevLett.121.023601`.

[27] Matthias M. Müller et al. "One decade of quantum optimal control in the chopped random basis". en. In: *Reports on Progress in Physics* 85.7 (June 2022). Publisher: IOP Publishing, p. 076001. ISSN: 0034-4885. DOI: `10.1088/1361-6633/ac723c`. URL: `https://dx.doi.org/10.1088/1361-6633/ac723c`.

[28] Sara Murciano, Jérôme Dubail, and Pasquale Calabrese. "More on symmetry resolved operator entanglement". en. In: *Journal of Physics A: Mathematical and Theoretical* 57.14 (Mar. 2024). Publisher: IOP Publishing, p. 145002. ISSN: 1751-8121. DOI: `10.1088/1751-8121/ad30d1`. URL: `https://dx.doi.org/10.1088/1751-8121/ad30d1`.

[29] "Nanoscale quantum sensing with Nitrogen-Vacancy centers in nanodiamonds – A magnetic resonance perspective". en-US. In: *Progress in Nuclear Magnetic Resonance Spectroscopy* 134-135 (Apr. 2023). Publisher: Pergamon, pp. 20–38. ISSN: 0079-6565. DOI: `10.1016/j.pnmrs.2022.12.001`. URL: `https://www.sciencedirect.com/science/article/pii/S0079656522000322`.

[30] J. A. Nelder and R. Mead. "A Simplex Method for Function Minimization". In: *The Computer Journal* 7.4 (Jan. 1965), pp. 308–313. ISSN: 0010-4620. DOI: `10.1093/comjnl/7.4.308`. URL: `https://doi.org/10.1093/comjnl/7.4.308`.

[31] Román Orús. "A practical introduction to tensor networks: Matrix product states and projected entangled pair states". en. In: *Annals of Physics* 349 (Oct. 2014), pp. 117–158. ISSN: 0003-4916. DOI: 10.1016/j.aop.2014.06.013. URL: https://www.sciencedirect.com/science/article/pii/S0003491614001596.

[32] Christian Osterkamp et al. "Engineering preferentially-aligned nitrogen-vacancy centre ensembles in CVD grown diamond". en. In: *Sci Rep* 9.1 (Apr. 2019). Publisher: Nature Publishing Group, p. 5786. ISSN: 2045-2322. DOI: 10.1038/s41598-019-42314-7. URL: https://www.nature.com/articles/s41598-019-42314-7.

[33] Sebastian Paeckel et al. "Time-evolution methods for matrix-product states". en. In: *Annals of Physics* 411 (Dec. 2019), p. 167998. ISSN: 0003-4916. DOI: 10.1016/j.aop.2019.167998. URL: https://www.sciencedirect.com/science/article/pii/S0003491619302532.

[34] Matteo G. A. Paris. "Quantum estimation for quantum technology". In: *International Journal of Quantum Information* 07.supp01 (Jan. 2009). Publisher: World Scientific Publishing Co., pp. 125–137. ISSN: 0219-7499. DOI: 10.1142/S0219749909004839. URL: https://www.worldscientific.com/doi/abs/10.1142/S0219749909004839.

[35] D. Perez-Garcia et al. "Matrix product state representations". In: *Quantum Info. Comput.* 7.5 (July 2007), pp. 401–430. ISSN: 1533-7146.

[36] Luca Pezzé and Augusto Smerzi. "Entanglement, Nonlinear Dynamics, and the Heisenberg Limit". In: *Physical Review Letters* 102.10 (Mar. 2009). Publisher: American Physical Society, p. 100401. DOI: 10.1103/PhysRevLett.102.100401. URL: https://link.aps.org/doi/10.1103/PhysRevLett.102.100401.

[37] Guillermo Preisser et al. "Comparing bipartite entropy growth in open-system matrix-product simulation methods". In: *Physical Review A* 108.1 (July 2023). Publisher: American Physical Society, p. 012616. DOI: 10.1103/PhysRevA.108.012616. URL: https://link.aps.org/doi/10.1103/PhysRevA.108.012616.

[38] Phila Rembold et al. "Introduction to quantum optimal control for quantum sensing with nitrogen-vacancy centers in diamond". In: *AVS Quantum Science* 2.2 (June 2020). Publisher: American Vacuum Society, p. 024701. DOI: 10.1116/5.0006785. URL: https://avs.scitation.org/doi/10.1116/5.0006785.

[39] Marco Rossignolo et al. "QuOCS: The quantum optimal control suite". In: *Computer Physics Communications* 291 (Oct. 2023), p. 108782. ISSN: 0010-4655. DOI: `10.1016/j.cpc.2023.108782`. URL: `https://www.sciencedirect.com/science/article/pii/S0010465523001273`.

[40] Jirawat Saiphet and Daniel Braun. "Simulation of the dissipative dynamics of strongly interacting nitrogen-vacancy centers with tensor networks". In: *Physical Review A* 111.2 (Feb. 2025). Publisher: American Physical Society, p. 022604. DOI: `10.1103/PhysRevA.111.022604`. URL: `https://link.aps.org/doi/10.1103/PhysRevA.111.022604` (visited on 04/28/2025).

[41] Anders W. Sandvik. "Ground States of a Frustrated Quantum Spin Chain with Long-Range Interactions". en. In: *Phys. Rev. Lett.* 104.13 (Mar. 2010), p. 137204. ISSN: 0031-9007, 1079-7114. DOI: `10.1103/PhysRevLett.104.137204`. URL: `https://link.aps.org/doi/10.1103/PhysRevLett.104.137204`.

[42] Sebastian Schiffer et al. "Many-body localization in XY spin chains with long-range interactions: An exact-diagonalization study". In: *Phys. Rev. A* 100.6 (Dec. 2019). Publisher: American Physical Society, p. 063619. DOI: `10.1103/PhysRevA.100.063619`. URL: `https://link.aps.org/doi/10.1103/PhysRevA.100.063619`.

[43] Anthony W. Schlimgen et al. "Quantum simulation of the Lindblad equation using a unitary decomposition of operators". In: *Phys. Rev. Res.* 4 (2 June 2022), p. 023216. DOI: `10.1103/PhysRevResearch.4.023216`. URL: `https://link.aps.org/doi/10.1103/PhysRevResearch.4.023216`.

[44] Ulrich Schollwöck. "The density-matrix renormalization group in the age of matrix product states". In: *Annals of Physics*. January 2011 Special Issue 326.1 (Jan. 2011), pp. 96–192. ISSN: 0003-4916. DOI: `10.1016/j.aop.2010.09.012`. URL: `https://www.sciencedirect.com/science/article/pii/S0003491610001752`.

[45] Saravanan Sengottuvel et al. "Wide-field magnetometry using nitrogen-vacancy color centers with randomly oriented micro-diamonds". en. In: *Scientific Reports* 12.1 (Oct. 2022). Publisher: Nature Publishing Group, p. 17997. ISSN: 2045-2322. DOI: `10.1038/s41598-022-22610-5`. URL: `https://www.nature.com/articles/s41598-022-22610-5`.

[46] J. M. Taylor et al. "High-sensitivity diamond magnetometer with nanoscale resolution". en. In: *Nature Phys* 4.10 (Oct. 2008). Publisher: Nature Publishing

Group, pp. 810–816. ISSN: 1745-2481. DOI: 10.1038/nphys1075. URL: https://www.nature.com/articles/nphys1075.

[47] "The NV0 defects in diamond: A quantum mechanical characterization through its vibrational and Electron Paramagnetic Resonance spectroscopies". en-US. In: *Journal of Physics and Chemistry of Solids* 160 (Jan. 2022). Publisher: Pergamon, p. 110304. ISSN: 0022-3697. DOI: 10.1016/j.jpcs.2021.110304. URL: https://www.sciencedirect.com/science/article/abs/pii/S002236972100370X.

[48] Guifré Vidal. "Efficient Classical Simulation of Slightly Entangled Quantum Computations". In: *Phys. Rev. Lett.* 91.14 (Oct. 2003). Publisher: American Physical Society, p. 147902. DOI: 10.1103/PhysRevLett.91.147902. URL: https://link.aps.org/doi/10.1103/PhysRevLett.91.147902.

[49] Kseniia Volkova et al. "Optical and Spin Properties of NV Center Ensembles in Diamond Nano-Pillars". In: *Nanomaterials* 12.9 (2022). ISSN: 2079-4991. DOI: 10.3390/nano12091516. URL: https://www.mdpi.com/2079-4991/12/9/1516.

[50] Cao Wang et al. "Realization of high-dynamic-range broadband magnetic-field sensing with ensemble nitrogen-vacancy centers in diamond". In: *Review of Scientific Instruments* 94.1 (Jan. 2023), p. 015109. ISSN: 0034-6748. DOI: 10.1063/5.0089908. URL: https://doi.org/10.1063/5.0089908.

[51] P. Welter et al. "Scanning nitrogen-vacancy center magnetometry in large in-plane magnetic fields". In: *Applied Physics Letters* 120.7 (Feb. 2022), p. 074003. ISSN: 0003-6951. DOI: 10.1063/5.0084910. URL: https://aip.scitation.org/doi/abs/10.1063/5.0084910.

[52] A. H. Werner et al. "Positive Tensor Network Approach for Simulating Open Quantum Many-Body Systems". In: *Physical Review Letters* 116.23 (June 2016). Publisher: American Physical Society, p. 237201. DOI: 10.1103/PhysRevLett.116.237201. URL: https://link.aps.org/doi/10.1103/PhysRevLett.116.237201.

[53] Weijie Wu et al. *Spin squeezing in an ensemble of nitrogen-vacancy centers in diamond.* 2025. arXiv: 2503.14585 [quant-ph]. URL: https://arxiv.org/abs/2503.14585.

[54] Zhujing Xu et al. "Quantum information processing with closely-spaced diamond color centers in strain and magnetic fields". In: *Opt. Mater. Express* 9.12 (Dec. 2019), pp. 4654–4668. DOI: 10.1364/OME.9.004654. URL: https://opg.optica.org/ome/abstract.cfm?URI=ome-9-12-4654.

[55] Huijie Zheng et al. “Zero-Field Magnetometry Based on Nitrogen-Vacancy Ensembles in Diamond”. In: *Phys. Rev. Appl.* 11.6 (June 2019). Publisher: American Physical Society, p. 064068. DOI: `10.1103/PhysRevApplied.11.064068`. URL: `https://link.aps.org/doi/10.1103/PhysRevApplied.11.064068`.

[56] Hengyun Zhou et al. “Quantum Metrology with Strongly Interacting Spin Systems”. In: *Phys. Rev. X* 10.3 (July 2020). Publisher: American Physical Society, p. 031003. DOI: `10.1103/PhysRevX.10.031003`. URL: `https://link.aps.org/doi/10.1103/PhysRevX.10.031003`.

[57] Yuchun Zhu et al. *Simulation of ODMR Spectra from Nitrogen-Vacancy Ensembles in Diamond for Electric Field Sensing*. arXiv:2301.04106 [quant-ph]. Jan. 2023. DOI: `10.48550/arXiv.2301.04106`. URL: `http://arxiv.org/abs/2301.04106`.

Appendix: publications

First Publication

PHYSICAL REVIEW A **111**, 022604 (2025)

Simulation of the dissipative dynamics of strongly interacting nitrogen-vacancy centers with tensor networks

Jirawat Saiphet[*] and Daniel Braun
Institut für Theoretische Physik, Eberhard Karls Universität Tübingen, 72076 Tübingen, Germany

(Received 12 July 2024; revised 22 November 2024; accepted 24 January 2025; published 5 February 2025)

Nitrogen-vacancy (NV) centers in diamond are a promising platform for highly sensitive quantum sensors for magnetic fields and other physical quantities. The quest for high sensitivity combined with high spatial resolution naturally leads to dense ensembles of NV centers and hence to strong, long-range interactions between them. Hence, simulating strongly interacting NVs becomes essential. However, obtaining the exact dynamics for a many-spin system is a challenging task due to the exponential scaling of the Hilbert space dimension, a problem that is exacerbated when the system is modeled as an open quantum system. In this work, we employ the matrix product density operator (MPDO) method to represent the many-body mixed state and to simulate the dynamics of an ensemble of NVs in the presence of strong long-range couplings due to dipole-dipole forces. We benchmark different time-evolution algorithms in terms of numerical accuracy and stability against time evolution based on exact numerical diagonalization. Subsequently, we simulate the dynamics in the strong-interaction regime and study the impact of decoherence on the accuracy of the MPDO method. Last, we investigate the dynamics of quantum Fisher information and show that for small distances below about 5 nm the resulting strong dipole-dipole interaction can improve the sensitivity for magnetic field sensing when the ensemble is driven by pulses of constant amplitude.

DOI: 10.1103/PhysRevA.111.022604

I. INTRODUCTION

Probing magnetic fields with high sensitivity and resolution is important in cutting-edge research applications. A single nitrogen-vacancy (NV) center in diamond was proposed as a nanoscale probe [1] and used for measuring a magnetic field [2,3]. Recently, controlled systems of double and triple NV centers were successfully fabricated [4]. Using NV center ensembles with many spins has the potential to increase the sensitivity by having more spins in a probe [5–7]. Requiring, at the same time, high spatial resolution leads to ensembles with high density. The resulting strong dipole-dipole interactions between the NV centers lead, however, to a rapid population of subspaces of Hilbert space with reduced total spin. For example, if we had two spins $1/2$, not only would the triplet states get populated, but so would the antisymmetric singlet state, resulting in a reduced response to the applied magnetic field. This can be considered a form of intrinsic decoherence [8] in addition to the remaining external decoherence mechanisms, resulting in short coherence times [9] and hence less sensitivity. Decoupling the interactions with specific control pulses or engineering the alignments of NV centers to reduce interactions can increase the coherence time and sensitivity [8,10,11]. However, ideally, one would like to profit from the interactions for generating entangled states that could highly enhance the sensitivity of the probe.

To model and optimize entanglement generation in a dissipative system with strong and long-range interactions, simulations of its dynamics in the presence of microwave control pulses is necessary. However, given the many-body nature of an ensemble, simulating its exact dynamics is intractable. Exact simulations of closed spin-$1/2$ systems with long-range interaction have been implemented for up to 32 spins [8,12–14] and up to 12 spins with dissipation [15,16]. In order to address this challenge, we use a tensor network approach to capture the dynamics of the ensemble. Matrix product states (MPSs) [17–20] were proposed for the efficient simulation of quantum metrology [21] and open quantum systems [22]. Simulations of non-Markovian systems have been performed using matrix product operators (MPOs) with a nearest-neighbor model [23,24].

In this work, we consider an NV center ensemble that consists of spin-1 particles. All NV centers interact with each other via long-range dipole-dipole interaction. We simulate the dissipative dynamics by using the matrix product density operator (MPDO) method. We investigate the efficiency of using MPDOs in simulating dynamics in the strong-interaction limit and under dissipation. Operator entanglement entropy (opEE) is computed and used to demonstrate the interplay between strong interaction and dissipation for the capability of the MPDO to approximate the exact states. We then address and quantify possible sensitivity improvements from NV-NV interactions during the time evolution using quantum Fisher information.

II. THEORY

A. Strongly interacting NV centers

An NV center is a spin-1 system that forms in a carbon lattice of diamonds if two adjacent carbons are replaced by a nitrogen atom and a vacancy. Without an external

---

[*] Contact author: jirawat.saiphet@uni-tuebingen.de

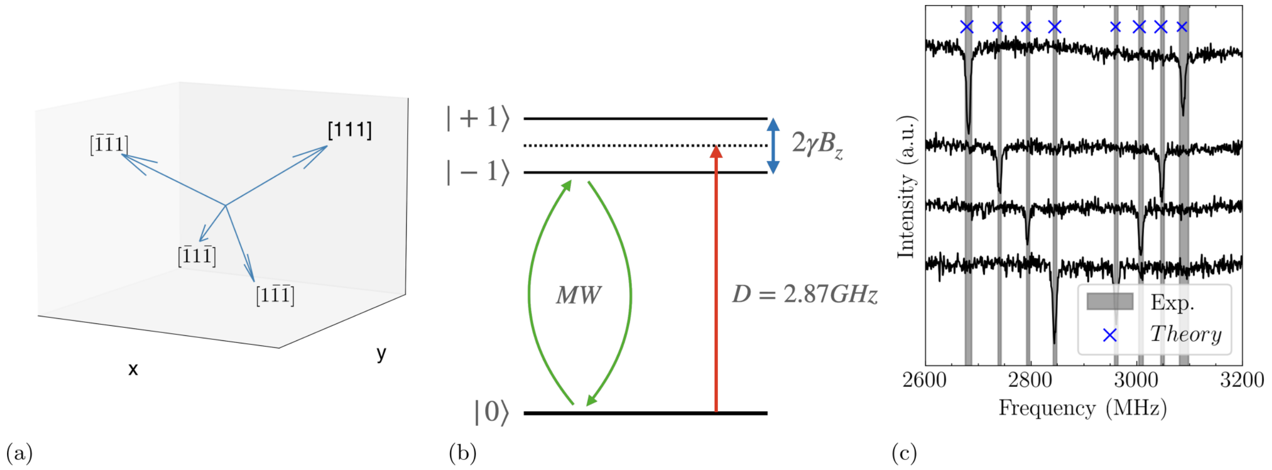

FIG. 1. (a) Four possible orientations given by diamond's crystallographic axes. (b) Energy levels of an NV center. (c) ODMR spectra of four different axes from measurements and analytic calculations.

field applied, the diamond structure creates a zero-field splitting. Energy levels corresponding to states $|0\rangle$ and $|\pm 1\rangle$, with $m_s = 0, \pm 1$, respectively, are separated by $D = 2\pi \times 2870$ MHz.

Diamond's crystallographic axes provide four possible orientations of the principal axes of the NV center [see Fig. 1(a)], separating them into different groups. For example, the NV center in the [111] group has $\hat{z}$ parallel to a unit vector $\frac{1}{\sqrt{3}}(1, 1, 1)$. Different groups have different couplings to the magnetic field, which leads to different energy levels that can be distinguished by optically detected magnetic resonance (ODMR).

In an external magnetic field, the field component B_z along the NV center's principal axis creates an additional energy splitting between $|-1\rangle$ and $|+1\rangle$ proportional to B_z. This allows selective transitions from the ground state $|0\rangle$ to one of the two exited states by applying a microwave field at resonance frequency. Here, we restrict ourselves to a transition to $|-1\rangle$.

The Hamiltonian for an individual NV center with microwave drive with Rabi frequency $\Omega(t)$ is given by

$$\hat{H}_{\mathrm{NV},i} = \hbar\big(D\hat{S}_z^2 + g_s\mu_{\mathrm{B}}B_z^{(i)}\hat{S}_z + \Omega(t)\cos(\omega t)\hat{S}_x^{(i)}\big), \tag{1}$$

where $g_s \simeq 2$ and μ_{B} is the Bohr magneton. The spin operators for $S = 1$ are

$$\hat{S}_x = \frac{1}{\sqrt{2}}\begin{pmatrix} 0 & 1 & 0 \\ 1 & 0 & 1 \\ 0 & 1 & 0 \end{pmatrix}, \quad \hat{S}_y = \frac{i}{\sqrt{2}}\begin{pmatrix} 0 & -1 & 0 \\ 1 & 0 & -1 \\ 0 & 1 & 0 \end{pmatrix},$$

$$\hat{S}_z = \begin{pmatrix} 1 & 0 & 0 \\ 0 & 0 & 0 \\ 0 & 0 & -1 \end{pmatrix}. \tag{2}$$

Applying the unitary $\hat{U} = e^{i\omega t\hat{S}_z^2}$ to Eq. (1) to transform to a frame corotating with the microwave and using the rotating-wave approximation yields

$$\hat{H}_{\mathrm{NV},i} = \hbar\left((D - \omega)\hat{S}_z^2 + g_s\mu_{\mathrm{B}}B_z^{(i)}\hat{S}_z + \frac{\Omega(t)}{2}\hat{S}_x^{(i)}\right). \tag{3}$$

At resonance frequency, $\omega = D \pm g_s\mu_{\mathrm{B}}B_z^{(i)}$, the microwave drive makes a transition between $|0\rangle \leftrightarrow |\pm 1\rangle$ for the ith NV center. The energy levels of $\hat{H}_{\mathrm{NV},i}$ are depicted in Fig. 1(b). They agree with the experimental observation [4].

NV centers interact with each other via dipole-dipole interaction. We consider a case of strong interaction between NV centers and hence ignore nuclear spin. The general definition of dipole-dipole interaction between NV center i and NV center j is

$$H_{\mathrm{dip},ij} = -\frac{\mu_0(g_s\mu_{\mathrm{B}})^2\hbar^2}{4\pi r_{ij}^3}[3(\vec{S}^{(i)} \cdot \hat{r})(\vec{S}^{(j)} \cdot \hat{r}) - \vec{S}^{(i)}\vec{S}^{(j)}], \tag{4}$$

where $\vec{S}^{(i)} = (\hat{S}_x, \hat{S}_y, \hat{S}_z)^{(i)}$ are spin operators of NV center i and $\hat{r}_{ij} = (r_x, r_y, r_z)_{ij}$ are the unit vectors connecting the two NV centers. We restrict ourselves to the case where all NV center centers have the same orientation. The dipole-dipole interaction in the rotating frame can then be transformed into an effective Hamiltonian [16],

$$\hat{H}_{\mathrm{eff},\{ij\}} = C_{\mathrm{dip}}\big(\tfrac{1}{2}\big(\hat{S}_x^{(i)}\hat{S}_x^{(j)} + \hat{S}_y^{(i)}\hat{S}_y^{(j)}\big) - \hat{S}_z^{(i)}\hat{S}_z^{(j)}\big), \tag{5}$$

where $C_{\mathrm{dip}} = \frac{J_0 q_{ij}}{r_{ij}^3}$, $J_0 = \frac{\mu_0\hbar^2(g_s\mu_{\mathrm{B}})^2}{4\pi} = 2\pi \times 52\,\mathrm{MHz\,nm}^3$, and $q_{ij} = 3(\hat{r}_{ij} \cdot \hat{z}_i)(\hat{r}_{ij} \cdot \hat{z}_j) - \hat{z}_i \cdot \hat{z}_j$, with $\hat{z}_i$ being the unit vector pointing in the direction of dipole i. It reduces to $q_{ij} = (3\cos^2\theta - 1)$ and $\cos\theta \equiv \hat{z}_i \cdot \hat{r}_{ij}$ in the case of the same group ($\hat{z}_i = \hat{z}_j$).

B. Tensor network state

Due to the r^{-3} scaling, the interactions within an ensemble of NV centers extends beyond the nearest neighbors and becomes long range. These all-to-all interactions increase complexity and limit our capability to exactly simulate the system to only a few spins. To simulate the many-body dynamics for an ensemble of NV centers, we represent the quantum state as a tensor network state. The state of a closed system is decomposed into a one-dimensional tensor network structure, called a matrix product state [17–20],

$$|\Psi\rangle = \sum_{i_1 \cdots i_N = 1}^{d} A^{i_1}A^{i_2} \cdots A^{i_N}|i_1 \cdots i_N\rangle, \tag{6}$$

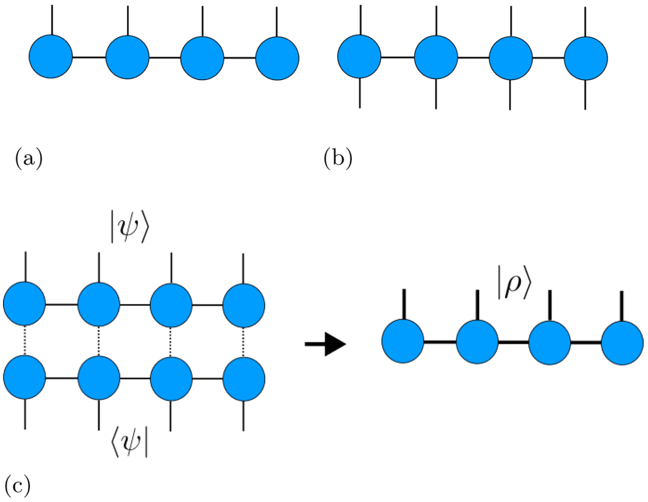

FIG. 2. Tensor diagrams representing (a) MPS, a wave function for a pure state; (b) MPO, an operator; and (c) MPDO, a vectorized density operator constructed from an MPS and its conjugate by contracting auxiliary indices, depicted as dashed lines, and combining corresponding physical (bonds) indices. The thick line implies square dimensions compared to the original index.

where a matrix A^{i_n} has matrix elements $A^{i_n}_{\alpha_{(n-1)}\alpha_n}$. The MPS decomposition in Eq. (6) can be visualized by the tensor diagram in Fig. 2(a), where each sphere visualizes a tensor A^{i_n} and lines are indices of the tensors. The connecting lines represent a contraction by summation over a shared index of two tensors. Each matrix element $A^{i_n}_{\alpha_{(n-1)}\alpha_n}$ in the MPS contains a physical index i_n representing the local Hilbert space of the nth NV center. The virtual index, or bond index α_n, having bond dimensions $d(\alpha_n) = \chi_n$ [except for $d(\alpha_0) = d(\alpha_N) = 1$], labels links between two tensors. Those linked bonds will be contracted when we extract any observable from the MPS. For example, the contraction of a shared index between tensors $A^{i_{n-1}}A^{i_n} \equiv \sum_{\alpha_{(n-1)}=1}^{\chi_{(n-1)}} A^{i_{n-1}}_{\alpha_{(n-2)}\alpha_{(n-1)}} A^{i_n}_{\alpha_{(n-1)}\alpha_n}$ happens between the left bond index α_{n-1} of A^{i_n} and the right bond index α_{n-1} of $A^{i_{n-1}}$. Note that in Eq. (6) we use notation where the summation over α_n is not written explicitly and $n = 1, \ldots, N$. Physically, the bond dimension contains information about the entanglement entropy between the two parts of the tensor network that the bond connects. Using MPS allows us to compress the bond dimensions and to efficiently represent the ground state in compact, small Hilbert spaces.

A similar tensor network structure can be adapted to simulate an open system [25,26]. To represent an operator we need a MPO as given in Fig. 2(b). This MPO, in an orthogonal basis, represents a density operator of the system,

$$\hat{\rho} = \sum_{i_1 \cdots i_N = 1}^{d} \sum_{i'_1 \cdots i'_N = 1}^{d} B^{i_1 i'_1} B^{i_2 i'_2} \cdots B^{i_N i'_N} |i_1 \cdots i_N\rangle\langle i'_1 \cdots i'_N|. \quad (7)$$

For pure states, this MPO can be constructed by contracting auxiliary indices of two MPS and then combining corresponding physical (bond) indices. Furthermore, we combine the physical indices to create a MPDO representing a vectorized density operator:

$$|\rho\rangle\rangle = \sum_{j_1 \cdots j_N = 1}^{d^2} B^{j_1} B^{j_2} \cdots B^{j_N} |j_1 \cdots j_N\rangle\rangle. \quad (8)$$

Here, $j_n = (i_n, i'_n)$ and $|j_n\rangle \in \mathbb{C}^{d^2}$ is combined from two physical indices. The dimension of each resulting index is doubled compared to the MPS. A graphical representation of this process is shown in Fig. 2(c).

C. Simulation of dissipative dynamics

We simulate ρ directly, including dissipation, by solving the vectorized master equation

$$\frac{\partial}{\partial t}|\rho\rangle\rangle = \mathcal{L}|\rho\rangle\rangle, \quad (9)$$

where $|\rho\rangle\rangle$ is the MPDO given by Eq. (8) and $\mathcal{L}$ is a vectorized Lindblad operator defined as

$$\begin{aligned}\mathcal{L}(t) = & -i[\hat{H}(t) \otimes \mathbb{I} - \mathbb{I} \otimes \hat{H}^T(t)] \\ & + \sum_i \gamma_i \left\{ L_i \otimes (L_i^\dagger)^T - \frac{1}{2}[L_i^\dagger L_i \otimes \mathbb{I} + \mathbb{I} \otimes (L_i^\dagger L_i)^T] \right\}.\end{aligned} \quad (10)$$

Note that when $\gamma_i = 0$, the dynamics are unitary. In this case when MPS is sufficient to simulate the system, utilizing MPDO is unnecessary and computationally more expensive due to the squared memory.

III. RESULTS

We simulate a one-dimensional spin-1 chain with long-range interaction and dissipation using MPDOs. We assume uniform separation for nearest-neighbor spins, $r_{i,i+1} = r$ for any $i = 1, 2, \ldots, N$. All spins align on the xy plane such that the position $\vec{r}^{(i)} = r(i, i, 0)/\sqrt{2}$. For the very strong interaction regime, this separation is set to be $r < 2$ nm, while experiments with dense samples reached $r \sim 5$ nm [4]. In our simulations we use the following conditions: (1) The amplitude of the external magnetic field is chosen to match the level splitting read off from the top line in Fig. 1(c), $2g_s\mu_B B_z = 2\pi \times 407$ MHz. (2) Uniform Rabi frequency $\Omega(t) = \Omega = 2\pi \times 2.00$ MHz for driving the $|0\rangle \leftrightarrow |-1\rangle$ transition, with $\omega = D - g_s\mu_B B_z$. (3) All NV centers belong to the same orientation group parallel to [111]. (4) Time step $dt = 1$ ns. (5) The initial state is $|0\rangle^{\otimes N}$.

A. Simulation algorithms in the strong-interaction regime without dissipation

First, we investigate the precision and numerical stability of tensor network algorithms in the very strong interaction regime with $\gamma_i = 0$ for two different algorithms that simulate time evolution and support the long-range model [27]: (1) the MPO W^{II} [28] and (2) the time-dependent variational principle (TDVP) [29,30]. We simulate the dynamics of ensembles of up to 10 NV centers and $\chi_{\max} = 16$. Here, $\chi_{\max}$ is a maximum dimension for all bonds. First of all, we find that the same dynamics are produced from both W^{II} and the TDVP. This is shown as a small discrepancy in the real part of $\langle S_z\rangle$ of

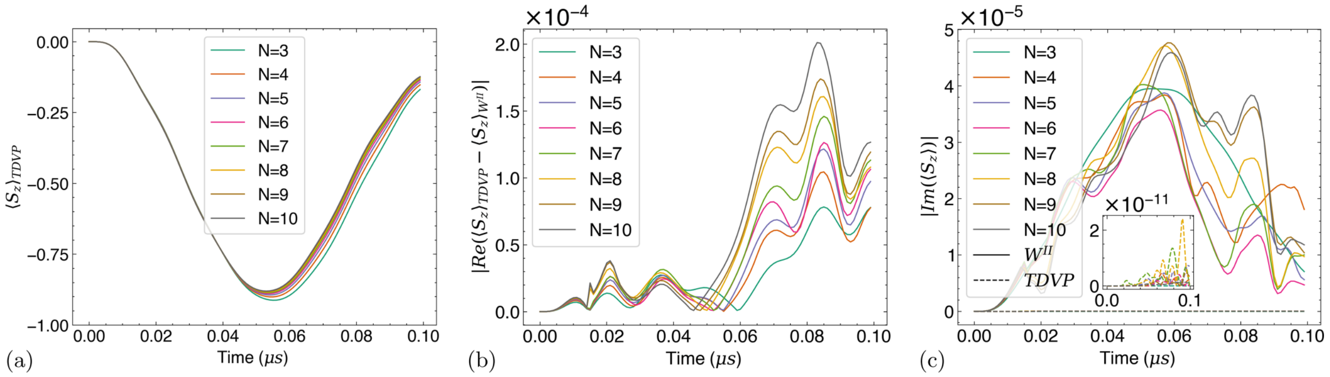

FIG. 3. Comparison of simulation results between W^{II} and TDVP algorithms for different N. (a) Real-time evolution of $\langle S_z\rangle$ calculated from the TDVP algorithm with MPDO. (b) Difference in the real part of $\langle S_z\rangle$ from the TDVP and W^{II} algorithms. (c) Numerical errors in the imaginary part of the W^{II} algorithm (main plot) are 5 orders of magnitude larger than in the TDVP algorithm (inset).

the whole system produced by the two algorithms in Fig. 3(b) when $r = 2\,\mathrm{nm}$. However, the TDVP has significantly smaller errors in the imaginary parts, as shown in Fig. 3(c). Furthermore, in Fig. 4 we observe that the W^{II} can be numerically unstable under certain condition, i.e., when the interaction Hamiltonian is fully modeled by Eq. (4) and not approximated by Eq. (5). The algorithm fails to produce a normalized value for expected magnetization $\langle S_z\rangle$ when the interaction strength becomes stronger while the TDVP is still valid compared to exact diagonalization. This is shown in Fig. 4 for $N = 3$ and $r = 0.5\,\mathrm{nm}$. We suspect that the observable divergence in W^{II} is a result of exploiting the complex time-step technique mentioned in [27] to improve the propagation error, as using the technique destroys the unitarity of the propagator. However, without the technique, the numerical error of propagating the quantum state with the W^{II} method compared to the exact evolution dramatically degrades from $O(dt^2)$ to $O(dt)$. In this case, the algorithm will not be able to capture the correct dynamics even in the weaker-interaction regime. To avoid this problem, we keep the TDVP as the main algorithm for our simulations.

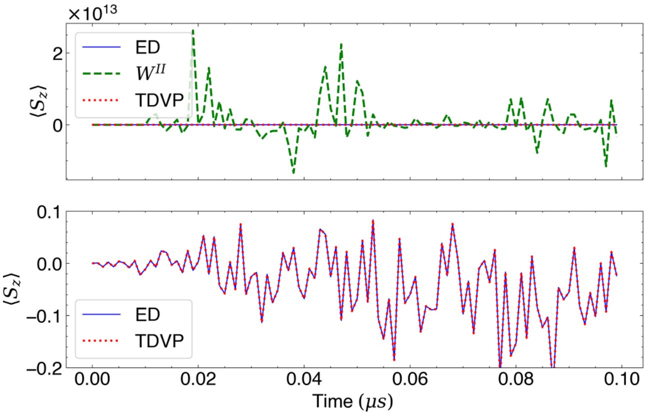

FIG. 4. W^{II} can fail when interaction becomes very strong (see top panel), while TDVP gives the same dynamics as exact diagonalization (bottom panel). Results are for $N = 3$ and $r = 0.5\,\mathrm{nm}$.

B. Dissipative dynamics with finite bond dimensions

A major source of error when using MPSs or MPDOs is truncation error. Keeping finite bond dimensions and truncating when the bond indices exceed $\chi_{\max}$ introduce an error. This error is given by the square root of the sum of squares of the truncated singular values of all bonds,

$$\epsilon = \sqrt{\sum_{k>\chi_{\max}} (s_k)^2}. \tag{11}$$

Typically, these errors remain bounded if the state has entanglement that follows an area law, e.g., when the system has only nearest-neighbor interactions. In such a case, the bond dimension grows with small singular values during the time evolution, allowing the simulation of large systems with small error. However, since we are considering a case of long-range interaction, this argument should not hold. In Figs. 5 and 6 we plot simulation results for different $\chi_{\max}$ with $r = 2.0\,\mathrm{nm}$ and $r = 1.5\,\mathrm{nm}$ compared to a result from exact diagonalization for $N = 4, 7$. We find that stronger interactions introduce bigger errors in bond truncation. The results for smaller $\chi_{\max}$ follow the exact calculation only as long as entanglement entropy does not reach $\chi_{\max}$, i.e., up to a certain number of time steps before diverging and becoming inaccurate due to truncation errors.

These results imply that a bigger $\chi_{\max}$ is required to capture the dynamics in the presence of long-range, strong interactions, thus making the MPS or MPDO method less efficient. Next, we add dissipation by setting $\gamma_i = \gamma \neq 0$, so each spin has the same dissipation rate. Numerical values of γ are given in $(\mu\mathrm{s})^{-1}$ throughout. For the dissipation operator $\hat{L}_i$ we choose the dephasing operator, $\hat{L}_i = \hat{S}_z$, which is relevant, e.g., for magnetic field noise. Figure 7 shows the absolute errors compared to exact calculations of dissipative dynamics for different $\chi_{\max}$ and different values of r and γ. The discrepancy of these dissipative dynamics compared to the exact one is smaller than in the nondissipative case for the same $\chi_{\max}$. When the growth of singular values of bipartition of the total state across the bond is limited by a larger γ, bond truncation becomes more effective since it introduces fewer

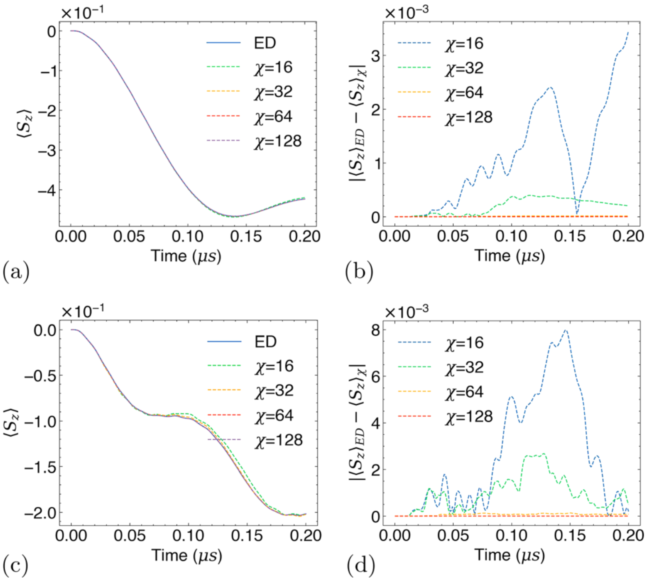

(a) (b) (c) (d)

FIG. 5. Four NV centers with $\gamma = 0$. (a) Average magnetization extracted from MPDO as a function of time and (b) numerical errors compared to exact diagonalization as a function of maximum bond dimension for $r = 2.0$ nm. (c) and (d) The same as (a) and (b), but for 1.5 nm.

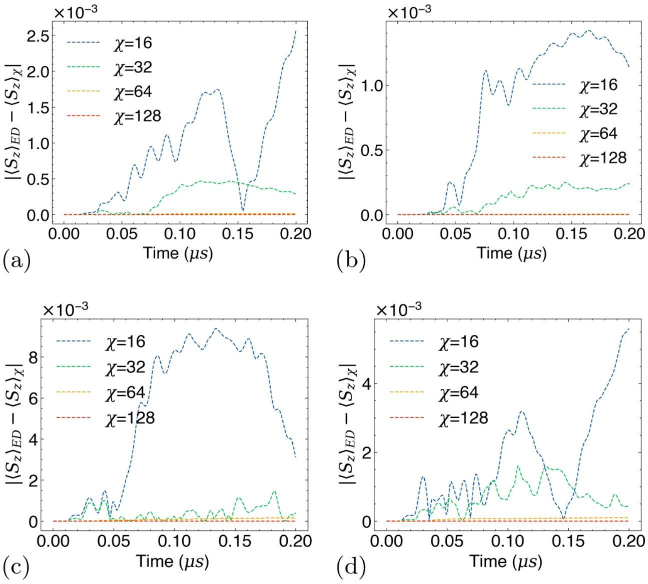

(a) (b) (c) (d)

FIG. 7. Numerical errors compared to exact diagonalization as a function of maximum bond dimension for four NV centers. (a) $r = 2.0$ nm and $\gamma = 1.0$, (b) $r = 2.0$ nm and $\gamma = 5.0$, (c) $r = 1.5$ nm and $\gamma = 1.0$, and (d) $r = 1.5$ nm and $\gamma = 5.0$.

errors. This demonstrates the interplay between the growth of entanglement entropy due to interactions and dissipation, which hinders it. To understand quantitatively how stronger interactions induce entanglement entropy during time evolution, we calculate the opEE of the reduced density matrix determined by cutting the system into two halves at the middle bond and tracing out the other half. We use the von Neuman entropy, which is defined as [31]

$$S_{\mathrm{op}} = -\sum_{i}^{\chi} (\lambda_i)^2 \ln(\lambda_i)^2, \tag{12}$$

where λ_i are singular values of the cut bond with bond dimension χ for the vectorized operator. Here, λ_i are squared because they are singular values of a vectorized operator $|\rho\rangle$. Note that in general, opEE does not give a direct measure of entanglement for mixed states. The opEE for a pure state is twice the value of its standard entanglement entropy, $S_{\mathrm{op}}(|\rho\rangle) = 2S(|\psi\rangle)$, when $\rho = |\psi\rangle\langle\psi|$ [32]. However, the opEE provides insight into how well the state can be approximated by an MPDO, indicating simulation errors from a truncation [33].

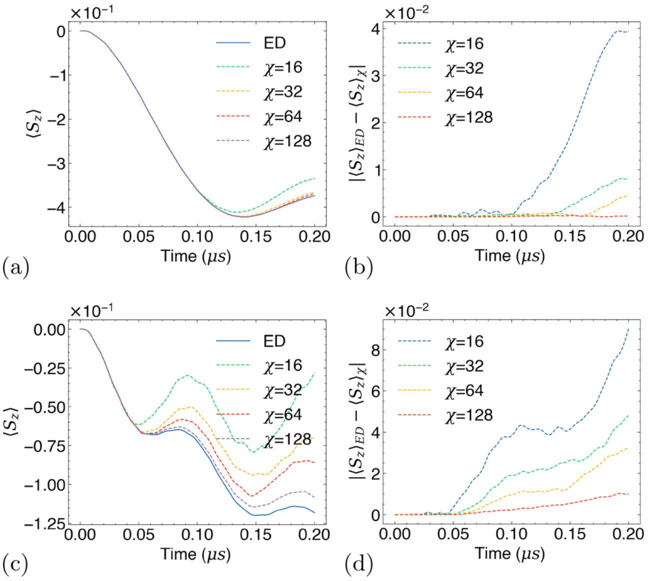

(a) (b) (c) (d)

FIG. 6. Seven NV centers with $\gamma = 0$. (a) Average magnetization extracted from MPDO as a function of time and (b) numerical errors compared to exact diagonalization as a function of maximum bond dimension for $r = 2.0$ nm. (c) and (d) Same as (a) and (b), but for 1.5 nm.

After time evolution, the middle bond index $\alpha_{(N/2+1)}$, which is the bond that equally separates the MPDO into two halves, has the largest dimension. Figure 8 shows the time evolution of the opEE calculated from cutting the middle bond for $N = 4$ and $N = 7$. Figures 8(a) and 8(b) have $\gamma = 0$; Figs. 8(c) and 8(d) show results for different values of γ. The opEE growth as a function of time is accelerated as interactions become stronger. This agrees with the results of larger errors from the truncation shown earlier. Except at very strong interaction, i.e., $r = 1.5$ nm, opEE grows at the beginning and saturates rapidly. For $r = 1.5$ nm, the initial growth is fastest, but opEE continues to grow after a short time interval of a relatively stable value around 0.12 μs. This behavior depends on the Rabi frequency Ω. With the doubling of Ω from $2\pi \times 2$ MHz to $2\pi \times 4$ MHz, the initial rise of the opEE becomes even faster, but the plateau is reached around 0.12 μs [see Fig. 11(a) in Appendix B].

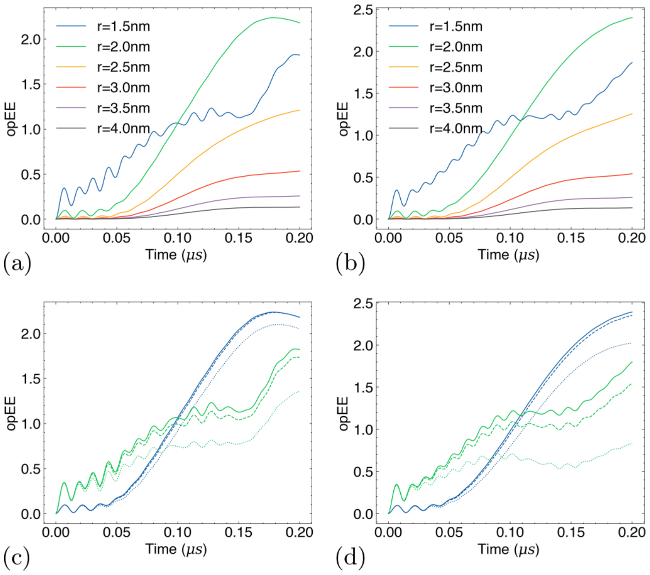

FIG. 8. Operator entanglement entropy [Eq. (12)] of the middle bond. (a) and (b), for $N = 4$ and 7, respectively, show trends of opEE to grow faster when interactions get stronger. Each line has $\gamma = 0$. (c) and (d), for $N = 4$ and $N = 7$, respectively, show dissipation suppresses the generation of opEE. Green: $r = 1.5$ nm; blue: $r = 2.0$ nm. Solid lines, $\gamma = 0.0$; dashed lines, $\gamma = 1.0$; dotted lines, $\gamma = 5.0$.

C. Quantum Fisher information and sensitivity

According to the Cramér-Rao bound, the sensitivity in the estimation of a parameter θ using quantum probes is bounded by the inverse of the quantum Fisher information (QFI), $(\delta\theta)^2 \geqslant \frac{1}{MF_Q}$, where M is the number of independent measurements and F_Q is the QFI [34]. The definition of the QFI for a mixed state $\hat{\rho}$ is given by

$$F_Q = \mathrm{Tr}[\hat{\rho}\hat{L}^2], \tag{13}$$

where $\hat{L}$ is the symmetric logarithmic derivative (SLD) that satisfies

$$\partial_\theta \hat{\rho} = \tfrac{1}{2}(\hat{L}\hat{\rho} + \hat{\rho}\hat{L}). \tag{14}$$

Hence, sensitivities can be improved by repeating the measurements or using more probes. For N independent probes, we obtain the standard quantum limit, $\delta\theta \geqslant O(1/\sqrt{N})$. However, the QFI can increase when the probes are highly entangled. For example, under evolution with a pure Zeeman term and in the absence of decoherence and dissipation, probes prepared in a Greenberger-Horne-Zeilinger state achieve optimal sensitivity for magnetic field measurement that follows the "Heisenberg limit", $\delta\theta \geqslant O(1/N)$ [35].

Thus, since interactions are necessary for the creation of entanglement, dense NV center ensembles harbor the potential for higher sensitivity compared to noninteracting NV centers. However, the lack of permutational symmetry leads to the population of other irreducible representations of SU(2) starting from the one with maximum spin; i.e., on average, the total spin decays, and sensitivity is reduced. Optimal control is therefore necessary to harvest the entanglement from strong interactions to achieve higher sensitivity.

D. Dynamics of QFI

To quantify the sensitivity of the ensemble of interacting NV centers to a uniform magnetic field B_z, we compute the quantum Fisher information of the mixed state during time evolution. Instead of direct calculation using Eq. (13), we use the tensor network approach for calculating the QFI as in [36]. Note that, unlike in the original work [36], we optimize only the SLD and not the input state ρ. In short, we iteratively search for the SLD that satisfies the following definition of the QFI:

$$F(\rho_\phi, L) = \sup_L [2\mathrm{Tr}(\rho'_\phi L) - \mathrm{Tr}(\rho_\phi L^2)]. \tag{15}$$

At the beginning, we randomly create the MPO approximation of an SLD L, given by

$$L = \sum_{jk} \mathrm{Tr}\big(S[1]^{j_1}_{k_1} \cdots S[n]^{j_n}_{k_n}\big)|\mathbf{j}\rangle\langle\mathbf{k}|. \tag{16}$$

Here, $S[l]^{j_l}_{k_l}$ is a Hermitian matrix. In searching for an optimal L we locally update $(S[1]^{j_1}_{k_1}, \ldots, S[n]^{j_n}_{k_n})$ by sweeping from $S[1]$ to $S[n]$ and back to $S[1]$ again until F has converged. For example, when updating $S[l]^{j_l}_{k_l}$, all other tensors S^j_k are fixed and combined. Then after contractions, Eq. (15) becomes

$$F(\rho, L) = 2\sum_\alpha b_\alpha S[l]_\alpha - 2\sum_{\alpha\beta} S[l]_\alpha A_{\alpha\beta} S[l]_\beta. \tag{17}$$

Here, b and A are a vector and a matrix resulting from contracting the fixed tensors and combining the uncontracted indices. A diagrammatic explanation can be found in [36]. Taking the derivative with respect to $S[l]$, $\partial F(\rho, L)/\partial S[L] = 0$, Eq. (17) yields $\frac{1}{2}(A + A^T)|S[l]\rangle = |b\rangle$. A solution to this equation provides a local extremum for the QFI. Since this local update approach tends to get stuck at local extrema, several repetitions with different initial L are needed and can be computationally expensive for large N.

Figure 9 shows the dynamics of the QFI for a nondissipative system with small size and different r. At each time step, we find the optimal SLD from 10 independent realizations and select the one with the largest QFI. Furthermore, we utilize the optimal SLD obtained from the previous time step as the initialization for the current time step. Based on our experience, although the outcome is not guaranteed, implementing such a strategy can lead to a smoother result for the QFI.

According to Fig. 9, the QFI of $r = 4.0$ nm nearly reaches values of N noninteracting probes, denoted as $F_{|+1\rangle^{\otimes N}} = N$. The QFI increases if the interactions are stronger, especially when $r \leqslant 2.5$ nm, leading to a QFI that can be greater than N. This suggests that the sensitivity of the probes is enhanced by the entanglement that is created by the interaction. Still, as for opEE, the QFI remains relatively small when $r = 1.5$ nm, i.e., for very strong interaction. We find that this is because the interaction strength of the nearest NV center pairs ($C_{\mathrm{dip},(i,i+1)} = 2\pi \times 15.41$ MHz) becomes substantially larger than the Rabi frequency ($\Omega = 2\pi \times 2.00$ MHz). As shown Fig. 10, the QFI can be further increased for $r = 1.5$ nm by increasing the Rabi frequency.

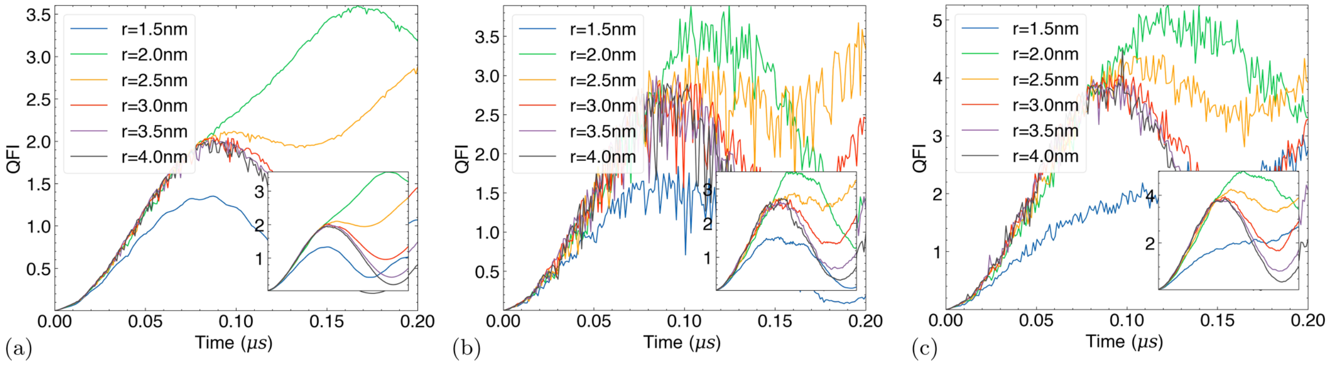

FIG. 9. Dynamics of QFI with Rabi frequency $\Omega = 2\pi \times 2.00$ MHz. All plots are the best value computed from 10 different SLD initializations. The insets contain moving averages of the main plots over 10 time steps. (a) $N = 2$, (b) $N = 3$, and (c) $N = 4$.

IV. CONCLUSION

An ensemble of NV center centers is a promising quantum metrology platform. While adding more independent spins improves the sensitivity, the probe can, in principle, also reach greater sensitivity due to entanglement created by interactions. Also, having a dense ensemble means that the total size of the probe can be smaller, resulting in better spatial resolution. However, without external control of the entanglement and the states generated, strong dipole-dipole interactions due to small separations between NV center centers within a dense ensemble are usually detrimental for the sensitivity as they lead to a rapid decay of the total spin.

To investigate a system of strongly interacting NV centers, we simulated the master equation with dissipation using MPDOs. We benchmarked the W^{II} and TDVP algorithms against the exact numerical diagonalization method for time evolution with a long-range interaction model. We found the W^{II} algorithm has bigger errors in the imaginary part and is less stable in a very small separation regime compared with TDVP. Then, with TDVP for small NV center separations, we investigated the effect of finite maximum bond dimensions on the simulation accuracy. We again determined the accuracy as a function of bond dimensions by comparing the obtained states to those from exact diagonalization. Stronger interactions result in larger errors, suggesting the need for larger bonds. For dissipative dynamics, we found higher accuracy, which can be attributed to slower growth of operator entanglement entropy. These results indicate that the tensor network method could be suitable for simulating an open system. However, we found an exception for $r = 1.5$ nm, for which the errors can be bigger even though the operator entanglement entropy is smaller than for $r = 2.0$ nm.

For applications in quantum sensing, we used the approach of locally optimizing approximations of the SLD to obtain the quantum Fisher information. The QFI of driven ensembles shows that strong interaction can create entanglement-enhanced sensitivity compared to independent spins. Our results are based on quantum Fisher information, which gives the ultimate achievable sensitivity optimized over all possible positive operator-valued measurements and unbiased estimator functions of the parameter. Future investigations will have to show to what extent this optimal sensitivity can be reached in specific sensing protocols.

Finally, we observed that the boost in sensitivity can diminish when the interaction becomes significantly larger than the Rabi frequency. In this situation, it is necessary to utilize microwaves with higher intensities for driving in order to increase the sensitivity.

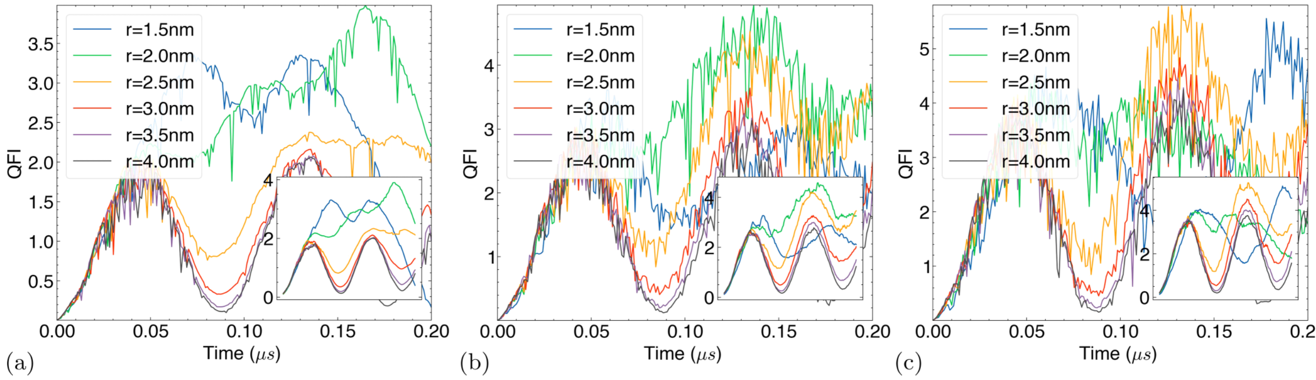

FIG. 10. Dynamics of QFI when the Rabi frequency is doubled from Fig. 9 to $2\Omega = 2\pi \times 4.00$ MHz. An increase of the maximal value of the QFI compared to the case with Rabi frequency $\Omega = 2\pi \times 2.00$ MHz can be observed for $r = 1.5$ nm. (a) $N = 2$, (b) $N = 3$, and (c) $N = 4$.

ACKNOWLEDGMENTS

This work was supported by the Baden Württemberg Stiftung, project CDINQUA. The tensor network codes are algorithms modified and implemented from TENPY [37].

APPENDIX A: PURE-STATE ENTANGLEMENT ENTROPY FOR A VECTOR AND AN OPERATOR

Any pure state has a Schmidt decomposition $|\psi_{AB}\rangle = \sum_i^r \sqrt{\lambda_i}|i\rangle_A \otimes |i\rangle_B$, with Schmidt coefficients $\sqrt{\lambda_i} > 0$ and $\sum_i^r \lambda_i = 1$. Then we can define the reduced density matrix for a bipartite system by partial trace over the other parts: $\rho_A = \mathrm{Tr}_B[\rho_{AB}] = \sum_i^r \lambda_i |i\rangle_A\langle i|_A$ and $\rho_B = \mathrm{Tr}_A[\rho_{AB}] = \sum_j^r \lambda_j |j\rangle_B\langle j|_B$. The density operator of the total system reads $\rho_{AB} = |\psi_{AB}\rangle\langle\psi_{AB}| = \sum_{ij}^{r,r} \sqrt{\lambda_i}\sqrt{\lambda_j}(|i\rangle_A \otimes |i\rangle_B)(\langle j|_A \otimes \langle j|_B)$. The entanglement entropy for the reduced density operators is defined as

$$S(\rho_A) = -\mathrm{Tr}[\rho_A \ln(\rho_A)] = -\sum_{i=1}^{r} \lambda_i \ln \lambda_i, \tag{A1}$$

where $S(\rho_A) = S(\rho_B)$. To find the operator entanglement entropy (opEE), we vectorize $\rho_{AB} \to |\rho_{AB}\rangle\rangle$,

$$|\rho_{AB}\rangle\rangle = |\psi_{AB}\rangle|\psi_{AB}\rangle \tag{A2}$$

$$= \sum_{\mu}^{r^2} \Lambda_\mu |i_A i_B; j_A j_B\rangle. \tag{A3}$$

Here, $\Lambda_\mu = \sqrt{\lambda_i}\sqrt{\lambda_j}$, and $\mu = (i, j)$. The superdensity operator, denoted by $\rho^\sharp$, can be created using an outer product:

$$\rho^\sharp_{AB} = |\rho_{AB}\rangle\langle\rho_{AB}| \tag{A4}$$

$$= \sum_{\substack{\mu=(i,j),\\ \nu=(k,l)}}^{r^2,r^2} \Lambda_\mu\Lambda_\nu |i_A i_B; j_A j_B\rangle\langle k_A k_B; l_A l_B|. \tag{A5}$$

Like for $\rho_A(\rho_B)$, we can also have $\rho^\sharp_A(\rho^\sharp_B)$, e.g., $\rho^\sharp_A = \sum_\mu^{r^2} \Lambda_\mu^2 |i_A; j_A\rangle\langle i_A; j_A|$. Then we can find the opEE,

$$S_{\mathrm{op}}(\rho^\sharp_A) = -\left[\sum_\mu \Lambda_\mu^2 \ln\left(\Lambda_\mu^2\right)\right] \tag{A6}$$

$$= -\left[\sum_{i,j} (\lambda_i\lambda_j)\ln(\lambda_i\lambda_j)\right] \tag{A7}$$

$$= -\left[\sum_{i,j} (\lambda_i\lambda_j)[\ln(\lambda_i) + \ln(\lambda_j)]\right] \tag{A8}$$

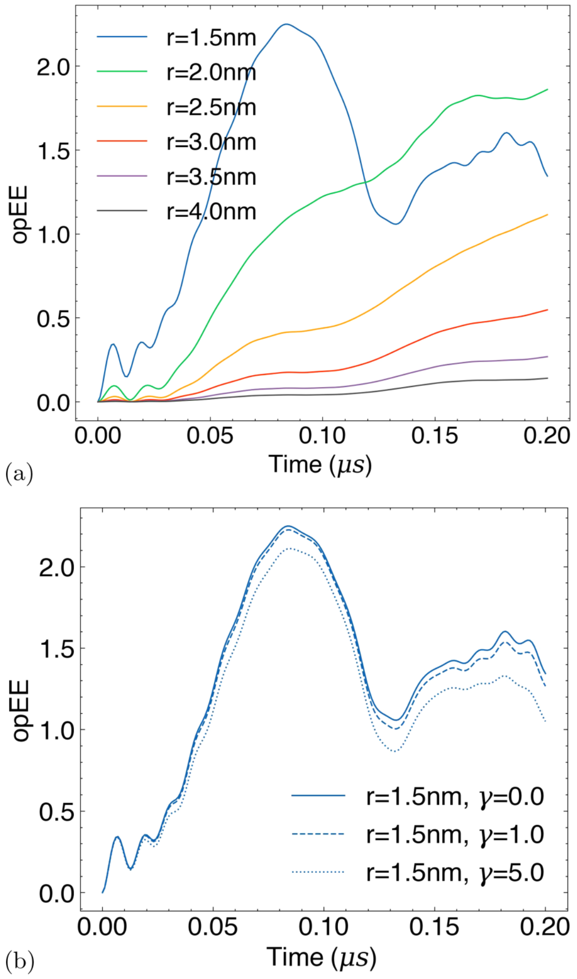

FIG. 11. Operator entanglement entropy of the middle bond. Rabi frequency is 2Ω.

$$= -\left[\sum_i (\lambda_i)\ln(\lambda_i)\sum_j(\lambda_j) + \sum_i(\lambda_i)\sum_j(\lambda_j)\ln(\lambda_j)\right] \tag{A9}$$

$$= -\left[2\sum_i \lambda_i \ln(\lambda_i)\right] \tag{A10}$$

$$= 2S(\rho_A). \tag{A11}$$

APPENDIX B: OPEE FOR RABI FREQUENCY 2Ω

Figure 11 shows, up to 200 ns, the dynamics of the operator entanglement entropy in the middle bond when the Rabi frequency is doubled from $\Omega = 2\pi \times 2.00$ MHz → $2\Omega = 2\pi \times 4.00$ MHz.

---

[1] J. M. Taylor, P. Cappellaro, L. Childress, L. Jiang, D. Budker, P. R. Hemmer, A. Yacoby, R. Walsworth, and M. D. Lukin, Nat. Phys. **4**, 810 (2008).

[2] P. Welter, J. Rhensius, A. Morales, M. S. Wörnle, C. H. Lambert, G. Puebla-Hellmann, P. Gambardella, and C. L. Degen, Appl. Phys. Lett. **120**, 074003 (2022).

[3] B. L. Dwyer, L. V. H. Rodgers, E. K. Urbach, D. Bluvstein, S. Sangtawesin, H. Zhou, Y. Nassab, M. Fitzpatrick, Z. Yuan, K. De Greve, E. L. Peterson, H. Knowles, T. Sumarac, J.-P. Chou, A. Gali, V. V. Dobrovitski, M. D. Lukin, and N. P. de Leon, PRX Quantum **3**, 040328 (2022).

[4] M. Haruyama, S. Onoda, T. Higuchi, W. Kada, A. Chiba, Y. Hirano, T. Teraji, R. Igarashi, S. Kawai, H. Kawarada, Y. Ishii, R. Fukuda, T. Tanii, J. Isoya, T. Ohshima, and O. Hanaizumi, Nat. Commun. **10**, 2664 (2019).

[5] P. Balasubramanian, C. Osterkamp, Y. Chen, X. Chen, T. Teraji, E. Wu, B. Naydenov, and F. Jelezko, Nano Lett. **19**, 6681 (2019).

[6] H. Zheng, J. Xu, G. Z. Iwata, T. Lenz, J. Michl, B. Yavkin, K. Nakamura, H. Sumiya, T. Ohshima, J. Isoya, J. Wrachtrup, A. Wickenbrock, and D. Budker, Phys. Rev. Appl. **11**, 064068 (2019).

[7] C. Wang, Q. Liu, Y. Hu, F. Xie, K. Krishna, N. Wang, L. Wang, Y. Wang, K. C. Toussaint Jr, J. Cheng, H. Chen, and Z. Wu, Rev. Sci. Instrum. **94**, 015109 (2023).

[8] H. Zhou, J. Choi, S. Choi, R. Landig, A. M. Douglas, J. Isoya, F. Jelezko, S. Onoda, H. Sumiya, P. Cappellaro, H. S. Knowles, H. Park, and M. D. Lukin, Phys. Rev. X **10**, 031003 (2020).

[9] E. Bauch, S. Singh, J. Lee, C. A. Hart, J. M. Schloss, M. J. Turner, J. F. Barry, L. M. Pham, N. Bar-Gill, S. F. Yelin, and R. L. Walsworth, Phys. Rev. B **102**, 134210 (2020).

[10] D. Farfurnik, Y. Horowicz, and N. Bar-Gill, Phys. Rev. A **98**, 033409 (2018).

[11] C. Osterkamp, M. Mangold, J. Lang, P. Balasubramanian, T. Teraji, B. Naydenov, and F. Jelezko, Sci. Rep. **9**, 5786 (2019).

[12] A. W. Sandvik, Phys. Rev. Lett. **104**, 137204 (2010).

[13] S. Schiffer, J. Wang, X.-J. Liu, and H. Hu, Phys. Rev. A **100**, 063619 (2019).

[14] C. Cheng, Phys. Rev. B **108**, 155113 (2023).

[15] S. Essink, Ph.D. thesis, Universität Bonn, 2018.

[16] G. Kucsko, S. Choi, J. Choi, P. C. Maurer, H. Zhou, R. Landig, H. Sumiya, S. Onoda, J. Isoya, F. Jelezko, E. Demler, N. Y. Yao, and M. D. Lukin, Phys. Rev. Lett. **121**, 023601 (2018).

[17] G. Vidal, Phys. Rev. Lett. **91**, 147902 (2003).

[18] D. Perez-Garcia, F. Verstraete, M. M. Wolf, and J. I. Cirac, Quantum Inf. Comput. **7**, 401 (2007).

[19] U. Schollwöck, Ann. Phys. (NY) **326**, 96 (2011).

[20] R. Orús, Ann. Phys. (NY) **349**, 117 (2014).

[21] M. Jarzyna and R. Demkowicz-Dobrzański, Phys. Rev. Lett. **110**, 240405 (2013).

[22] R. Finsterhölzl, M. Katzer, A. Knorr, and A. Carmele, Entropy **22**, 984 (2020).

[23] A. W. Schlimgen, K. Head-Marsden, L. M. Sager, P. Narang, and D. A. Mazziotti, Phys. Rev. Res. **4**, 023216 (2022).

[24] G. E. Fux, D. Kilda, B. W. Lovett, and J. Keeling, Phys. Rev. Res. **5**, 033078 (2023).

[25] H. Weimer, A. Kshetrimayum, and R. Orús, Rev. Mod. Phys. **93**, 015008 (2021).

[26] D. Jaschke, S. Montangero, and L. D. Carr, Quantum Sci. Technol. **4**, 013001 (2018).

[27] S. Paeckel, T. Köhler, A. Swoboda, S. R. Manmana, U. Schollwöck, and C. Hubig, Ann. Phys. (NY) **411**, 167998 (2019).

[28] M. P. Zaletel, R. S. K. Mong, C. Karrasch, J. E. Moore, and F. Pollmann, Phys. Rev. B **91**, 165112 (2015).

[29] J. Haegeman, C. Lubich, I. Oseledets, B. Vandereycken, and F. Verstraete, Phys. Rev. B **94**, 165116 (2016).

[30] C. Hubig, J. Haegeman, and U. Schollwöck, Phys. Rev. B **97**, 045125 (2018).

[31] S. Murciano, J. Dubail, and P. Calabrese, J. Phys. A **57**, 145002 (2024).

[32] G. J. Preisser Beltrán, Ph.D. thesis, Université de Strasbourg, 2023.

[33] G. Preisser, D. Wellnitz, T. Botzung, and J. Schachenmayer, Phys. Rev. A **108**, 012616 (2023).

[34] M. G. A. Paris, Int. J. Quantum Inf. **7**, 125 (2009).

[35] V. Giovannetti, S. Lloyd, and L. Maccone, Science **306**, 1330 (2004).

[36] K. Chabuda, J. Dziarmaga, T. J. Osborne, and R. Demkowicz-Dobrzański, Nat. Commun. **11**, 250 (2020).

[37] J. Hauschild and F. Pollmann, SciPost Phys. Lect. Notes 5 (2018).